

Arterial tree taper and bifurcations: implications on wave reflection and pressure at the aortic root using a one-dimensional computational model

A thesis submitted for the degree of Doctor of Philosophy

By

Shima Abdullateef

Department of Mechanical and Aerospace Engineering
Brunel University London

April 2020

ABSTRACT

Cardiovascular diseases are the prominent cause of mortality across the globe, and numbers are anticipated to grow with late industrialisation and urbanisation of the developing countries. Therefore, advancing techniques for the diagnosis of cardiovascular diseases is both desired and needed.

Understanding the behaviour of the flow in the arterial system in normal and pathological conditions may aid in improving the diagnosis and treatment of cardiovascular diseases. The existence of the wave reflections and their effect on the increase of pressure at the aortic root is well established, however, the distance that a reflected wave can travel from the periphery to reach the aortic root has not been investigated. This project aims to investigate the distance travelled and the amplitude of reflected waves originating from the periphery and addresses this objective by investigating wave propagation in simple structures first, then focusing on studying the main geometrical features of large arterial vessels.

A one-dimensional formulation of blood flow is used for replicating pulse wave propagation within compliant vessels. Initially, the influence of bifurcations is studied and used as building blocks for explaining the behaviour of reflections waves in a system. Another fundamental feature of the arterial tree which has not been widely studied is the arterial tapering. In this thesis, different computational models are used to reveal the direct impact of tapering and the tapering angle on the amplitude of pressure and wave speed. We further expand our understanding of the impact of tapering on the reflections by using a 55-segment arterial tree computational model.

The results show that with a high number of bifurcations, single reflections originating from a distal site may not be discernible due to re-reflection and entrapment of the waves between the bifurcations. This work shows that if there is a reflection generated from distal limbs, only 1 per cent of the pressure amplitude of the wave reaches to the aortic root. Further, tapering in the arterial tree causes a higher dissipation of wave compared to an arterial tree without tapering. However, the bifurcations may be the predominant cause of reflection in the arterial tree.

Furthermore, it is shown that increasing the tapering angle is associated with an increase in pulse pressure and peak pressure, as it can be seen in the ageing descending aorta.

Finally, it can be concluded that determining a location for wave reflections can be an oversimplification of the matter and might overlook the fact that some reflections are an amalgamation of multiple reflections or re-reflections. The outcome of this project can provide a better understanding of the response of a healthy arterial tree to wave reflections.

CONTENTS

Abstract.....	i
Contents	iii
Acknowledgement	vii
Preface.....	viii
List of Figures	ix
List of Tables	xiv
Abbreviations and Variables.....	xviii
Chapter 1. Introduction	1
1.1 Cardiovascular system	2
1.1.1 Heart.....	2
1.1.2 Vascular system	3
1.1.3 Blood.....	4
1.2 Blood flow and the arterial system	5
1.2.1 Brief historical review.....	5
1.2.2 Wave propagation	7
1.2.3 Pulse wave velocity.....	9
1.3 Computational models	11
Zero-dimensional models (0D)	11
One-dimensional models (1D).....	13
Three-dimensional models (3D)	14
1.4 Aim and Objectives.....	14
1.5 Outline of the thesis	15
Chapter 2. One-dimensional cardiovascular models	17
2.1 One-dimensional (1D) equations	17
2.1.1 Derivation of governing equations.....	18
2.1.2 Conservation of mass equation	19

2.1.3 Conservation of momentum equation.....	19
2.1.4 Pressure and Area relationship.....	23
2.2 The method of characteristics	24
2.3 Linearization of the equations.....	27
2.4 Numerical solution.....	28
2.5 Lumped parameter models.....	29
2.5.1 Terminal resistance (R).....	29
2.5.2 Two element Windkessel models (RC)	29
2.5.3 Three element Windkessel models (RCR).....	30
2.6 Interfaces.....	30
2.6.1 Inflow/outflow boundary conditions.....	30
2.6.2 Splitting flow	32
2.7 Wave separation and wave intensity.....	33
2.8 Linear analysis of wave reflections.....	35
Framework of computations	36
Chapter 3. Impact of bifurcations on pressure and wave reflections.....	37
3.1 Introduction.....	37
3.2 Methodology	38
3.2.1 Pressure waveforms in a simple bifurcation	39
3.2.2 Pressure waveforms in two-consecutive bifurcations.....	41
3.2.3 Pressure waveforms in a five-consecutive bifurcations.....	42
3.2.4 Pressure waveforms in a 15-consecutive bifurcation with inflow at terminal locations	43
3.3. Results.....	44
3.3.1 Pressure waveforms in a simple bifurcation	44
3.3.2 Pressure waveforms in two-consecutive bifurcations.....	51
3.3.3 Pressure waveforms in five-consecutive bifurcations.....	59
3.3.4 Pressure waveforms in a 15-consecutive bifurcations	61
3.4 Discussion.....	61
3.5 Conclusion	64
Chapter 4. Analysis of the response of the arterial tree to a reflected wave.....	65

4.1 Introduction.....	65
4.2 Methodology	66
4.3 Results.....	70
4.4 Discussion.....	78
4.5 Conclusion	80
Chapter 5. Impact of tapering on the pressure amplitude and reflections	81
5.1 Introduction.....	81
5.2 Methodology	83
5.2.1 Reflections in three-stepwise area reduction	83
5.2.2 Reflections in stepwise diameter reduction and continuously tapered vessel	84
5.2.3 A combination of step-wise tapering and a bifurcation	85
5.2.4 Tapering in the upper thoracic aorta	86
5.2.5 Tapering in the aorta and iliac bifurcation	88
5.3 Results and discussion	89
5.3.1 Reflections in three-step area reduction.....	89
5.3.2 Reflections in stepwise diameter reduction and continuously tapered vessel	92
5.3.3 A combination of step-wise structure and bifurcation.....	94
5.3.4 Tapering in the upper thoracic Aorta	95
5.3.5 Tapering in the descending aorta and iliac bifurcation.....	99
5.4 Limitations	102
5.5 Conclusion	103
Chapter 6. Impact of tapering in the arterial tree	104
6.1. Introduction.....	104
6.2. Methods.....	105
6.2.1 Forward direction.....	106
6.2.2 Backward direction	107
6.3. Results.....	110
6.3.1 Forward direction.....	110
6.3.2 Backward direction	111
6.4. Discussion.....	112
6.5. Limitations	113

6.6. Conclusion	114
Chapter 7.General Discussion.....	115
7.1. Summary of the Thesis Achievement	117
7.2. Implications for Future Research.....	118
Appendix I. Calculation of arterial resistance and compliance	119
References.....	122

ACKNOWLEDGEMENT

I would like to express my appreciation and gratitude to everyone who helped and supported me during my PhD.

First, I would like to thank my supervisor, Professor Ashraf Khir, for his guidance, and patience during this project. I appreciate his expertise, directions and motivations throughout my work. Also, I would like to thank my second supervisor, Dr Quan Long, for his ideas and technical advice.

I wish to thank all the academics that I had the opportunity to meet during my thesis. Dr Jordi Alastruey and Dr Jorge Mariscal-Harana of King's College London, who helped me with 1D model, Dr Madalina Negoita for her friendship and helping me with Image processing methods, Professor José González-Alonso, Dr Svetlana Ignatova and Professor Wamadeva Balachandran for their valuable comments and suggestions to improve my work, Dr Wisam Hacham who introduced me to the lab environment, and finally, Professor Colin Clark for his suggestions and advice. It was a great honour to meet with Professor Kim Parker and have the opportunity to discuss my work with him.

I would like to express my gratitude to the family that I found away from home, Mrs Jenny Kume, Jaleh, Samira, and Shirin. Thank you for all the moral support and help. Life would have been harder without you.

Also, I would like to express my deepest gratitude to my colleague and best friend, Alessandro, for all of his help in the lab, proofreading, supporting me through tough times and all the adventure we had together.

I would also like to thank all my friends for all the moments we spent together, Masoud, Nicola, Angel, Giulia, Enrico, Femke and many more fellow students in BIB.

Last but not least, I would like to thank and dedicate this thesis to my mother, father and sister for believing in me, encouraging me, and their unconditional support.

PREFACE

Parts of the results presented in Chapter 3 is published by IEEE Engineering in Medicine and Biology Society, Computing in Cardiology 2018, Maastricht, The Netherlands (Abdullateef *et al.*, 2019).

The research presented in Chapter 5 is published by the International Journal of Numerical Methods in Biomedical Engineering (Abdullateef, Mariscal-Harana and Khir, 2020) and partially published in proceedings of Artery research (Abdullateef *et al.*, 2020).

LIST OF FIGURES

Figure 1. 1. The structure of the wall in the blood circulatory system. The layout of the wall in an elastic artery, a muscular artery, and arterioles are presented. (www.memorangapp.com) .4	4
Figure 1. 2. The concept of Windkessel (Westerhof, Lankhaar and Westerhof, 2009).....	12
Figure 1. 3. The schematic of two-element, three-element, and four-element Windkessel models (Westerhof, Lankhaar and Westerhof, 2009).	13
Figure 2. 1. A simple, compliant vessel with cross-sectional area A , wall thickness h , flow velocity U , and length l in 1D orientation.....	18
Figure 2. 2. The velocity profile estimated by Equation (2.20) in a parabolic form (solid line, $\gamma=2$) and used by Smith et al. (2002) (dashed line, $\gamma=9$)	22
Figure 2. 3. Definition sketch of forward and backward characteristics. Every point (x,t) is intersected by a unique pair of characteristics curves.....	26
Figure 2. 4. Layout of the Riemann problem which takes into account the characteristic information reaching to both sides of the interface (x_0) and calculates the upwinded states AL_u, UL_u and AR_u, UR_u originated from the discontinuity between two initial states AL, UL and AR, UR	31
Figure 2. 5. Schematic representation of a bifurcation.	32
Figure 2. 6. A description of the procedure of calculation of wave propagation using the 1D model. The input variables are defined, and the numerical platform solves the equations of conservation of mass and momentum and tube law and produces the changes in pressure and velocity and area changes.	36
Figure 3. 1. The prescribed terminal boundary conditions for the daughter vessels, which is either absorption ($R=0$), or blocked ($R=1$).....	40
Figure 3. 2. A simple bifurcation with an inflow defined at the terminal boundary condition of daughter 1. Other boundaries are complete absorption ($R=0$).....	41
Figure 3. 3. Two-consecutive bifurcations with different locations prescribed for inflow. Other than inflow, the boundary condition for distal ends are absorption ($R=0$).....	42
Figure 3. 4. Schematic presentation of the five consecutive bifurcations with one blocked terminal point in its fifth bifurcation.....	43
Figure 3. 5. A schematic presentation of 15-consecutive bifurcations. The inflow is injected at the end of daughter vessels in each generation of bifurcations.	44

Figure 3. 6. The pressure variation in vessels of the bifurcation model. M is the mother/parent vessel, D1 is the first daughter vessel, and D2 is the second daughter vessel. The terminal boundary condition for both daughter vessels is absorption. (Experiment a) The pressure is estimated in two locations at each vessel; location 1 is close to its inlet and location 2 is at the outlet.....45

Figure 3. 7. Pressure waveforms in all vessels in a bifurcation. The terminal boundary condition for daughter vessel 1 is blocked while daughter vessel 2 has an absorbing boundary condition. (Experiment b) location 1 is close to its inlet and location 2 is at the outlet.....46

Figure 3. 8. Pressure waveforms in all vessels in a bifurcation. The terminal boundary conditions for both daughter vessels are blocked. (Experiment c)48

Figure 3. 9. The pressure variation in vessels of the bifurcation model. M is the mother vessel, D1 is the first daughter vessel, and D2 is the second daughter vessel. The inflow introduced to the system from the end of daughter 1 and terminal boundary conditions for other vessels are absorption.....50

Figure 3. 10. The pressure variation in vessels of the two-consecutive bifurcation model. The inflow is introduced to the system from the inlet of vessel 1, and terminal boundary conditions for the rest of vessels are complete absorption. (Experiment a)52

Figure 3. 11. The pressure variation in vessels of the two-consecutive bifurcation model. The inflow is introduced to the system from the outlet of vessel 2 to replicate a reflection wave behaviour, and terminal boundary conditions for the rest of the vessels are complete absorption. (Experiment b)54

Figure 3. 12. The pressure variation in vessels of the two-consecutive bifurcations model. The inflow is introduced to the system from the outlet of vessel 4, and terminal boundary conditions for the rest of vessels are complete absorption. (Experiment c)57

Figure 3. 13. Pressure and velocity variations in the stem vessel of the 5-consecutive bifurcations with all-absorbing terminal boundary conditions (top) and one blocked end in the fifth bifurcation (bottom). Each label in the figures corresponds to a wave. The left-hand picture is the input wave, and the right-hand side is a magnified view of the rest of pressures and velocities.60

Figure 3. 14. The rate of the measured pressure in the mother vessel, $P(M)$, over the pressure measured in the daughter vessels, $P(D)$, in 15 generations of bifurcations.61

Figure 4. 1. A schematic representation of the arterial tree model and the impulse..... 69

Figure 4. 2. The estimated pressure (left column) and velocity (right column) in five locations along the aorta and iliac artery in open valve (OV) and close valve (CV) conditions.	71
Figure 4. 3. The pressure amplitude of pulse travelling the arterial tree in the reverse direction with a close valve. The inflow is induced at R. anterior tibial, about 118 centimetres away from the ascending aorta.....	72
Figure 4. 4. The velocity amplitude of pulse travelling the arterial tree in the reverse direction with a close valve (CV). The inflow is induced at R. anterior tibial, about 118 centimetres away from the ascending aorta.	73
Figure 4. 5. The backward pressure component of the pulse induced at the R. anterior tibial in iliac-femoral (left) and the aorta (right), both in CV and OV conditions. The locations are separated into two different graphs so that the difference between the values in the aorta be visible.....	73
Figure 4. 6. Wave intensity analysis in the backward direction for the imposed pulse at the R. anterior tibial. The left figure shows the intensity in the right distal iliac, and the right figure shows the intensity in the aorta. The locations are separated into two different graphs so that the difference between the values in the aorta be visible.....	74
Figure 4. 7 Pressure waves in the right iliac artery at the distal point, midpoint and proximal to the iliac bifurcation.	75
Figure 4. 8. The pressure transfer at the iliac bifurcation with a pulse induced from right anterior tibial. The middle point of each vessel is selected.....	76
Figure 4. 9. The estimated pressure (left) and velocity (right) at five locations in the arterial tree as the pulse is inserted in the right anterior tibial.	77
Figure 5. 1. A schematic representation of a tapered structure with a three-stepwise reduction in their diameter.....	84
Figure 5. 2. Stepwise tapering of a vessel compared to a continuously tapered vessel. The tapering angle in all the structures is similar	85
Figure 5. 3. A combination of a stepwise tapering and bifurcation. The measurement point is located at the inlet of the parent vessel.	86
Figure 5. 4. The three-element Windkessel model connected to the outlet of the thoracic aorta.	87
Figure 5. 5. Schematic representation of the model consisting of the upper thoracic aorta and its side-branches connected to the iliac bifurcation	88

Figure 5. 6. The pressure in the inlet of the first (blue), second (red), and third (green) segments in the three stepwise model.....	90
Figure 5. 7. A schematic representation of stepwise tapering consisting of three segments and emerged reflections pattern. The length of all the segments L1, L2, and L3 are 5 metres. c1, c2 and c3 denote for wave speed in the respective segments.	92
Figure 5. 8. The pressure in the inlet (A) and the outlet (B) of a continuous tapered, 5-step diameter reduction, 4-step diameter reduction and a straight vessel.	92
Figure 5. 9. Wave intensity analysis in a straight vessel, a continuously tapered vessel, 4-step reduction of diameter, and 5-step reduction of diameter.	94
Figure 5. 10. The pressure (top) and wave intensity analysis (bottom) at the inlet of a stepwise structure with segments 5 metres long (Experiment 1), 0.312 metres (Experiment 2), and 0.078 metres (Experiment 3). All the structures have the same mechanical properties except the axial length of its consisting segments. The structure ends with a bifurcation, where the daughter vessel diameter is reduced in the same manner.	95
Figure 5. 11. The measured pressure and velocity at the inlet of the thoracic vessel in different angles of tapering.....	97
Figure 5. 12. Forward and backward components of the pressure measured at the inlet of the upper thoracic aorta in different tapering angles.	97
Figure 5. 13. The arterial compliance (left) and resistance (right) changes with increased tapering angles.	98
Figure 5. 14. Wave intensity analysis at the inlet of the thoracic aorta with different tapering angles.	99
Figure 5. 15. Pressure waveforms measured at the ascending aorta in the model of the aorta and iliac bifurcation.	100
Figure 5. 16. Wave intensity analysis at the ascending aorta. The model consists of the aorta connected to the iliac bifurcation. The tapering angle is changing in the descending aorta..	101
Figure 5. 17. The reported variation of tapering angle in descending aorta with ageing in Hickson et al. (2010).....	102
Figure 6. 1. The schematic representation of the arterial model and the induced inflow. Blue solid circles indicate the measurement sites. The first Red arrow indicates the direction of the wave in the forward direction and the second red arrow shows the direction of the wave in the backward used in the second simulation.....	107

Figure 6. 2. Pressure (left) and velocity (right) at the ascending aorta (top row) and thoracic aorta in tapered and non-tapered arterial structures.....	110
Figure 6. 3. Wave intensity analysis at the ascending aorta and thoracic aorta when the arterial tree is tapered (T) and non-tapered (NT)	111
Figure 6. 4. The ratio of the backward pressure along the aortic arch and ascending aorta. The simulations are done in CV (left) and OV (right) conditions. In each figure, the ratios for the tapered and non-tapered structure is presented.....	111
Figure 6. 5. The backward wave intensity ratio across the aortic arch when the pulse is travelling towards the ascending aorta in CV and OV conditions.....	112
Figure A1. 1. Schematic representation of reduction of a single vessel into a two-element Wk model in 1D model.....	119

LIST OF TABLES

Table 1. 1. Relation of the electrical elements and their hydraulic application in Windkessel	13
Table 2. 1. Forward and backward waves, signs of the waves and their function.....	34
Table 2. 2. Types of reflection coefficient and their corresponding values.....	36
Table 3. 1. The properties used in the simple bifurcation model.....	40
Table 3. 2. The parameters used for modelling two-consecutive bifurcations.....	42
Table 3. 3. The parameter used in five-consecutive bifurcations model.	43
Table 3. 4. The wave speed and reflection coefficient calculated for each vessel in a simple bifurcation model.....	44
Table 3. 5. Pressure waves and their corresponding route, amplitude and time of occurrence in Experiment a. The values given by the simulations are compared against the values calculated by the theoretical equations.	45
Table 3. 6. Information about the pressure waveforms present in the daughter vessels 1 and 2.	46
Table 3. 7. Pressure waves and their corresponding route, amplitude and time of occurrence in mother vessel (V1). The values given by the simulations are compared against the values calculated by the theoretical equations. (Experiment b).....	47
Table 3. 8. Pressure waveforms amplitude and time, and their routes in daughter 1. (Experiment b).....	47
Table 3. 9. Pressure waveforms amplitude and time, and their routes in daughter 2 with an absorbing end. (Experiment b).....	48
Table 3. 10. Pressure waves and their corresponding route, amplitude and time of occurrence in mother vessel (V1). The values given by the simulations are compared against the values calculated by the theoretical equations. (Experiment c)	49
Table 3. 11. Pressure waveforms amplitude and time, and their routes in daughter 1 and 2 with blocked ends. (Experiment c)	49
Table 3. 12. Pressure waves and their corresponding route, amplitude and time of occurrence in mother vessel (V1). The inflow is inserted from the daughter vessel to replicate a reflection. (Reverse direction).....	50

Table 3. 13. Pressure waves and their corresponding route, amplitude and time of occurrence in Daughter1, where the inflow is injected. (Reverse direction)	50
Table 3. 14. Pressure waves and their corresponding route, amplitude and time of occurrence in Daughter2. The inflow is injected into daughter vessel 1. (Reverse direction).....	51
Table 3. 15. Wave speed and reflection coefficient calculated for vessels in two-consecutive bifurcations' model.....	51
Table 3. 16. Pressure waves and their corresponding route, amplitude and time of occurrence in vessel 1 in the two-consecutive bifurcations model. The inflow is injected into vessel 1. (Experiment a)	52
Table 3. 17. Pressure waves and their corresponding route, amplitude and time of occurrence in vessel 1 in the two-consecutive bifurcations model. The inflow is injected into vessel 2. (Experiment a)	53
Table 3. 18. Pressure waves and their corresponding route, amplitude and time of occurrence in vessel 1 in the two-consecutive bifurcations model. The inflow is injected into vessel 3. (Experiment a)	53
Table 3. 19. Pressure waves and their corresponding route, amplitude and time of occurrence in vessel 1 in the two-consecutive bifurcations model. The inflow is injected into vessel 4. (Experiment a)	53
Table 3. 20. Pressure waves and their corresponding route, amplitude and time of occurrence in vessel 1 in the two-consecutive bifurcations model. The inflow is injected into vessel 5. (Experiment a)	54
Table 3. 21. Pressure waves and their corresponding route, amplitude and time of occurrence in vessel 1 in the two-consecutive bifurcations model. The inflow is injected into vessel 2 to replicate a reflection wave. (Experiment b).....	55
Table 3. 22. Pressure waves and their corresponding route, amplitude and time of occurrence in vessel 2 in the two-consecutive bifurcations model. The inflow is injected into vessel 2 to replicate a reflection wave. (Experiment b).....	55
Table 3. 23. Pressure waves and their corresponding route, amplitude and time of occurrence in vessel 3 in the two-consecutive bifurcations model. (Experiment b).....	55
Table 3. 24. Pressure waves and their corresponding route, amplitude and time of occurrence in vessel 4 in the two-consecutive bifurcations model. The inflow is injected into vessel 2 to replicate a reflection wave. (Experiment b).....	56

Table 3. 25. Pressure waves and their corresponding route, amplitude and time of occurrence in vessel 5 in the two-consecutive bifurcations model. The inflow is injected into vessel 2 to replicate a reflection wave. (Experiment b).....	56
Table 3. 26. Pressure waves and their corresponding route, amplitude and time of occurrence in vessel 1 in the two-consecutive bifurcations model. The inflow is injected into vessel 4 to replicated distal reflections. (Experiment c)	57
Table 3. 27. Pressure waves and their corresponding route, amplitude and time of occurrence in vessel 2 in the two-consecutive bifurcations model. The inflow is injected into vessel 4 to replicate a distal reflection. (Experiment c).....	58
Table 3. 28. Pressure waves and their corresponding route, amplitude and time of occurrence in vessel 3 in the two-consecutive bifurcations model. The inflow is injected into vessel 4 to replicate a distal reflection. (Experiment c).....	58
Table 3. 29. Pressure waves and their corresponding route, amplitude and time of occurrence in vessel 4 in the two-consecutive bifurcations model. The inflow is injected into vessel 4 to replicate a distal reflection. (Experiment c).....	59
Table 3. 30. Pressure waves and their corresponding route, amplitude and time of occurrence in vessel 5 in the two-consecutive bifurcations model. The inflow is injected into vessel 4 to replicate a distal reflection. (Experiment c).....	59
Table 3. 31. Pressure waves and their corresponding route, amplitude and time of occurrence in vessel 1 in the two-consecutive bifurcations model. The inflow is injected into vessel 2. (Experiment c)	60
Table 4. 1. The geometrical and peripheral resistance of segments in the computational arterial tree model.....	68
Table 4. 2. Description of the waves in the right iliac artery shown in Figure 4.7.....	75
Table 5. 1. The dimensions and properties used in the structure with a three-stepwise reduction in diameter.....	84
Table 5. 2. The properties used in the comparison of 4 stepwise, five stepwise diameter reduction, continuous tapered, and straight vessel.....	85
Table 5. 3. The dimension of vessels used in tapered vessels and a bifurcation. In experiment 1, the segments are 5 metres long, and in experiment 2, the length of each segment is 0.3125 metres, and in experiment 3, the segments are 0.07 metres.....	86
Table 5. 4. The properties used in the thoracic aorta model taken from (Xiao, Alastruey and Figueroa, 2014).....	87

Table 5. 5. Parameters used in the aorta and iliac bifurcation model.	89
Table 5. 6. Description of each pressure wave appearing in the experiment.....	91
Table 5. 7. A comparison of the local pulse wave velocity (PWV_{MK}) at the inlet of each segment using the Moens-Korteweg equation their mean value (PWV_{mean}) and the regional pulse wave velocity using the foot-to-foot method (PWV_{ff}).	91
Table 5. 8. Different tapering angles in thoracic aorta and the value pulse wave velocity in the inlet, outlet, mean, and the foot-to-foot method.	96
Table 5. 9. The changes in the angle of tapering and the outlet diameter in the upper thoracic model.....	96
Table 6. 1. Diameter values in the tapered and non-tapered arterial model. Column four consists of the radius of the tapered segments at the inlet and outlet, and column five is the radius used for the non-tapered arterial tree. In the backward direction simulations, segment 71 is changed to a source of a pulse, and it is highlighted with grey.	108

ABBREVIATIONS AND VARIABLES

Abbreviations

BCW	Backward Compression Wave
BEW	Backward Expansion Wave
CVD	Cardiovascular Disease
CV	Close-Valve
FCW	Forward Compression Wave
FEW	Forward Expansion Wave
NT	Non-Tapered
ODE	Ordinary Differential Equation
OV	Open-Valve
PDE	Partial Differential Equation
PWV or c	Pulse Wave Velocity or Wave speed
T	Tapered
Wk	Windkessel
WIA	Wave Intensity Analysis

Variables

α	Area ratio	-
A_0	Initial area value	cm^2
β	Wall mechanical properties	$m^{-2}kg s^{-2}$
c	pulse wave velocity or wave speed	m/s
c_{MK}	Moens-Korteweg's wave speed	m/s
c_{fft}	Foot-to-foot wave speed	m/s
C	Peripheral Compliance	$m^3 Pa^{-1}$
C_v	Vessel compliance	$m^3 Pa^{-1}$
D	Diameter	cm
d	Derivative	-
∂	Partial Derivative	-
σ	Circumferential tensile stress,	N/m^2

ν	Poisson's ratio	-
dI	Wave intensity	$W m^{-2} s^{-2}$
dI_f	Forward component of wave intensity	$W m^{-2} s^{-2}$
dI_b	Backward component of wave intensity	$W m^{-2} s^{-2}$
E	Young's modulus	N/m^2
ϵ	Strain	-
f	Friction force	N/m
h	Wall thickness	mm
l	Length	cm
$\lambda_{f\&b}$	Eigenvalues	m/s
μ	Dynamic viscosity of the fluid	$cm^{-1} g s^{-1}$
p	Pressure	$mmHg$
p_f	Forward component of pressure	$mmHg$
p_b	Backward component of pressure	$mmHg$
p_0	Initial pressure value	$mmHg$
Q	Flow rate	m^3/s
R_0	Initial radius value	mm
Re	Reynolds number	-
R_f	Reflection coefficient	-
$R_1 \& R_2$	Peripheral resistance	$Pa s m^{-3}$
R_v	Vessel resistance	$Pa s m^{-3}$
ρ	Density	Kg/m^3
U	Velocity of the flow	m/s
U_0	Initial value for velocity	m/s
W_f	Forward Characteristic variable	m/s
W_b	Backward Characteristic variable	m/s
x	Axial position	m
Z	Characteristic impedance	$m^{-4} Kg s^{-1}$

CHAPTER 1

INTRODUCTION

Interpreting the underlying mechanism of blood pressure and wave propagation in the arterial tree can provide instructions about the alteration in the pulse waveforms and the possible cardiovascular pathologies.

Mechanical properties of the arterial tree, such as vessel stiffness and geometry, can influence the shape of arterial pressure and flow waves. For example, aortic unfolding is a common clinical expression referring to the elongation and enlarging of the aortic arch diameter caused by ageing, and previous works proved that it increases the central arterial blood pressure and pulse pressure (O'Rourke and Nichols, 2005; Sugawara *et al.*, 2008; Redheuil *et al.*, 2011; Collins *et al.*, 2014).

In addition, any changes in mechanical properties could generate a wave reflection or a wave travelling towards the heart. Wave reflections and the principle site for reflections has been the focus of several studies (Bos *et al.*, 1976; Khir and Parker, 2005; Westerhof *et al.*, 2008). However, the determination of the reflection site and the distance that a reflected wave can travel is an ongoing debate (Segers *et al.*, 2017).

It is suggested that the reflected waves are a combination of the multiple reflections rather than a single wave, and the further the site of the reflection the more their dissipation in their contribution to reflections (Davies *et al.*, 2012). Further, the possible sources of reflections and damping the reflected waves in a healthy arterial tree is assumed to be the tapered structure and bifurcations. However, a quantitative study of the influence of the mentioned factors is absent in the literature, highlighting the need for investigation on the main characteristics of the arterial tree on the reflected waves.

Recent studies demonstrated that one-dimensional models have the ability to capture the main features of the area, pressure and flow waveforms in human conduit arteries, (Olufsen *et al.*, 2000; Steele *et al.*, 2003; Willemet, Lacroix and Marchandise, 2013; Xiao, Alastruey and Figueroa, 2014; Boileau *et al.*, 2015).

Hence, in this project, the influence of bifurcations and tapering is studied using the computational wave propagation in different 1D models, simulated as a network of flexible

vessels. This chapter starts with the anatomical and physiological description of elements of the systemic circulation (Section 1.1), followed by an explanation about blood flow and waves in the arterial tree (Section 1.2). Next, a brief description of the computational models used for the study of the blood flow in the arterial tree is provided in Section 1.3. The aim and objective of this research can be found in Section 1.4, and the outlook of this thesis is given in Section 1.5.

1.1 CARDIOVASCULAR SYSTEM

In the cardiovascular system, approximately 5 litres of blood is circulated between the heart and the volume of the arterial bed. Blood is responsible for transferring oxygen, hormones, nutrients and cellular waste products throughout the body (Baker, Tortora and Nostakos, 1976). The blood circulations have a crucial role in the thermoregulation of our body and in the distribution of hormones and other chemical substances that are necessary to cells. Each part of the cardiovascular system is explained in more detail in this section.

1.1.1 HEART

The heart acts as a pump which drives the blood into the arterial system periodically; it consists of four chambers: two atria and two ventricles. The heart's pumping action is constituted by two phases: systole and diastole. Blood is ejected into the aorta and the pulmonary artery in the systolic phase due to the contraction of the left and right ventricles, respectively. While in the diastolic phase ventricles relax and are refilled because of gravitational and inertial forces and the atrial contraction. The atrial and ventricular contractions are the result of electrical impulses originating from the Sino-arterial (SA) node, located at the top of the right atrium. The electrical activity of the heart can be acquired and studied for diagnostic purposes with the echocardiogram (ECG), representing a powerful clinical tool.

The right ventricle sends the blood to the pulmonary circulation, which allows deoxygenated blood to be re-oxygenated in the lungs. The left ventricle sends the blood into the aorta, and from there the blood travels through the whole body until it reaches to the capillary circulation via arteriole and exchanges the oxygen, nutrients and waste products with cells. Venules collect the blood from the capillaries and carry the cellular waste products and the CO₂ to the veins that convey the blood back to the heart. (Figure 1.1)

1.1.2 VASCULAR SYSTEM

The systemic circulation consists of a network of curved and branching vessels whose size decreases in the arteries, arterioles, and capillary beds, and an increase in venules and veins. As it is shown in Figure 1.1, the arterial wall and the veins wall are constructed of three layers or tunicae:

- Tunica adventitia: this layer is the outer coat of the arterial vessel, and it is mainly composed of elastin and collagen fibres.
- Tunica media: the middle coat or tunica media is composed of elastic fibres and smooth muscles cells. It is usually the thickest layer and plays a vital role in two functional properties of elasticity and contractility.
- Tunica intima: the inner layer is mainly composed of endothelial cells which are in contact with the blood and play a crucial role in mechanosensing pathways, determining vasodilation and vasoconstriction.

Due to different composition and function of each layer, the relative thickness (i.e. the ratio between the layer and the total wall thickness) of each them varies throughout the circulatory system. For example, arteries close to the heart have to withstand high pressure and recoil during diastole; therefore, such arteries contain a high percentage of elastic fibres in all its layers and are commonly defined as elastic arteries (Figure 1.1). Moving along the arterial tree further away from the heart, the percentage of smooth muscles in tunica media increases while the amount of elastic fibres decreases. These arteries are commonly defined as muscular arteries. Finally, in arterioles, the thickness of all three layers diminishes significantly. They are also known as the resistance vessels because with their narrow lumen, and they cause a slowdown in blood flow (Baker, Tortora and Nostakos, 1976).

In studies of the circulatory system, the arteries are divided into two groups: 1) Large or conducting vessels and 2) small vessels. A reason for this separation is the significant difference among the predominance of inertial effects over viscous effect in the blood flow in different vessel sizes. By using the Reynolds number, Re , the behaviour of the flow can be predicted. Reynolds number (adimensional) can be calculated by Equation 1.1. (Reynolds, 1883)

$$Re = \frac{U D}{\nu} = \frac{\rho D U}{\mu} = \frac{\rho U^2}{\mu U/D} \sim = \textit{inertial force/viscous force} \quad (1.1)$$

Where U is the velocity of the flow, ν is the kinematic viscosity, and D is the diameter of the vessel. Re can also be rewritten in the form of the second expression in equation 1.1, where the dynamic viscosity of the fluid (μ) and the density (ρ) are considered.

Finally, Reynold's number also can be reformulated as the ratio of inertial force over the viscous force, as shown in the third term of equations 1.1.

This thesis focuses mainly on the mechanics and behaviours of large blood vessels.

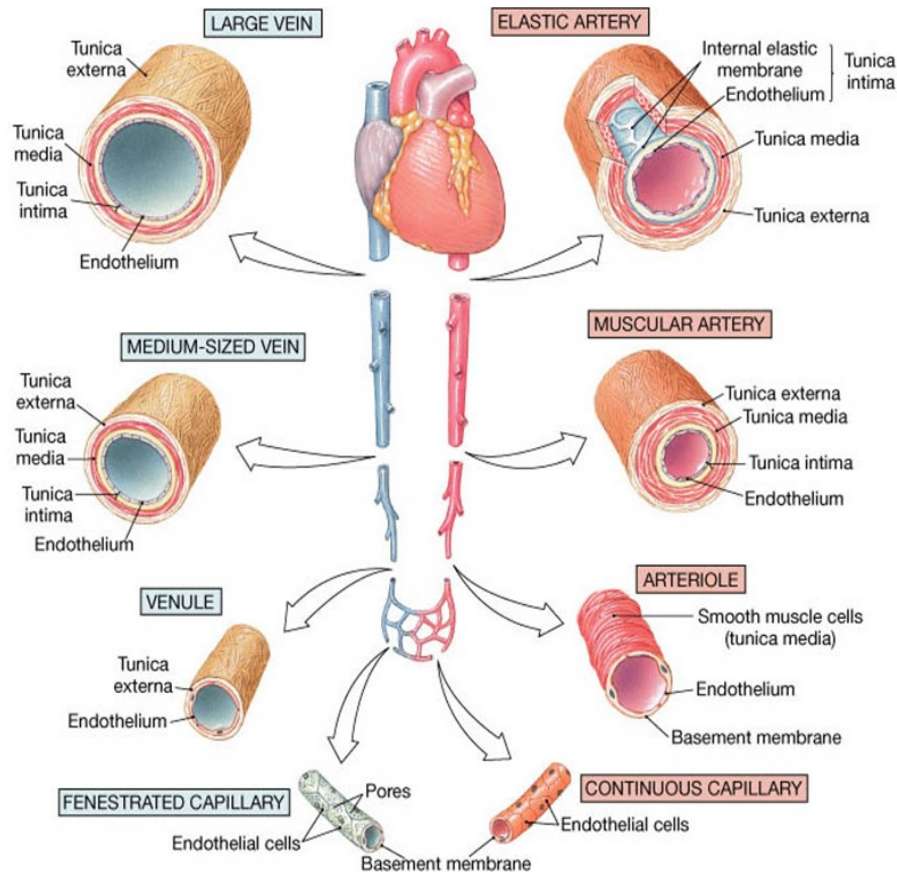


Figure 1. 1. The structure of the wall in the blood circulatory system. The layout of the wall in an elastic artery, a muscular artery, and arterioles are presented. (www.memorangapp.com)

1.1.3 BLOOD

Blood is a liquid connective tissue that transports oxygen from the lung to the cells and returns carbon dioxide from cells to the lungs. Blood also has a crucial role in maintaining the temperature throughout the body as well as the PH. Blood is composed of two parts: 45% is formed elements such as red cells, white cells and platelets (Baker, Tortora and Nostakos, 1976). The remaining part is the plasma which is a watery liquid containing the dissolved substance. The plasma is regarded as a homogeneous Newtonian fluid of density of 1050 kg/m^3 , and its viscosity is $0.0012 - 0.0016 \text{ kg/m s}$ at $37 \text{ }^\circ\text{C}$ (Peskin, 1982). Compared to water, blood is thicker heavier and more viscous. Since red blood cells have the

highest concentration among other particles, the mechanical properties of the blood are approximated with those of the red blood cells.

It is also worth mentioning that the blood is not homogenous. However, in the vessels with diameters which exceed 100 μm , particles size becomes negligible with respect to the vessel size and blood can be regarded as homogenous (Peskin, 1982).

1.2 BLOOD FLOW AND THE ARTERIAL SYSTEM

1.2.1 BRIEF HISTORICAL REVIEW

William Harvey (1578-1657) was the first known author to start the modern conception of cardiovascular physiology and biophysics. He described the complete systemic circulation and blood properties and published his results in 1628 (Harvey, 1628).

Stephan Hales (1677-1761) successfully measured arterial pressure in animals. He proposed that the arterial system act similarly to the inverted, air-filled dome of a contemporary fire engine. Hence, the arterial system can smooth the pressure oscillations produced by the intermittent pumping action of the heart. Moreover, Hale was the first to introduce the concept of peripheral resistance. Isaac Newton (1642-1727) had a crucial role in the modern understanding of the cardiovascular system with his work in mathematics and introducing the concept of fluid viscosity, which provides crucial information about vascular resistance and blood flow.

The theoretical approach to the circulation originated from the work of a mathematician called Leonhard Euler (1707-1783). In 1755, he published the one-dimensional equations of conservation of mass and momentum in a distensible tube. In 1808 a physician called Thomas Young (1773-1829) explained the relationship between the velocity of propagation of the arterial pulse and elastic properties of the vessel.

It is worth mentioning the contributions of Fourier (1768-1839), which was not directly related to the mechanics of arteries but had a significant impact on arterial hemodynamic. In 1822, he claimed that periodic functions could be expressed as the superimposition of an infinite series of sinusoidal functions. This concept was later used in modelling the flow behaviour in the arterial system (Fourier, 2009).

Jean Louis Poiseuille (1799-1869), with the development of his law of viscous flow in tubes, indirectly contributed to the arterial mechanics. According to Poiseuille (1846), the volume flow rate is proportional to the diameter, length, and the pressure drop along the tube. The speed of wave propagation in elastic tubes was studied by two brothers called Wilhelm Eduard

Weber and Ernst-Heinrich Weber. In 1866, they published their findings and proposed a formula for calculation of wave speed, which is derived from the density of the fluid and the radial distensibility of the tube (Weber and Weber, 1825).

One of the mathematicians who influenced the area of hemodynamic without any work on arterial mechanics or waves was Riemann (1826-1866). He published a general solution for hyperbolic systems of partial differential equations in 1860, which was later used to solve the equations related to the arterial system and waves (Riemann, 1876).

Two more scientists dedicated their work to define the wave speed of elastic tubes in 1877-1878. Adriaan Isebree Moens (1846-1891) published his experimental results on wave speed in arteries (Moens, 1877), while Korteweg (1848-1941) published a theoretical study on wave speed (Korteweg, 1878). In his theoretical analysis, the wave speed was determined considering both the elasticity of the tube wall and the compressibility of the fluid.

With the contributions of Otto Frank (1865-1944) in qualitative physiology, the arterial mechanics could be estimated with mathematical formulations. Frank followed the theory of Hales about the resemblance of the arterial system to the air-filled dome of a fire engine's pump and formulated the Windkessel (Wk) model (air chamber in German) (Frank, 1899). Moreover, in 1905, he also introduced the theory of waves in arteries (Frank, 1905).

In 1955 McDonald started using the Fourier series in hemodynamics. With the contribution of Womersley, they developed the concept of impedance analysis through the Fourier technique in the frequency domain. McDonald, thanks to the pulsatile nature of blood flow in the arteries, approximated arterial pressure to a periodic signal and exploited the theoretical formulation of Fourier to decompose arterial pressure into an assembly of sinusoidal waves.

The modelling of the arterial system started with an analogue model of Noordergraaf and his team, in which electrical circuit segments consisting of a resistor in series with an inductor and a capacitor represented arteries. In addition, the left ventricle was modelled by a synthesiser, and peripheral vessels were modelled by resistors (Noordergraaf, Verdouw and Boom, 1963).

With the development of technology and digital computers, the impedance method gained more interest and was further developed in the works of Taylor (1959), and Westerhof and colleagues (1971). However, a significant drawback of the impedance method was that it provided analysis in the frequency domain and could not provide information about the axial location of the events.

In 1971, Anliker and colleagues solved the nonlinear equations of Euler by using the methods of characteristics derived by Riemann (Anliker, Rockwell and Ogden, 1971). They

conducted a systematic study of different elements of the vascular system to reach a complete description of the arterial system using the method of characteristics.

Parker and Jones developed a new approach for studying waves in the early 90s. They hypothesised that arterial waves are constituted by the summation of forward (from the heart to the periphery) and backward (from the periphery to the heart) travelling waves and formulated a mathematical method to achieve their separation from arterial pressure and velocity waveforms (Parker and Jones, 1990) Later on, they proposed a novel index related to wave transmission called wave intensity.

Application of the computers assisted the process of solving the equations for pulse wave velocity; therefore, many scientists were able to solve the nonlinear formulations in the time domain (Anliker, Rockwell and Ogden, 1971; Stergiopoulos, Young and Rogge, 1992; Olufsen *et al.*, 2000). This could help scientists to study the wave propagation throughout the arterial system and bifurcations, also controlling the inflow and outflow boundary conditions.

1.2.2 WAVE PROPAGATION

The disturbance in a substance travels in time and space, and results in the exchange of energy from one form to another; this phenomenon is called wave propagation. In the cardiovascular system, the ventricular ejection produces a change in pressure and flow. The generated waves travel in the artery because of the energy exchange between the inertial force of blood and the elasticity of the arterial walls. It is widely accepted that blood can be approximated as an incompressible fluid in conduit vessels (Atabek and Lew, 1966; Pedley, 1980; Caro *et al.*, 2011). Therefore, the aorta and rest of the elastic arteries must distend in order to compensate for the sudden increase of blood volume caused by the ventricular ejection.

Consequently, the diameter of the inlet of the aorta increases with the increase of pressure to compensate for the increase. This action continues along the aorta and other elements of the arterial system and affects the pressure and blood velocity locally. The two main methods for studying the wave propagation in vessels are briefly explained below.

1) WAVE PROPAGATION IN THE FREQUENCY DOMAIN

As mentioned before, the initial approach for analysing the wave propagation was in the frequency domain. In this approach, the concept of impedance in electrical circuits is applied to the arterial system. Arterial impedance (Z) represents the ratio between pressure and flow. One of the conditions required for impedance analysis is considering the cardiovascular system in the steady-state. By using the impedance analysis, the arterial flow and pressure waveforms

can be decomposed into sinusoidal components with the appropriate frequencies, magnitudes and phase shifts. The impedance analysis can provide valuable information about the wave propagation in the closed arterial system; however, Parker (Parker, 2009) argues that, in general, the heart cannot be considered as a steady-state system, which contradicts one of the main assumptions in impedance analysis. Moreover, Mitchel (2009) claims this approach has several limitations. The main limitation is that Fourier series can reconstruct the amplitude and phases of the various frequencies, but not the information about the location or time of the event.

II) WAVE INTENSITY ANALYSIS

Wave intensity analysis is based on sound mechanical principles, i.e. the conservation of mass and momentum, and involves the general solution of the basic equations using the method of characteristics. It describes the energy flux carried by the waves per unit area. In 1988, Parker and his colleagues discovered that, despite the complexity of the mathematical methods, the results are surprisingly simple to apply (Parker *et al.*, 1988). The numerical methods are described in detail in Chapter 2.

The most crucial property of wave intensity, overcoming the drawback of impedance analysis, is that it is defined in the time domain, and therefore, relating the wave features to the temporal changes in measured pressure and velocity is feasible. Moreover, no assumption is made on the vessel's wall nonlinear behaviour, taking into account different viscoelastic properties of the wall, fluid viscosity, convective and frictional effect.

The wave intensity (dI) is defined merely as the product of the measured pressure (dP) and velocity (dU), and it separates waves into forward component, waves travelling from the left ventricle to periphery, and backward component, waves returning from distal locations due to changes in mechanical and geometrical properties of the conveying vessel.

Wave intensity has been used for the analysis of the physiological waves in the aorta (Koh *et al.*, 1998; Jones *et al.*, 2002; Khir and Parker, 2005; Li *et al.*, 2019), coronary arteries (Sun *et al.*, 2004; Davies *et al.*, 2006), and superficial arteries such as carotid, femoral, and brachial artery (Zambanini *et al.*, 2005; Borlotti *et al.*, 2012).

The mathematical formulation of wave intensity analysis requires the determination of the vessel wave speed, which is explained in section 1.2.3.

1.2.3 PULSE WAVE VELOCITY

The pulse wave velocity (PWV) or wave speed (c) is the speed at which a disturbance travels through the medium and provides crucial information about the mechanical properties of the arterial wall. The wave speed is directly related to the local distensibility of the vessel and could be of clinical importance. Practically, there are several developed approaches to determine the wave speed locally and in a single point. Some of the methods are described here briefly.

- *Moens-Korteweg*: As it was mentioned in 1.2.1, Korteweg and Moens worked on the estimation of the wave speed in elastic tubes, and they found the following relationship describing the wave speed for an incompressible fluid carried in a thinned wall tube

$$c_{MK} = \sqrt{\frac{Eh}{\rho D}} . \quad (1.2)$$

Where E is Young's modulus of the tube wall, h is the wall thickness, ρ is the fluid density and D is the diameter of the tube. (Korteweg, 1878)

- *Bramwell-Hill*: Derived from Moens-Kortewegs equation, the Bramwell-hill equation allows calculating local wave speed using vessel strain, blood density, and pulse pressure as

$$c_{BH} = \frac{1}{\sqrt{\rho \cdot Distensibility}} . \quad (1.3)$$

Distensibility is defined as changes in blood volume in a vessel over the volume multiplied by changes in pressure, i.e. $dV / (V \cdot dP)$. For the estimation of distensibility, changes in the cross-sectional area of the aorta can replace the volume variable as

$$Distensibility = \frac{\Delta A}{A_{minimal} \cdot \Delta P} . \quad (1.4)$$

A is the cross-sectional area, and ΔA and ΔP are the difference between maximal and minimal cross-sectional area and pressure respectively, in a cardiac cycle (Bramwell and Hill, 1922).

- *PU-loop*: In 2001, Khir et al. observed that, in early systole, there are no backward travelling waves and the changes in pressure and flow velocity are related to the forward wave only. The slope of the linear relationship between pressure and flow in this portion of the cardiac cycle is proportional to the local wave speed (Khir *et al.*, 2001).

$$c_{PUloop} = \frac{1}{\rho} \frac{dP_{\pm}}{dU_{\pm}} \quad (1.5)$$

(+) and (-) is the indication of the forward and backward directions, respectively.

- *Area-flow loop*: Based on the definition of the characteristic impedance, Rabben et al. used the ratio between the change in flow and change in cross-sectional area to estimate the pulse wave velocity during the reflection-free period of the cardiac cycle (Rabben *et al.*, 2004).

$$c_{QAloop} = \frac{dQ}{dA} \quad (1.6)$$

- *Sum of Squares*: Estimation of wave speed in coronary arteries was one of the main reason behind the development of the sum of squares method (Davies *et al.*, 2006).

$$c_{sq} = \sqrt{\frac{\sum(dP)^2}{\sum(dU)^2}} \quad (1.7)$$

- *LnDU-loop*: The LnDU-loop applies the same approach of the PU-loop; however, in this method, Feng and Khir substituted changes in pressure with changes of the logarithm form of the diameter. The changes in diameter in time could also be measured non-invasively with ultrasound imaging (Feng and Khir, 2010).

$$c_{lnDU} = \pm \frac{1}{2} \frac{dU_{\pm}}{d(\ln D)_{\pm}} \quad (1.8)$$

- *D²P-loop*: The calculation of wave speed in D²P-loop is based on the slope of the linear part of the loop in diastole. The slope is equal to $D_0/\rho c^2$ which D_0 is the mean arterial diameter and ρ stands for blood density. In this method, the arterial wall has Voigt-type and viscoelastic characteristics (Alastruey, 2011).

$$c_{D^2P} = D_0 \sqrt{\frac{dP}{\rho d(D^2)}} \quad (1.9)$$

In addition to methods mentioned above for the calculation of wave speed, which provide a local estimate for the pulse wave velocity in each cross-sectional area, a regional PWV can be estimated by foot-to-foot method, serving as a gold-standard method for clinical measurement of PWV.

- *Foot-to-foot*: this method relies on the standard definition of velocity as distance over travelling time. Similarly, acquiring arterial waves in two different locations of the arterial tree, the wave speed can be estimated as the ratio between the path length and the time difference between the arrival of the wave at the two locations. c_{fft} is calculated as $\Delta L / \Delta t$, where ΔL is the axial distance between the measurement sites, and Δt is the time it takes the wave to travel from one measurement site to the other. With c_{fft} , the foot of the wave is considered as the intersection point of the end-diastolic decline and early-systolic rise of the pressure waveform (Gaddum *et al.*, 2013).

1.3 COMPUTATIONAL MODELS

Numerical models provide tools to investigate blood flow and wave propagation inside the arterial system of the human body. It could play a crucial role in improving the diagnosis and treatment of pathologies related to the cardiovascular system. Using the computational models facilitate the untwining of the underlying mechanism of waves in the arterial tree, which might not be feasible to test in vivo due to physiological and ethical reasons.

There are three main methods for modelling the vascular system: 1) Three-dimensional models, based on Navier-stokes equations, 2) space-dependent one-dimensional models, based on Euler equations, 3) zero-dimensional or lumped parameter models established on electrical circuits laws.

In this section, there is a brief description of the available computational models that are used to study the blood flow in the arterial tree.

ZERO-DIMENSIONAL MODELS (0D)

In 0D models, the arterial segments are considered as compartments and homogenous. Each compartment can be related to blood flow in an organ such as the heart, structure of the vessels, or capillaries. Lumped parameter models have the ability to simulate the global response of the arterial system with a low computational cost. Moreover, only a few parameters representing the arterial tree are required for the simulation of distal parts, such as the capillary bed (Van de Vosse and Stergiopoulos, 2011).

The main paradigms of the lumped models were explained in section 1.2. Table 1.1 shows the relation between the electrical and the hydraulic application of 0D elements. There are elastic fibres present in the structure of the arterial wall, and their primary purpose is to transform the discontinuous and sudden changes of pressure, coming from the left ventricle, into steady and smoother changes. This smoothing mechanism is called the Windkessel (Wk) effect.

As mentioned in section 1.2.1, Otto Frank was the first one who developed a formulation for Wk effect by using two electrical circuit elements: a resistor (R) and a capacitor (C). The resistor represents the resistance to flow in the cardiovascular system, mainly in the small arteries and the arterioles; on the other hand, the capacitor characterized the compliance of the large arteries. A schematic representation of the relation of fire engines pump with the vascular system is presented in Figure 1.2.

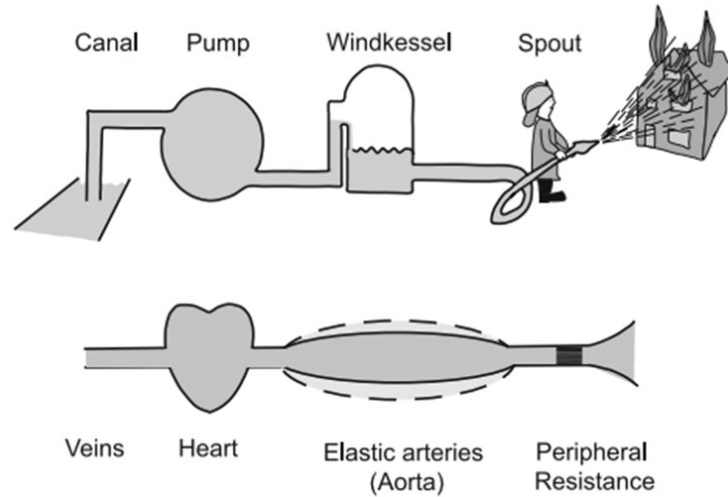


Figure 1. 2. The concept of Windkessel (Westerhof, Lankhaar and Westerhof, 2009)

The resistance, R , can be approximated as $R \approx P_{ao,mean}/CO$; With $P_{ao,mean}$ as the mean aortic pressure and CO as cardiac output. The value C can be calculated using the ratio of changes of volume, ΔV , and the resulting changes in pressure, ΔP , due to volume change. In other words, $C = \Delta V/\Delta P$ (Westerhof, Lankhaar and Westerhof, 2009).

This model could describe the behaviour of the arterial system during diastole when the aortic valve is closed. The changes of pressure in time during diastole has an exponential trend which equals to RC . This model was unable to capture the high-frequency components associated with pressure reflections in the arterial structure, and it is usually used to show an estimate of afterload on the heart or a simple terminal boundary condition for the distributed arterial network representations.

Moreover, the Wk model is unable to predict the relationship between pressure and flow in time during the systolic phase of the cardiac cycle. Therefore in 1971, Westerhof and his colleagues added a third element to this model.

The characteristic impedance, as shown in Figure 1.3 with Z_c is the third element, is connected in series with RC of Wk model. It can be seen as a link between the two-element model, and wave travel aspects of the arterial system since characteristic impedance equals wave speed multiplied by blood density divided by the aortic cross-sectional area (Westerhof, Elzinga and Sipkema, 1971).

Compared to 2-element Wk model, adding a simple resistance to 3-element Wk model improves the performance of the model in high frequencies, and many numerical and experimental studies have shown that 3-element Wk provides a better prediction of systolic and diastolic aortic pressure (Shi, Lawford and Hose, 2011).

To improve the accuracy of the three-element Wk model, Burattani and Gnudi proposed an inertance as the fourth element, which can represent all the inertances (L) in the arterial segments (Burattini and Gnudi, 1982). However, in practices, the four-element Wk model was difficult to estimate (Segers *et al.*, 2005; Burattini and Di Salvia, 2007). Hence, it is believed that the three-element Wk is more feasible and can model the global aspects of the arterial system (Westerhof, Lankhaar and Westerhof, 2009). Figure 1.3 depicts the Wk models with different numbers of elements and their arrangements.

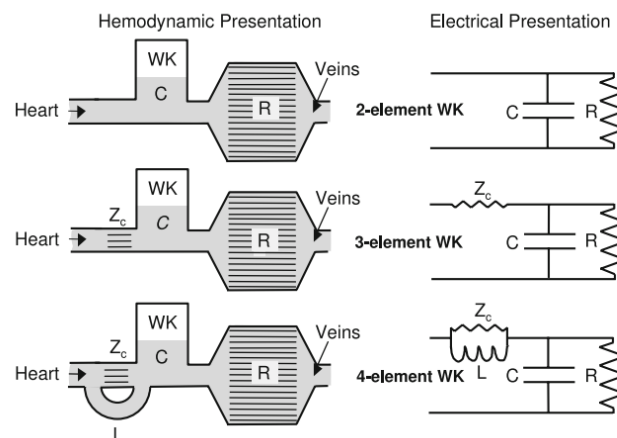


Figure 1. 3. The schematic of two-element, three-element, and four-element Windkessel models (Westerhof, Lankhaar and Westerhof, 2009).

The limitation of the Wk models is the inability to provide information about wave transmission, wave travel, blood flow distribution, and axial location of the reflected wave.

Table 1. 1. Relation of the electrical elements and their hydraulic application in Windkessel

Electric	Hydraulic
Voltage	Pressure
Current	Flow
Resistance (R)	Blood viscosity
Capacitance (C)	Wall compliance
Inductance (L)	Blood inertia

ONE-DIMENSIONAL MODELS (1D)

1D models are based on the physical principles of conservation of mass and momentum. In one-dimensional models, only the blood flowing in the axial direction is modelled, while other more complex motions are neglected. The arterial tree is simulated as a structure of flexible tubes that propagate the flow and pressure difference inside them. The effect of arterioles and

capillary beds on the blood flow is mostly modelled using the lumped parameter model or 0D models coupled to the terminal branches of the 1D model.

A 1D simulation is fast and allows researchers to include phenomena such as partial or total occlusions of arteries, which are not practicable on human subjects without surgical intervention. A detailed mathematical description of 1D models is provided in Chapter 2.

THREE-DIMENSIONAL MODELS (3D)

In 3D models, the vessels can be simulated with precise dimensions, and information such as shear stresses and the vorticity field can be calculated. Application of 3D models for the arterial system gives more precise information about the wave propagation inside a vessel. However, simulation of the complete arterial system is not feasible because of its computational cost and the number of variables that are required.

1.4 AIM AND OBJECTIVES

This overall goal of this thesis is to understand better the parameters affecting the pressure waveform observed in the aortic root. The aortic root is the most important site of the arterial system and having a direct effect on the left ventricle. Therefore, this work aims to study the magnitude and timing of arrival of reflected waves present in the aorta and the distance that a reflected wave can travel towards the aortic root.

Since two primary sources of reflection in the large arteries are bifurcations and tapering (Davies *et al.*, 2012), a systematic study on the effect of these reflection sources is performed. This investigation uses an existing one-dimensional model of pulse wave propagation within compliant vessels.

This specific objectives are to (i) quantify the reduction of pressure amplitude of reflections caused by bifurcations and tapering (ii) enhance our understanding about the alteration of pressure and velocity of a reflected wave travelling from distal limbs towards the aortic root, (iii) investigate the impact of tapering and the angle of tapering on wave speed and pressure waves, and explain the importance of the tapering in the arterial tree (iv) explain the results using the techniques that separate waves into their forward and backward components.

The ultimate goal of this research is to provide a better understanding of the influence of the geometrical structure of the aorta on the distance travelled by the reflected waves and their critical effect on the pressure waveform at the aortic root.

1.5 OUTLINE OF THE THESIS

Following the introduction in this chapter, with an overview of physiological and anatomical description of the arterial circulation and the wave propagation, the other chapters are organized as below:

In Chapter 2, a detailed description of the mathematical formulation of the one-dimensional wave propagation is provided.

In Chapter 3, different numerical models are used in order to study the effect of consecutive bifurcations on the pressure amplitude and the reflected waves. The results showed that with an increase in the number of bifurcations, a single reflection originating from periphery may not be sensed at the aortic root, due to reflections at bifurcations and being trapped between consecutive bifurcations. Hence, considering a single point origin for reflections can be an oversimplification of the phenomena happening in the physiological environment.

In Chapter 4, the pressure and velocity of a reflection pulse are studied on the route of the pulse to the ascending aorta in a validated arterial tree model. A pulse is induced from the left anterior tibial vessel, and the changes are numerically estimated across the iliac and the aorta. Both the pressure amplitude and the wave intensity of the wave reduced exponentially. Only 5 % of the pressure amplitude arrived at the distal abdominal aorta and is further reduced to 1 % in the aortic root. The pressure waves reflected more as they were travelling towards the aortic root. In contrast, the re-reflections were reflected less, suggesting that the tapering is enhancing the reflection of the reflected waves.

In Chapter 5, the focus is on the impact of tapering and the angle of tapering in the waves and the reflected waves. The complexity of the models used in Chapter 5 ranges from three vessels to a simple physiological model of the iliac bifurcation connected to the upper thoracic aorta. The results show that tapering causes an increase in the amplitude of pressure across the tapered vessel. The higher angle of tapering in a vessel can cause a higher pulse pressure and peak pressure. Finally, it is shown that in an ageing arterial tree, the angle of tapering, the peak pressure and the pulse pressure increases.

In Chapter 6, the analysis of Chapter 5 is further extended to an arterial tree with 55-segments. The arterial tree is modelled in tapered and non-tapered segments. At the same time, bifurcations have similar area ratio, i.e. reflection co-efficient, so that only the effect of taper be considered. First, the inflow is a physiological wave which is induced at the aortic root. The outcome shows higher pulse pressure and peak pressure in the tapered model compared to non-tapered one. Then, the inflow is induced from a distal location, namely left profunda femoris,

and the changes are monitored at the root of the aorta. The wave dissipation in the tapered model is higher than the non-tapered model.

Finally, Chapter 7 discusses the general outcome of this work, summarises the thesis achievements, and provides suggestions for future work.

CHAPTER 2

ONE-DIMENSIONAL CARDIOVASCULAR MODELS

The arterial system has a complex dynamic and many elements, therefore, an accurate representation of the flow and pressure in the whole system based on 3D models is beyond the capacity of current computers. Besides, constructing such models, and interpretation of its results is computationally costly and challenging.

On the other hand, 0D models can provide a global response of the arterial system and estimate the load on the heart with a relatively low computational cost. With these models, the entire response of arterial tree can be modelled by a resistor and a capacitor (Westerhof, Lankhaar and Westerhof, 2009), or multi-compartments to represent each part of arterial tree (Olufsen *et al.*, 2000). However, these models cannot provide information about the axial location of the waves.

1D models are simplified models exploiting global features of blood flow. Compared to the concise local dynamics models, these models are highly simplified. However, their results are reliable with low computational cost, and interpretation of the results is less challenging. 1D models can be used to model the whole systemic circulation (Westerhof *et al.*, 1969; Schaaf and Abbrecht, 1972; Avolio, 1980) or be focused on one part of the arterial system (Raines, Jaffrin and Shapiro, 1974; Balar, Rogge and Young, 1989; Peiro, Sherwin and Parker, 2003; Alastruey *et al.*, 2007; Willemet, Lacroix and Marchandise, 2011). More recently, the investigation using computational models are directed towards patient specific-conditions (Epstein *et al.*, 2015).

In 1D models, the Windkessel elements are used to show the resistance and compliance of the small arteries and arteriole.

2.1 ONE-DIMENSIONAL (1D) EQUATIONS

Several approaches have been used to derive the 1D model of a compliant pipe with an incompressible fluid flowing inside it. Some models are based on the incompressible Navier-Stokes equations (Peiró and Veneziani, 2009). The underlying assumption to such equations is that the ratio between the radius of the vessel, R_0 , and its length l is significantly small ($\frac{R_0}{l} \ll$

1). Therefore, asymptotically, the governing equations can be simplified by neglecting the higher-order terms in $\frac{R_0}{l}$ (Barnard *et al.*, 1966).

The second approach to 1D models consists in applying conservation principles. However, this type of models may considerably differ in feature due to choices made in the type of used boundary conditions, solving methodologies, and linear or non-linear assumptions (Stergiopulos, Young and Rogge, 1992).

2.1.1 DERIVATION OF GOVERNING EQUATIONS

The nonlinear 1D equations of blood flow in elastic vessels have been used to develop a computational model to trace waves as they travel through a simplified branching system as a surrogate of the arterial system.

An artery is modelled as a single compliant vessel with length l and with negligible local curvature. Therefore, changes can only occur in one axial direction by a Cartesian coordinate x . Figure 2.1 depicts a simple, compliant vessel and specifies changes of the variables along its axis. The area at each cross-sectional, S , is defined by $A(x, t) = \int_S d\sigma$. $d\sigma$ is the differential element of the area. Also, the average flow velocity and internal pressure at each cross-section are defined by $U(x, t) = \frac{1}{A} \int_S \hat{u} d\sigma$ and $p(x, t) = \frac{1}{A} \int_S \hat{p} d\sigma$, respectively. $\hat{u}(x, \sigma, t)$ and $\hat{p}(x, \sigma, t)$ designate the velocity flow and pressure within a constant x -section. Finally, the volume flux is described as $Q(x, t) = A(x, t)U(x, t)$ at given section S .

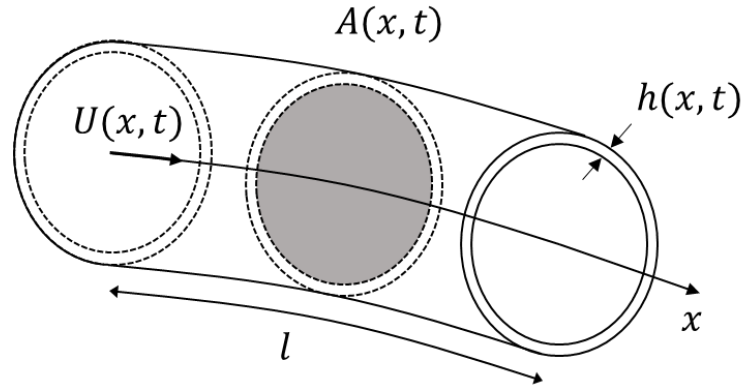


Figure 2. 1. A simple, compliant vessel with cross-sectional area A , wall thickness h , flow velocity U , and length l in 1D orientation.

In 1D models, the blood is assumed to be homogenous, incompressible and Newtonian, with a constant dynamic viscosity, μ , and density ρ . Furthermore, the effect of gravity on blood flow is not considered. As mentioned in section 1.1.2, by using the average diameter and velocity in large arteries in normal conditions, Reynold's number is below 2000. Hence, it is a reasonable

assumption to consider the blood flow to be laminar (Zamir, 2000; Pedley, 2003; Alastruey, 2006; Caro *et al.*, 2011).

Finally, it is assumed that area, flow velocity and pressure are constant at a section, which means there are three independent variables. Consequently, for finding these variables, three independent equations are needed: the conservation of mass (2.1.2) and momentum (2.1.3) and the relation between pressure and cross-sectional area (2.1.4).

2.1.2 CONSERVATION OF MASS EQUATION

The rate of change of mass within the vessel in Figure 2.1, which is an arbitrary control volume, should equal the net mass flux out of the control volume if it is assumed that there is no seepage through the side walls. The control volume of the vessel is defined as $V(t) = \int_0^l A(x, t) dx$, hence the conservation of the volume can be written as

$$\rho \frac{dV(t)}{dt} = \rho Q(0, t) - \rho Q(l, t). \quad (2.1)$$

Since the density of the blood (ρ) is assumed to be constant, Equation (2.1) can be divided by ρ . Moreover, by substituting $V(t)$ into Equation (2.1), the one-dimensional equation of mass conservation can be derived as

$$\frac{d}{dt} \int_0^l A(x, t) dx = - \int_0^l \frac{\partial Q}{\partial x} dx. \quad (2.2)$$

Assuming that the length of the vessel is independent of time, Equation (2.2) can be written as

$$\int_0^l \left(\frac{\partial A}{\partial t} + \frac{\partial Q}{\partial x} \right) dx = 0. \quad (2.3)$$

As the control volume is arbitrary, the integrand must be valid for any length (i.e. $l \in R$). Recalling $Q = AU$ the integrand of Equation (2.3) can also be written as

$$\frac{\partial A}{\partial t} + \frac{\partial(AU)}{\partial x} = 0 \quad (2.4)$$

2.1.3 CONSERVATION OF MOMENTUM EQUATION

Applying the conservation of momentum in the vessel represented in Figure 2.1 means that the rate of change of momentum within and the net flux of momentum out from the control volume must be equal to all of the applied forces on the control volume. The statement mentioned above can be written as

$$\frac{d}{dt} \int_0^l \rho Q dx + (\alpha \rho Q U)_l - (\alpha \rho Q U)_0 = F, \quad (2.5)$$

where F is the forces acting on the control volume in the x -direction, and α is the correction factor justifying the nonlinearity of the section integration of the local velocity \hat{u} ;

$$\int_S \rho (\hat{u})^2 d\sigma = \alpha \rho U^2 A = \alpha \rho U (UA) = \alpha \rho Q U \rightarrow \alpha = \frac{\int_S (\hat{u})^2 d\sigma}{AU^2} \quad (2.6)$$

The correction factor (α) allows the local velocity \hat{u} to vary in a cross-sectional area. In a straight vessel, the flow velocity is expected to be highest in the centre of the vessel and decreases as it gets close to the wall. With α , the shape of the velocity is taken into consideration. For example, if the flow has a uniform profile $\alpha = 1$, while for parabolic profile $\alpha = \frac{4}{3}$.

The right-hand side of the Equation (2.5) is the applied forces in the x -direction, consisting of pressure force and viscous force acting on the vessel. Therefore, this term can be written as

$$F = (pA)_0 - (pA)_l + \int_0^l \int_{\partial S} \hat{p} n_x ds dx + \int_0^l f dx, \quad (2.7)$$

where ∂S is the boundary of the section S , n_x is the x -component of the surface normal, and f is the frictional force per unit length. The double integral expression in Equation (2.7) stands for the sidewall pressure force and can be simplified by treating the vessel as axisymmetric and assuming uniform cross-sectional pressure (Peiro, Sherwin and Parker, 2003; Sherwin *et al.*, 2003), hence leading to

$$\int_0^l \int_{\partial S} \hat{p} n_x ds dx = \int_0^l p \frac{\partial A}{\partial x} dx. \quad (2.8)$$

If Equations (2.7) and (2.8) are combined, the equation is

$$\frac{d}{dt} \int_0^l \rho Q dx + (\alpha \rho Q U)_l - (\alpha \rho Q U)_0 = (pA)_0 - (pA)_l + \int_0^l p \frac{\partial A}{\partial x} dx + \int_0^l f dx. \quad (2.9)$$

To determine the one-dimensional differential momentum equation, it is noticeable that

$$(\alpha \rho Q U)_l - (\alpha \rho Q U)_0 = \int_0^l \frac{\partial(\alpha Q u)}{\partial x} dx, \quad (pA)_0 - (pA)_l = - \int_0^l \frac{\partial(pA)}{\partial x} dx. \quad (2.10)$$

Since ρ is assumed to be constant and l is independent of time and replacing the equations mentioned above in Equation (2.9) gives

$$\rho \int_0^l \left(\frac{\partial Q}{\partial t} + \frac{\partial(\alpha Q U)}{\partial x} \right) dx = \int_0^l \left(- \frac{\partial(pA)}{\partial x} + p \frac{\partial A}{\partial x} + f \right) dx. \quad (2.11)$$

Similar to the conservation of the mass, the integrands are valid for any arbitrary length l , and equal to each other. Therefore Equation 2.11 can be rewritten as

$$\rho \left(\frac{\partial Q}{\partial t} + \frac{\partial(\alpha QU)}{\partial x} \right) = \left(-\frac{\partial(pA)}{\partial x} + p \frac{\partial A}{\partial x} + f \right). \quad (2.12)$$

The first term of the right-hand side of Equation (2.12) can be replaced with its partial derivatives,

$$\frac{\partial(pA)}{\partial x} = p \frac{\partial A}{\partial x} + \frac{A \partial p}{\partial x}, \quad (2.13)$$

and upon insertion in Equation (2.12), the term $p \frac{\partial A}{\partial x}$ is cancelled out. Therefore, the 1D momentum equation can be simply written as

$$\frac{\partial Q}{\partial t} + \frac{\partial(\alpha QU)}{\partial x} + \frac{A \partial p}{\rho \partial x} = \frac{f}{\rho} \quad (2.14)$$

and recalling $Q = AU$, the momentum equation can be reformulated in terms of A and U ;

$$\frac{\partial(AU)}{\partial t} + \frac{\partial(\alpha AU^2)}{\partial x} + \frac{A \partial p}{\rho \partial x} = \frac{f}{\rho}. \quad (2.15)$$

This equation can be manipulated into

$$U \left[\frac{\partial A}{\partial t} + \frac{\partial(UA)}{\partial x} \right] + (\alpha - 1)U \frac{\partial(UA)}{\partial x} + A \left[\frac{\partial U}{\partial t} + \alpha U \frac{\partial U}{\partial x} \right] = -\frac{A \partial p}{\rho \partial x} + \frac{f}{\rho}, \quad (2.16)$$

where the first bracket consists of the conservation of mass equation (Eq. 2.4) and equal to zero. Therefore, rearranging equation (2.16)

$$\frac{\partial U}{\partial t} + (2\alpha - 1) U \frac{\partial U}{\partial x} + (\alpha - 1) \frac{U^2 \partial A}{A \partial x} + \frac{1 \partial p}{\rho \partial x} = \frac{f}{\rho A}. \quad (2.17)$$

The second and third terms on the left-hand side of Equation (2.17) stands for the convective inertia and account for a velocity profile which is uniform. However, these terms can be neglected because they have a significantly smaller value than the other terms, especially in large arteries where, under physiological conditions, the velocity profile is almost flat (Caro *et al.*, 2011). Therefore similar to reference (Brook, Falle and Pedley, 1999), the convective inertia expressions is neglected, and Equation 2.17 is reduced to

$$\frac{\overset{TA}{\partial \overline{U}}}{\partial t} + U \frac{\overset{CA}{\partial \overline{U}}}{\partial x} = -\frac{\overset{PG}{\partial \overline{P}}}{\rho \partial x} + \frac{\overset{VF}{\overline{f}}}{\rho A}, \quad (2.18)$$

where each term from right to left is accounting for viscous force per unit mass (VF), pressure gradient force per unit mass (PG), convective acceleration (CA), and temporal acceleration (TA) (Willemet and Alastruey, 2014).

Smith *et al.* (2002) derived the term f by integrating the incompressible 3D Navier-Stokes equations as

$$f = 2\mu \frac{A}{R} \left[\frac{\partial U}{\partial r} \right]_R. \quad (2.19)$$

μ denotes the viscosity of blood and, as mentioned in section 2.1.1, it is assumed to be constant and equal to 0.004 Pa s. Moreover, the shape of the velocity profile is assumed to be similar to the one described by Smith et al. (2002), which is

$$\hat{u}(x, \sigma, t) = \frac{\gamma + 2}{\gamma} U(x, t) \left[1 - \left(\frac{r}{R} \right)^\gamma \right], \quad (2.20)$$

where γ is constant for each flow profile, r is the radius from the centre line, and R is the radius of the vessel. Substituting Equation (2.19) into the momentum flux equation (Eq. 2.6) gives us an equation for γ , which is

$$\gamma = \frac{2 - \alpha}{\alpha - 1}. \quad (2.21)$$

Rewriting Equation (2.20) replacing γ yields to the flow profile with respect to α written as

$$\hat{u}(x, \sigma, t) = \frac{\alpha}{2 - \alpha} U(x, t) \left[1 - \left(\frac{r}{R} \right)^{\frac{2-\alpha}{\alpha-1}} \right]. \quad (2.22)$$

According to (Smith, Pullan and Hunter, 2002), the value of $\alpha = 1.1$ ($\gamma = 9$) is a compromise fit for experimental data, and in the numerical experiments described in this thesis, this value will be used. The velocity profile of $\alpha = 1.1$ is axisymmetric ($\frac{\partial u}{\partial r} \big|_{r=0} = 0$) and satisfies the no-slip condition ($u \big|_{r=R} = 0$). Figure 2.2 shows the velocity profile in a parabolic form and the form adopted by Smith et al. (2002).

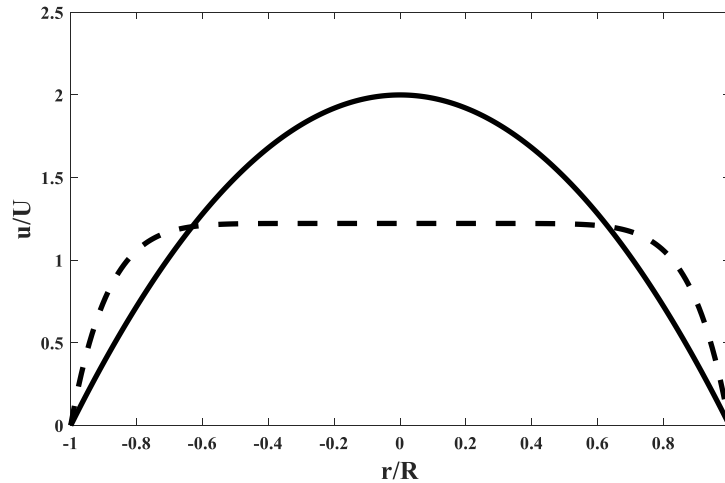


Figure 2. 2. The velocity profile estimated by Equation (2.20) in a parabolic form (solid line, $\gamma=2$) and used by Smith et al. (2002) (dashed line, $\gamma=9$)

Using the velocity profile shown in Figure 2.2 considers that the flow cannot reach to its fully developed state in physiological environment. Considering the human aorta, the entrance

length (the distance from the entrance required for a flow to become fully-developed) is approximately 94 cm (Caro *et al.*, 2011). 94 cm is greater than the normal length of the aorta and makes the whole aorta to be the entrance region. As a result, the velocity profile in the aorta will be approximately flat.

Finally, replacing Equation (2.22) in Equation (2.19) results in

$$f = -22\mu\pi U. \quad (2.23)$$

2.1.4 PRESSURE AND AREA RELATIONSHIP

For finding the mentioned three independent variables (p, U, A), another equation is required to close the system. Therefore, developing a relationship between area (A) and pressure (p) is necessary. The pressure-area relationship, or tube law, accounts for the interaction between the fluid and the conduit and has been modelled in different ways: linear pressure-area relationship (Raines, Jaffrin and Shapiro, 1974), nonlinear pressure-area model (Formaggia, Lamponi and Quarteroni, 2003; Peiro, Sherwin and Parker, 2003; Alastruey *et al.*, 2008, 2009; Alastruey, Kim H Parker and Sherwin, 2012) and finally nonlinear viscoelastic models (Holenstein, Niederer and Anliker, 1980; Alastruey *et al.*, 2011; Reymond *et al.*, 2011).

In this thesis, the lumen is modelled as circular with a thin, elastic, and homogenous wall. It is assumed that the vessel radius is far greater than the thickness of the walls ($R \gg h$). Hence, the external forces are limited to the stresses acting in the circumferential direction.

The circumferential tensile stress, σ , can be written as

$$\sigma = \frac{R_0(p - p_0)}{h}, \quad (2.24)$$

where R_0 and p_0 denotes the radius and pressure at the reference state, and the corresponding elastic strain, ϵ , can be written as (Atabek, 1968)

$$\epsilon = \frac{1}{1 - \nu^2} \frac{R - R_0}{R_0}. \quad (2.25)$$

where ν is Poisson's ratio, which describes the ratio between the strain in the axial and circumferential direction. Since arteries are mostly incompressible, Poisson's ratio is 0.5 (Weizsacker and Pinto, 1988). This equation is considering the effect of tethering in an in vivo state. Tethering, which is the effect of surrounding tissues on the movement of the arterial wall, influences the motion of the wall in longitudinal and radial directions; in the in vivo environment, the longitudinal motion is assumed to be almost zero (Atabek, 1968).

Considering the stress-strain equation for linear elastic materials $\sigma = E\epsilon$, the last two equations can be connected to each other. E is Young's modulus, yielding to the tube law used in the 1D model

$$P = P_0 + \frac{\beta}{A_0}(\sqrt{A} - \sqrt{A_0}). \quad (2.26)$$

A_0 is the initial area condition where $(P, U) = (P_0, 0)$. $\beta(x)$ represents the material properties of the elastic vessel, is space-dependent and can be expressed as a function of Young's modulus and wall thickness as (Alastruey, Kim H. Parker and Sherwin, 2012)

$$\beta = \frac{\sqrt{\pi} E h}{(1 - \nu^2) A_0}. \quad (2.27)$$

The viscoelastic behaviour of the arterial wall has been described in several works (Holzapfel, Gasser and Stadler, 2002; Alastruey *et al.*, 2011; Wang, Golob and Chesler, 2016). Nonetheless, the elastic wall models are preferable due to simplicity. Moreover, considering the viscoelastic behaviour of the wall would require accounting for the viscoelastic properties of the blood, hence coupling both wall and blood flow dynamics and adding more complexity to the numerical models (Ghigo *et al.*, 2017).

2.2 THE METHOD OF CHARACTERISTICS

The method of characteristics is an approach for solving partial differential equations (PDE). With this technique, the variables can be reduced to one independent variable or an ordinary differential equation (ODE).

If the tube law (Eq. 2.26) is applied to the momentum equation (2.18), the resulting equation will be:

$$\frac{1}{\rho} \frac{\partial p}{\partial x} = \frac{1}{\rho} \left(\frac{\partial p}{\partial A} \frac{\partial A}{\partial x} + \frac{\partial p}{\partial \beta} \frac{d\beta}{dx} + \frac{\partial p}{\partial A_0} \frac{dA_0}{dx} \right) \quad (2.28)$$

The 1D equations for conservation of mass (Eq. 2.4) and momentum can be written in quasi-linear matrix form

$$\frac{\partial U}{\partial t} + H \frac{\partial U}{\partial x} = S, \quad (2.29)$$

where

$$U = \begin{bmatrix} A \\ U \end{bmatrix}, \quad H = \begin{bmatrix} U & A \\ \frac{1}{\rho} \frac{\partial p}{\partial A} & U \end{bmatrix}, \quad S = \begin{bmatrix} 0 \\ \frac{1}{\rho} \left(\frac{f}{A} - \frac{\partial p}{\partial \beta} \frac{d\beta}{dx} - \frac{\partial p}{\partial A_0} \frac{dA_0}{dx} \right) \end{bmatrix}.$$

If the wave speed is $c = \sqrt{\frac{A}{\rho} \frac{\partial p}{\partial A}}$, then the term $\frac{1}{\rho} \frac{\partial p}{\partial A}$ in the matrix H can be rewritten as c^2/A .

With the assumption that $A > 0$, which is a necessary condition for having a physically relevant solution, the counter-diagonal elements of H are positive, and results in two real eigenvalues

$$\lambda_{f,b} = U \pm c. \quad (2.30)$$

Under physiological flow conditions, c is much higher than U , hence $\lambda_f = U + c > 0$ and $\lambda_b = U - c < 0$. Hence, λ_f and λ_b are speeds which pressure and velocity waveforms travel in the forward and backward directions, respectively. Pulse wave velocity can also be written in relation to the wall's mechanical properties (β) as

$$c = \sqrt{\frac{\beta}{2\rho A_0}} A^{\frac{1}{4}}. \quad (2.32)$$

The matrix H is diagonalisable and can be re-written as

$$H = L^{-1} \Lambda L, \quad (2.33)$$

where

$$L = \xi \begin{bmatrix} \frac{c}{A} & 1 \\ -\frac{c}{A} & 1 \end{bmatrix}, \quad \Lambda = \begin{bmatrix} \lambda_f & 0 \\ 0 & \lambda_b \end{bmatrix}.$$

ξ is an arbitrary scaling factor and, based on the work by Peiró and his colleagues (Peiro, Sherwin and Parker, 2003), ξ is equal to 1. If the Equation (2.33) is substituted in (2.29) instead of H , then multiplying L to the equation yields to

$$L \frac{\partial U}{\partial t} + \Lambda L \frac{\partial U}{\partial x} = LS. \quad (2.34)$$

The characteristic variables can be determined by integration of

$$\frac{\partial W}{\partial U} = L, \quad (2.35)$$

where $W = [Wf \quad Wb]^T$ is the vector of characteristic or Riemann variables, Equation (2.34) is reduced to

$$\frac{\partial W}{\partial t} + \Lambda \frac{\partial W}{\partial x} = LS. \quad (2.36)$$

If $\hat{x}(t)$ is defined as a parametric function in the (x, t) space, then the variation of W along the path of $\hat{x}(t)$ is written as

$$\frac{dW(\hat{x}(t), t)}{dt} = \frac{\partial W}{\partial t} + \frac{d\hat{x}}{dt} \Lambda \frac{\partial W}{\partial \hat{x}}. \quad (2.37)$$

By comparing the two Equations (2.13) and (2.14), it can be noticed that if $\frac{d\hat{x}}{dt} I = A$, then $\frac{dW}{dt} = LS$ along the path $\hat{x}(t)$. Hence, $\hat{x}(t)$ defines the characteristic path along which the information contained in W propagates in the (x, t) space. If in Equation 2.36 we consider the friction force to be negligible ($f = 0$), and β and A_0 are constant along x then $S = 0$. Hence, system 2.36 becomes decoupled, resulting in constant W_f and W_b along the characteristic curves. The two characteristic paths are

$$\frac{d\hat{x}}{dt} = \lambda_{f,b} = U \pm c. \quad (2.38)$$

Figure 2.3 depicts the characteristics of the system in x and t space.

Integrating Equation (2.35) gives us the characteristic variables can be written as

$$W_{f,b} = U - U_0 \pm \int_{A_0}^A \frac{c}{A} dA. \quad (2.39)$$

By applying the tube law (2.4, 2.5), the equations mentioned above can be solved as:

$$W_f = U - U_0 + 4(c - c_0), \quad (2.40)$$

$$W_b = U - U_0 - 4(c - c_0). \quad (2.41)$$

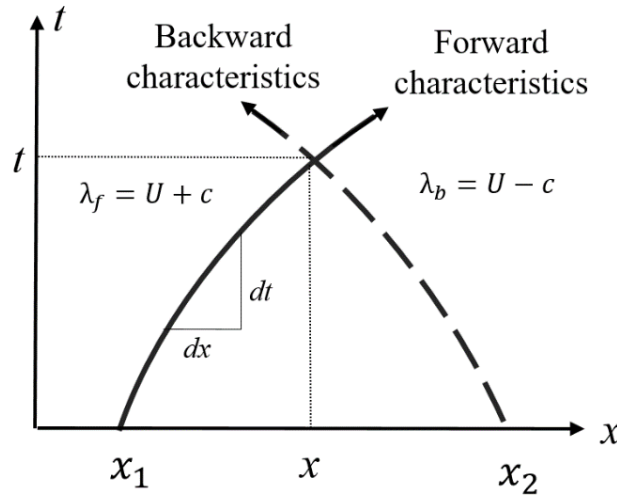


Figure 2. 3. Definition sketch of forward and backward characteristics. Every point (x,t) is intersected by a unique pair of characteristics curves

$$W_f = U - U_0 + 4(c - c_0), \quad (2.40)$$

Inserting Equation (2.32) into Equations (2.40) and (2.41) gives an explicit form of W (Sherwin *et al.*, 2003) as

$$W_{f,b} = u \pm 4 \sqrt{\frac{\beta}{2\rho}} \left(A^{\frac{1}{4}} - A_0^{\frac{1}{4}} \right). \quad (2.42)$$

With the help of the method of the characteristics described above, the Water-hammer equation can be derived, relating the variations of pressure (P) to variations of velocity (U) across a wavefront. If β and A_0 are considered to be constant along the axial direction, Equation 2.32 can be written as $c = \sqrt{\frac{1}{\rho D}} = \sqrt{\frac{A}{\rho} \frac{\partial p}{\partial A}}$. Rearranging the previous equation gives $\frac{c}{A} dA = \frac{dp}{\rho c}$.

Since changes of variables are defined in Equation 2.35 as $dW = LdU$,

$$dW_f = dU + \frac{dp}{\rho c}, \quad (2.43a)$$

$$dW_b = dU - \frac{dp}{\rho c}. \quad (2.43b)$$

Solving the above-mentioned equation for dP and dU gives us

$$\begin{aligned} dp &= \rho c \frac{dW_f - dW_b}{2}, \\ dU &= \frac{dW_f + dW_b}{2}. \end{aligned} \quad (2.44)$$

And the Water hammer equation is derived as

$$dp_{f\&b} = \pm \rho c dU_{f\&b} \quad (2.45)$$

2.3 LINEARIZATION OF THE EQUATIONS

The nonlinear dependency of p on A through the pressure-area relationship and the nonlinear viscous term $\frac{f}{\rho A}$ makes the system (2.29) not linear. Also, the convective term in the momentum equation $U \frac{\partial U}{\partial x}$ is adding to the nonlinearity of the system (2.29). Therefore, a reference state is defined where $(A, P, U) = (A_0, 0, 0)$ and introducing a small perturbation $\Delta a, \Delta p$ and Δu changes Equation (2.29) to

$$\frac{\partial \Delta U}{\partial t} + H_0 \frac{\partial \Delta U}{\partial x} = S_0, \quad (2.46)$$

where

$$\Delta U = \begin{bmatrix} \Delta a \\ \Delta u \end{bmatrix}, \quad H_0 = \begin{bmatrix} 0 & A_0 \\ \frac{1}{2\rho} \frac{\beta}{A_0^{\frac{3}{2}}} & 0 \end{bmatrix}, \quad S = \begin{bmatrix} 0 \\ \frac{1}{\rho} \left(\frac{f_0}{A_0} - \frac{\partial \Delta p}{\partial \beta} \frac{d\beta}{dx} - \frac{\partial \Delta p}{\partial A_0} \frac{dA_0}{dx} \right) \end{bmatrix}.$$

The friction force is changed to $f_0 = -22\mu\pi\Delta u$ and $\frac{\partial \Delta p}{\partial \Delta a}$ is approximated to $\frac{\partial \Delta p}{\partial \Delta a} \Big|_{\Delta a=0} = \frac{\beta}{2A_0^{\frac{3}{2}}}$, which can be rewritten as

$$\Delta p = \frac{\beta}{2A_0^{3/2}} \Delta a = \frac{\rho(c_0)^2}{A_0} \Delta a \quad (2.47)$$

where $c_0 = \sqrt{\frac{\beta}{2\rho}} A_0^{\frac{1}{4}}$.

The characteristic analysis of System (2.45) gives the linear characteristics function ΔW_f and ΔW_b ,

$$\Delta W_f = \Delta u + \frac{c_0}{A_0} \Delta a, \quad (2.48)$$

$$\Delta W_b = \Delta u - \frac{c_0}{A_0} \Delta a, \quad (2.49)$$

propagating in the (x, t) space with constant speeds $-c_0$ and $+c_0$. The linear characteristic paths are straight lines as

$$\frac{d\hat{x}_{f,b}}{dt} = \pm c_0. \quad (2.50)$$

2.4 NUMERICAL SOLUTION

Different numerical methods can be applied for solving the 1D blood flow equations mentioned in this chapter. The numerical schemes in the time domain are desirable since they provide comprehensive information in the time domain and give information about the axial distance. These schemes include the method of characteristics (Anliker, Rockwell and Ogden, 1971; Schaaf and Abbrecht, 1972; Stettler, Niederer and Anliker, 1981), finite volumes (Müller and Toro, 2013; Montecinos, Müller and Toro, 2014), finite element methods such as continuous and discontinuous Galerkin (Sherwin *et al.*, 2003; Bessems, Rutten and Van De Vosse, 2007; Mynard, Penny and Smolich, 2008; Alastruey, Kim H Parker and Sherwin, 2012) and Taylor-Galerkin (Formaggia, Lamponi and Quarteroni, 2003), finite differences such as Lax-Wendroff (Olufsen *et al.*, 2000; Azer and Peskin, 2007) and the MacCormack methods (Hellevik *et al.*, 2009; Saito *et al.*, 2011). A study in 2015 confirmed that all these methods are in good agreement with each other in estimating pressure and area changes in large arteries (Boileau *et al.*, 2015).

In this thesis, the nonlinear system of 1D equations (Eq. 2.29) is solved using the discontinuous Galerkin scheme, with high-order 1D spectral/*hp* element spatial discretisation. According to (Karniadakis and Sherwin, 2007), this method is convenient for the 1D formulation and can propagate waves with different frequencies with fast convergence and good dispersion properties. More details about the numerical discretisation can be found in (Peiro, Sherwin and Parker, 2003; Sherwin *et al.*, 2003; Karniadakis and Sherwin, 2007).

2.5 LUMPED PARAMETER MODELS

In this section, the lumped parameter models (0-D) used in this thesis are explained. 1D governing equations can be reduced to zero-dimensional as

$$\begin{cases} \frac{\partial \Delta a}{\partial t} + A_0 \frac{\partial \Delta u}{\partial x} = 0, \\ \frac{\partial \Delta u}{\partial t} + \frac{1}{\rho} \frac{\partial \Delta p}{\partial x} = -\frac{8\pi\mu\Delta u}{\rho A_0}. \end{cases} \quad (2.51)$$

Assumptions are that β and A_0 are constant throughout the arterial domain, and the generic velocity profile (Eq. 2.20) is defined with $\gamma = 2$, which better approximated the velocity profile in small arteries (Olufsen *et al.*, 2000).

$$\begin{cases} C \frac{dP_{in}}{dt} + Q_{out} - Q_{in} = 0, \\ L \frac{dQ_{out}}{dt} + RQ_{out} + P_{out} - P_{in} = 0, \end{cases} \quad (2.52)$$

where $Q_{in} = Q(0, t)$, $Q_{out} = Q(L, t)$, $P_{in} = P(0, t)$, $P_{out} = P(L, t)$. $R = \frac{8\pi\mu l}{A_0^2}$, $L = \frac{\rho l}{A_0}$ and $C = \frac{A_0 l}{\rho(c_0)^2}$ are the resistance to flow and blood inertia and wall compliance they are equivalent to their electrical element.

2.5.1 TERMINAL RESISTANCE (R)

In this model, only the resistance of the peripheral vascular system is modelled. This model assumes $L = 0$ and $C = 0$. Therefore, the Equation (2.52) yields to

$$Q_{out} = Q_{in} = Q = A^*U^* = \frac{(P_{in} - P_{out})}{R} \quad (2.53)$$

If there is only a resistance coupled to a 1D model the reflection coefficient can be defined as

$$R_t = \frac{R - Z_0}{R + Z_0} \quad (2.54)$$

Z_0 denotes the characteristic impedance of terminal segments of the 1D model calculated as $Z_0 = \frac{\rho c}{A_0}$.

2.5.2 TWO ELEMENT WINDKESSEL MODELS (RC)

This model adds one compliance (C) to the resistance (R) defined before, while keeping inductance at zero; $L = 0$. The Equations (2.52) changes to

$$C \frac{dP_{in}}{dt} + \frac{P_{in} - P_{out}}{R} - Q_{in} = 0. \quad (2.55)$$

2.5.3 THREE ELEMENT WINDKESSEL MODELS (RCR)

This model provides a better estimation of terminal boundary condition, and it avoids non-physiological wave reflections in the microcirculation. The added R can be calculated as $R_m = \frac{P_{in} - P_C}{Q_{in}}$, where P_C is the pressure across the compliance C . For the RC block, the following system is considered

$$\begin{cases} C \frac{dP_C}{dt} + Q_{out} - Q_{in} = 0, \\ RQ_{out} + P_{out} - P_{in} = 0, \end{cases} \quad (2.56)$$

2.6 INTERFACES

In this section, the modelling of junctions and connections between segments are briefly explained.

2.6.1 INFLOW/OUTFLOW BOUNDARY CONDITIONS

The 1D formulation allows us to define an inflow boundary condition as time-dependent area change $A(t)$, velocity change $U(t)$, or flow rate $Q(t)$. The outflow of the heart can be modelled as lumped parameter model of the left ventricle (Mynard and Smolich, 2014), the entire heart (Formaggia *et al.*, 2006; Reymond *et al.*, 2011) and the aortic valve (Sherwin *et al.*, 2003; Matthys *et al.*, 2007).

Within this work, the inflow of the arterial system is defined as a flow rate $Q_{in}(t)$, which has been widely used in the literature (Alastruey, 2006; Epstein *et al.*, 2015; Willemet, Vennin and Alastruey, 2016). Generally, the origin of the inflow in the arterial network is the heart which is initiated in the left-hand side of the initial segment. In this thesis, other than considering the inflow generated from the heart, the inflow can be prescribed for a peripheral location, i.e. right-hand side of the terminal segment.

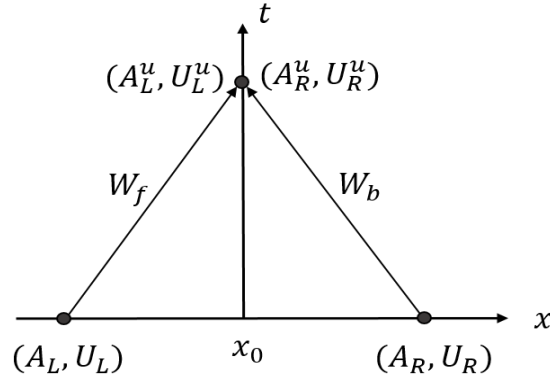


Figure 2. 4. Layout of the Riemann problem which takes into account the characteristic information reaching to both sides of the interface (x_0) and calculates the upwind states (A_L^u, U_L^u) and (A_R^u, U_R^u) originated from the discontinuity between two initial states (A_L, U_L) and (A_R, U_R) .

The solution of the Riemann problem neglects the characteristics moving away from the interface and only considers the information arriving at the interface, i.e. the upwind state. At time t , an interface has two constant states, (A_L, U_L) and (A_R, U_R) as illustrated in Figure 2.4.

For example, if the inflow is injected from the left-hand side (A_L, U_L) represents the current variables, and (A_R, U_R) is the initial state of the vessel. W_f and W_b are the characteristic variables for the forward and backward directions.

The states are located at the end region of the left element (L as a subscript) and the initial point of the elemental region on the right (R as a subscript). The characteristic paths at the interface can be written as

$$W_f(A_L, U_L) = W_f(A_L^u, U_L^u), \quad (2.57)$$

and

$$W_b(A_R, U_R) = W_b(A_R^u, U_R^u). \quad (2.58)$$

W_f and W_b are derived from Equation (2.40) and (2.41). With the law of conservation of mass and continuity of total pressure at the interface,

$$A_L^u U_L^u = A_R^u U_R^u, \quad (2.59)$$

$$\rho \frac{(U_L^u)^2}{2} + p(A_L^u) = \rho \frac{(U_R^u)^2}{2} + p(A_R^u). \quad (2.60)$$

The same formulation can be solved if the inflow is arriving at the interface from the right and moving to the left side of the interface. For more information about the interface connection, the reader is referred to (Alastruey, 2006).

At the outlet of the models that are used within this work, different boundary conditions are used. The lumped parameter models are explained in Section 2.5. Also, complete absorption

and blockage are used in some simulations where waves are completely absorbed or completely reflected. More explanation about the complete absorption and blocked ends are given in section 2.8.

2.6.2 SPLITTING FLOW

The type of junction which is used in this thesis is vessel splitting into two vessels, as shown in Figure 2.5. At a bifurcation, the parent vessel is separated into two daughter vessels. Therefore, it is necessary to solve the characteristic variables at the given boundary. The initial state for the parent vessel (1), and daughter vessels (2 and 3) are considered to be (A_1, P_1, U_1) , (A_2, P_2, U_2) , and (A_3, P_3, U_3) .

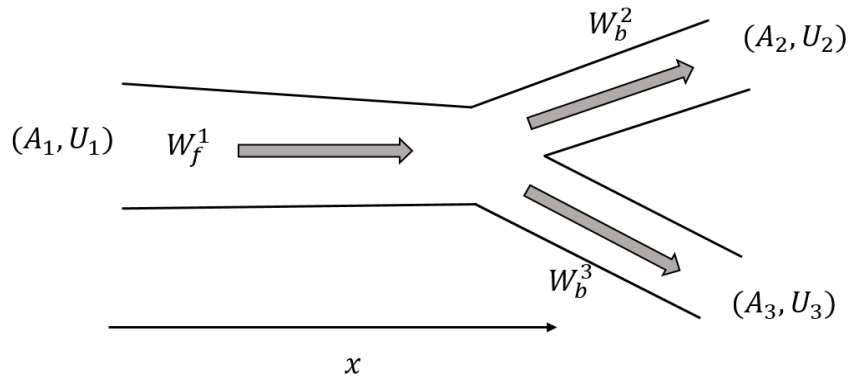


Figure 2. 5. Schematic representation of a bifurcation.

If the blood flow is assumed to be inviscid, then the system can be described in terms of forward and backward characteristic variables as

$$W_f(A_1^u, U_1^u) = W_f(A_1, U_1), \quad (2.61)$$

$$W_b(A_2^u, U_2^u) = W_b(A_2, U_2), \quad (2.62)$$

$$W_b(A_3^u, U_3^u) = W_b(A_3, U_3). \quad (2.63)$$

W_f and W_b are defined as Equations (2.40) and (2.41), respectively. Since the bifurcation is defined at the splitting point and no blood flow is exiting from the system, it is possible to write $Q_1 = Q_2 + Q_3$, and $Q = AU$ (Olufsen, 1999).

$$A_1^u U_1^u = A_2^u U_2^u + A_3^u U_3^u. \quad (2.64)$$

Bernoulli's law, which governs the continuity of total pressure (dynamic and static) (Alastruey *et al.*, 2012), gives us the second governing rule at the splitting junctions as

$$p_{(A_1^u)} + \frac{1}{2} \rho (U_1^u)^2 = p_{(A_2^u)} + \frac{1}{2} \rho (U_2^u)^2, \quad (2.65)$$

$$p_{(A_1^u)} + \frac{1}{2} \rho (U_1^u)^2 = p_{(A_3^u)} + \frac{1}{2} \rho (U_3^u)^2. \quad (2.66)$$

The Equations (2.59) to (2.64) are solved at each junction using the Newton-Raphson method. For more information about the solution of abovementioned equations reader is referred to (Alastruey, 2006; Alastruey, Kim H Parker and Sherwin, 2012). Other than the mentioned method, there are different methods for modelling bifurcations (Anliker, Rockwell and Ogden, 1971; Stettler, Niederer and Anliker, 1981; Olufsen, 1999). It worth mentioning that for pulsatile flow in elastic vessels where the flow is dominated by viscous flow the Bernoulli's law, derived for steady flow in rigid pipes, is violated (Olufsen *et al.*, 2000). Hence, the assumption of pressure continuity in bifurcations can provide a better approximation with accounting for some loss of energy (Anliker, Rockwell and Ogden, 1971; Stergiopoulos, Tardy and Meister, 1993).

In this work, the angle of bifurcation and the energy losses at the junctions are neglected, which represent a limitation in this study. However, research reported that the effect of the bifurcation angle on reflections at junctions is negligible (Westerhof *et al.*, 1969). Some studies in the literature modelled the energy losses as a function of flow rate and bifurcation angles (Stettler, Niederer and Anliker, 1981; Formaggia, Lamponi and Quarteroni, 2003; Steele *et al.*, 2003).

2.7 WAVE SEPARATION AND WAVE INTENSITY

Waves can be separated into their forward and backward components in the frequency domain (Westerhof *et al.*, 1972) and the time domain (Laxminarayan, 1979). The forward component is propagating with speed of $U + c$ in the forward direction, and the backward component is propagating with speed of $U - c$ in the backward direction. Waves can be linearly separated as $dP = dP_f + dP_b$ and $dU = dU_f + dU_b$ (Parker and Jones, 1990; Matthys *et al.*, 2007; Alastruey *et al.*, 2011).

By applying the Water-hammer equation (Eq. 2.45) to the equations as mentioned above, the forward and backward pressure and velocity are given as

$$dP_{f,b} = \frac{1}{2}(dP \pm \rho c dU), \quad dU_{f,b} = \frac{1}{2}\left(dU \pm \frac{dP}{\rho c}\right). \quad (2.67)$$

The nonlinear separation of the wavefronts is also studied in (Stergiopoulos, Tardy and Meister, 1993; Pythoud, Stergiopoulos and Meister, 1996; Mynard *et al.*, 2012). However, Pythoud and colleagues explained that the theoretical results of linear and nonlinear wave separations show a relatively small 5-10 per cent difference (Pythoud, Stergiopoulos and Meister, 1996).

Equation (2.67) is widely used in Wave Intensity Analysis (WIA). WIA studies the flux of energy carried by the wave per cross-sectional area, and it is represented as dI and calculated with

$$dI_{f,b} = dP_{f,b}dU_{f,b} = \pm \frac{1}{4\rho c} (dP \pm \rho cdU)^2 \quad (2.68)$$

The SI unit is W/m^2 . The wave intensity for forward travelling waves is positive ($dI > 0$) and for backward travelling waves is negative ($dI < 0$). Table 2.1 presents different wave intensities and the variation of the pressure and velocity affecting it.

Table 2. 1. Forward and backward waves, signs of the waves and their function

		Compression wave	Expansion wave
Forward waves	Pressure	$dP > 0$	$dP < 0$
	Velocity	$dU > 0$	$dU < 0$
	Wave Intensity	$dI > 0$	$dI > 0$
Backward waves	Pressure	$dP > 0$	$dP < 0$
	Velocity	$dU < 0$	$dU > 0$
	Wave Intensity	$dI < 0$	$dI < 0$

In normal physiological conditions, during early systole, a forward compression wave (FCW) is produced by the left ventricle contraction and increases both pressure and blood velocity (Khir *et al.*, 2001; Zambanini *et al.*, 2005; Kolyva and Khir, 2015). With the arrival of reflections, the second wave to appear is the backward compression wave (BCW). Then, in late-systole, both pressure and blood velocity decrease due to the closure of the aortic valve, resulting in the third wave: a forward expansion wave (FEW). Another FCW is expected during aortic valve closure due to a brief increase in pressure.

The distinct advantages of WIA are: 1) being a time-domain based analysis, which provides comprehensive information about the timing of the events. 2) There is no assumption about the vessel's wall linearity and the effects of viscoelasticity, convection, and friction is also taken into account. 3) It considers the effect and time of waves travelling in the forward direction as well as the backward direction (Parker and Jones, 1990; Khir and Parker, 2002). This method has been widely used in *in-vitro* (Khir and Parker, 2002; Feng, Long and Khir, 2007; Khir *et al.*, 2007; Feng and Khir, 2008, 2010; Hacham and Khir, 2019) and *in-vivo* experiments. WIA is studied in different location of arterial tree such as the aorta (Koh *et al.*, 1998), coronary

arteries (Broyd *et al.*, 2017), carotid (Zambanini *et al.*, 2005; Borlotti *et al.*, 2012; Chiesa *et al.*, 2019), femoral artery (Borlotti *et al.*, 2012), pulmonary circulation (Lau *et al.*, 2014; Su *et al.*, 2017), and venous circulation (Wang *et al.*, 2006).

2.8 LINEAR ANALYSIS OF WAVE REFLECTIONS

When an incident wave reaches a reflection site, part of it reflects in the other direction, and the rest is transmitted in the same direction. The factor quantifying the amount of reflected wave is known as reflection coefficient, usually shown by R_f . A reflection coefficient can be measured with different approaches:

a) Considering the changes of pressure in a junction. $R_f = \delta P / \Delta P$ where δP and ΔP are the magnitudes of the reflected wave and incident wave, respectively.

b) Using the Impedance of the elements (inductance) $Y_0 = \frac{\rho c}{A}$

$$R_f(\text{Parent}) = \frac{(A_p/c_p) - (A_{D1}/c_{D1}) - (A_{D2}/c_{D2})}{(A_p/c_p) + (A_{D1}/c_{D1}) + (A_{D2}/c_{D2})} \quad (2.69)$$

$$R_f(\text{Daughter 1}) = \frac{(A_{D1}/c_{D1}) - (A_p/c_p) - (A_{D2}/c_{D2})}{(A_p/c_p) + (A_{D1}/c_{D1}) + (A_{D2}/c_{D2})} \quad (2.70)$$

$$R_f(\text{Daughter 2}) = \frac{(A_{D2}/c_{D2}) - (A_p/c_p) - (A_{D1}/c_{D1})}{(A_p/c_p) + (A_{D1}/c_{D1}) + (A_{D2}/c_{D2})} \quad (2.71)$$

where A and c are cross-sectional areas and wave speeds in the vessels, and the subscripts stand for Parent, Daughter 1, and Daughter 2 vessels. In this thesis, the reflection coefficient is mainly calculated using Equations 2.69- 2.70.

The equations mentioned above shows that a reflection coefficient at a bifurcation depends on the route and direction of the wave. For example, in chapter 3, the inflow is injected from the endpoint of a daughter vessel (in backward direction), and the wave reaches to bifurcation from the daughter vessel. In this case, the reflection coefficient is calculated by either Equation 2.70 or 2.71, which would be completely different from the reflection coefficient for the waves that are travelling from the parent vessel towards the daughter vessels (forward direction).

The reflection coefficient can be calculated in a junction between two consecutive tubes with different properties using the equations as mentioned above, considering one of the daughter tubes properties to be zero, in other words, $A_{D2}/c_{D2} = 0$. Table 2.2 summarises the types of reflection coefficients and their corresponding values.

Table 2. 2. Types of reflection coefficient and their corresponding values

Reflection type	Open-end	Closed-end	Absorption/ no reflection	Negative reflection	Positive reflection
R_f	-1	1	0	$-1 < R_f < 0$	$0 < R_f < 1$

The transmission coefficient (i.e. the parameter quantifying the amount of wave transmitted downstream of a bifurcation) is related to the reflection coefficient and calculated as $T = 1 + R_f$.

In bifurcations, if the wave speeds and cross-sectional areas are known, the reflection coefficient can be easily found. However, for a general discussion using an assumption for the relationship of wave speed and area can give us a reflection coefficient (R) that can be only expressed by using the cross-sectional area (A) of the vessels. Using the Moens-Korteweg equation (2.32), it is reasonable to assume that $c \sim A^{\frac{1}{4}}$ in a thin-walled, uniform tube with a constant product value of elastic modulus and wall thickness. The ratio between the areas of the daughter's vessels to the parent vessel is defined as $\alpha = (A_{D1} + A_{D2})/A_p$.

FRAMEWORK OF COMPUTATIONS

All the numerical models in this thesis are solved in a numerical platform called Nektar, developed in King's College University London. Each segment can be defined with non-overlapping elements, polynomial order, and quadratic order. In the physiological models, the arterial segments are mostly split into two-centimetre meshes. The time step, structure, and mechanical properties, such as dimensions, of each model will be mentioned separately in each chapter. Figure 2.6 summarizes the procedure of calculation of wave propagation using the equations mentioned in this chapter.

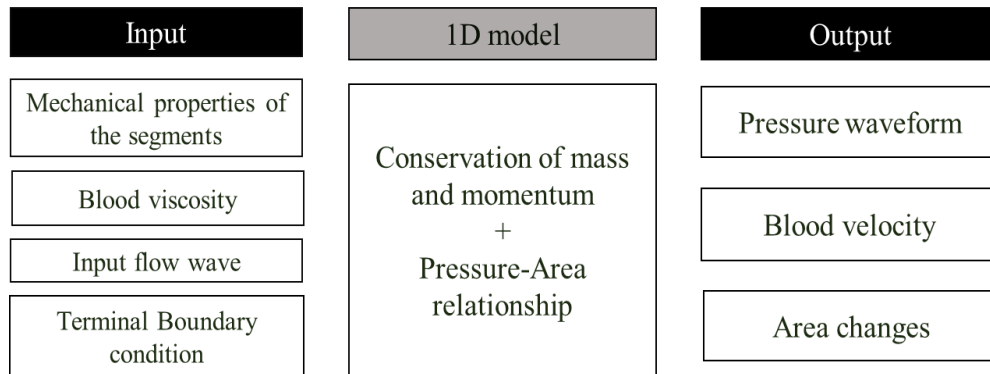


Figure 2. 6. A description of the procedure of calculation of wave propagation using the 1D model. The input variables are defined, and the numerical platform solves the equations of conservation of mass and momentum and tube law and produces the changes in pressure and velocity and area changes.

CHAPTER 3

IMPACT OF BIFURCATIONS ON PRESSURE AND WAVE REFLECTIONS

3.1 INTRODUCTION

Alteration in the morphology of the pressure wave was noted half a century ago, but the underlying mechanism responsible for these changes are not well understood. Many studies are focusing on the existence of reflected waves in the ascending aorta and their influence on the amplitude of pressure. Nevertheless, there is an ongoing debate about their origin, and the distance that a reflected wave can travel (LUCHSINGER *et al.*, 1964; O'Rourke *et al.*, 1968; Westerhof *et al.*, 2008; Davies *et al.*, 2012; Segers *et al.*, 2017).

The arterial tree is a multi-branching structure. As the parent vessel splits to its daughter vessels, there is a reflection arising from the junction. The reflection coefficient can be calculated by Equations (2.63 -2.65).

Even though there are many bifurcations in the arterial tree, the junctions in healthy arterial tree tend to follow a particular pattern. The bifurcations, mainly, are well-matched for the forward travelling waves, which means the backward waves are not easily transmitted to the reverse direction. Further, the structure of junctions shows a considerable amount of asymmetry in daughter branches (Papageorgiou *et al.*, 1990). The relationship between the dimension of the parent vessel and the daughter vessel dimensions are expressed as area ratio, presented by α , and can be calculated with

$$\alpha = \frac{A_{D1} + A_{D2}}{A_p}, \quad (3.1)$$

where A_{D1} and A_{D2} are the cross-sectional areas of the daughter vessels, and A_p is the cross-sectional area for the parent vessel.

Womersley and Karreman (Karreman, 1952) theoretically studied the case of symmetrical bifurcation and reported that if the area ratio is in a range of 1.14 degrees, the wave reflection will be minimal. In reference (Papageorgiou *et al.*, 1990), the authors studied 444 junctions at different locations of the human arterial system of the arterial tree, and they concluded that the optimal area ratio range predicted theoretically for wave reflections on being minimal are in agreement with their measurement, except the aortoiliac bifurcation where a lower value was

found. The aortoiliac bifurcation and its changes with age were studied in (Greenwald, Carter and Berry, 1990), where they noticed the reflection coefficient is changing from +0.3 in early life to -0.3 in old age. It is worth mentioning the assumption behind optimal area ratio for a minimal reflected wave is that the ratio of wall thickness to vessel radius stays constant before and after the junction.

There are different approaches to model bifurcations (Anliker, Rockwell and Ogden, 1971; Stettler, Niederer and Anliker, 1981; Mynard and Valen-Sendstad, 2015). In this chapter, the effect of bifurcation is studied computationally using the 1D model explained in Chapter 2. It is assumed that the bifurcation to take place at one point. Since there is no blood leaving the system at that point, the equilibrium is

$$q_p = q_{D1} + q_{D2}. \quad (3.2)$$

Considering that the pressure is continuous over the bifurcation,

$$P_p = P_{D1} = P_{D2}. \quad (3.3)$$

In reduced order (0D /1D) computational models of blood flow, also in this thesis, the energy loss at the bifurcations is neglected. However, in (Mynard and Valen-Sendstad, 2015), the authors studied the effect of energy losses in different angles and directions of the flow and concluded that considering energy loss can provide more accurate results.

In this chapter, several computational structures are simulated to unravel the impact of bifurcation on the reflected waves. The result of each simulation and structure are presented under the same subsection. Discussion about the results is provided in Section 3.4, followed by the conclusion in Section 3.5.

3.2 METHODOLOGY

Based on the 1D formulations and principles mentioned in Chapter 2, the propagation of waves in bifurcations are studied in this chapter. Different bifurcation models are used with different numbers of segments and complexities, and the pressure waveforms in those models are analysed. In all of the models, the parent vessel or the “mother” vessel is one of the measurement locations. This study starts with simple and easy-to-grasp models to facilitate understanding and validating the results of the simulations, and then the complexity increases to a maximum of 15 consecutive bifurcations.

A single bifurcation (Section 3.2.1) and then a two-consecutive bifurcation (Section 3.2.2) are simulated, and the calculated pressure waveforms in these models are analysed. These models

are simulated in two setups: 1) Inflow pulse is injected in the parent vessel. 2) The inflow pulse is inserted from one of the daughter vessels.

Next, more complicated setups with more than 11 vessels are compiled. The first simulation, which is five consecutive bifurcations, is explained in more detail in Section 3.2.3. Ten more bifurcations are added to the model in Section 3.2.4. In this section, the input is injected from terminal points in order to impose a big enough “reflected wave” which can be measured at the inlet. In the mentioned simulations. The shape of the flow impulse is defined as

$$q(t) = 5 \cdot 10^{-5} \exp(-10000(t - 0.05)^2) \text{ m}^3/\text{s}. \quad (3.4)$$

Any perturbation, such as semi-Gaussian shaped pulse, generates changes in pressure, area and velocity. The equations of conservation of mass and momentum and the tube-law (mentioned in chapter 2) calculate the changes in variables mentioned above.

3.2.1 PRESSURE WAVEFORMS IN A SIMPLE BIFURCATION

In this study, the movement of pressure waveforms in a simple bifurcation is traced when the inflow is prescribed to be, firstly, inserted into the parent vessel (I), and then the end of one of the daughter vessels to replicate a single ‘reflection’ coming from the end of a bifurcation (II).

I) FORWARD DIRECTION

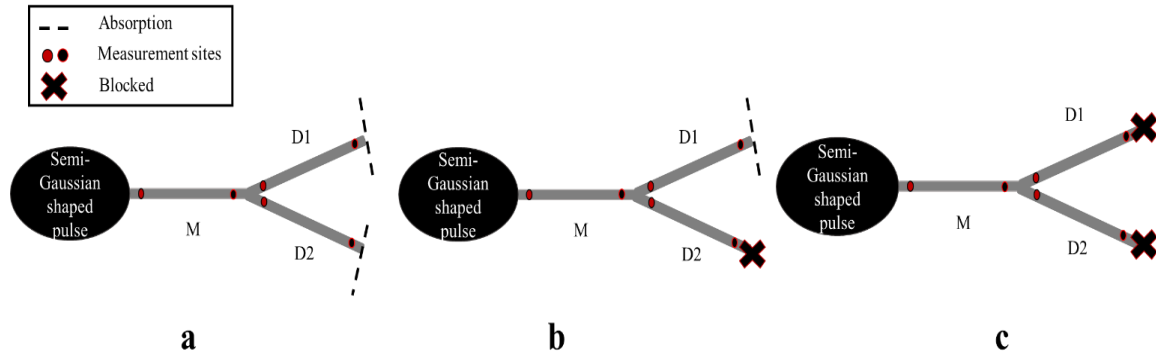
A semi Gaussian-shaped pulse is prescribed at the inlet of the parent vessel connected to a bifurcation. Table 3.1 presents the properties used for the vessels. The vessels are modelled to be 5-metres long, providing reflected waves with enough distance to occur separately with no overlaps, because a mean value for physiological wave speed in the aorta is 5 *m/s*. The pressure measurement locations are at the inlet and outlet of each vessel, as displayed in Figure 3.1. The parent vessel, or the mother vessel, is shown with M. D1 and D2 are the daughter vessels. The terminal boundary conditions for the daughter vessels are changed in 3 different simulations.

In Simulation a, terminal boundary condition for both daughter vessels is complete absorption. With this boundary condition, the reflected waves can be generated only by the bifurcation (Figure 3.1a). In Simulation b, one of the daughter vessels is blocked, causing a reflection travelling back from that terminal point (Figure 3.1b). Finally, both daughter vessels are blocked, and the number of reflections is expected to rise due to reflections caused by the blocked ends (Figure 3.1c).

Table 3. 1. The properties used in the simple symmetrical bifurcation model. The daughter vessels have the same properties, mentioned in 1st Bifurcation column.

Parameter	Description	Parent vessel	1st Bifurcation
r_0 (cm)	Initial radius	1.00	0.80
A_0 (cm ²)	Initial area	3.14	2.51
h (mm)	Thickness	0.50	0.50
E (MPa)	Young's modulus	1.20	1.20
L (m)	Length	5.00	5.00

Alterations in pressure in vessels are measured in two locations; at the beginning of the vessel ($x = 0.00$ metre, marked with red circles), and at the end of the vessel ($x = 4.99$ metres, marked with black circles).


 Figure 3. 1. The prescribed terminal boundary conditions for the daughter vessels, which is either absorption ($R=0$), or blocked ($R=1$)

The values calculated by the 1D model are compared with values calculated by the equations mentioned above to validate the results of simulations. The time of occurrence of waves and their reflections is estimated using the wave speed and the travelled distance, i.e. $t = \Delta L/c$. The PWV is calculated using the Moens-Korteweg equation (Eq. 1.3). The amplitude of each pressure wave is estimated using reflection coefficient (R_f) at bifurcations (Eq. 2.63-2.65) and transmission coefficient ($T = R_f + 1$) as below:

$$P_{reflected} = R_f * P_{incident}, \quad P_{transmitted} = T * P_{incident}. \quad (3.5)$$

When an incident pressure wave, $P_{incident}$, reaches the bifurcation, a part of the pressure is reflected and a wave, $P_{reflected}$, travels in the backward direction. The other part continues to travel in its initial direction which is known as $P_{transmitted}$.

In Equation 3.5 the expression $(1+R_f)$ is the transmission coefficient (shown by T - mentioned in chapter 2, Section 2.7). Since R_f can be either positive or negative, based on the dimensions of the bifurcation, T can be $T>1$ or $T<1$ causing the transmitted pressure to be either

larger or smaller than incident pressure. In a physiological environment, bifurcations can have positive and negative reflection coefficients.

II) BACKWARD DIRECTION

The same bifurcation with properties presented in Table 3.1 is simulated in this study. However, the inflow is introduced to the system from the daughter vessel 2. The inflow is mimicking a reflection arising from the terminal point of the daughter vessel. The boundary condition for the parent vessel is complete absorption. The inflow is defined as Equation 3.4.

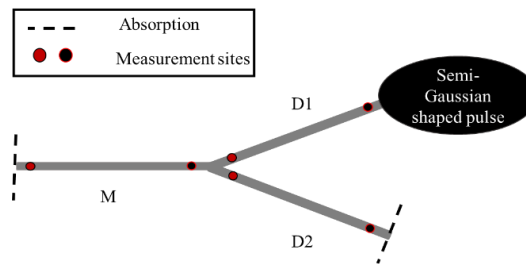


Figure 3. 2. A simple bifurcation with an inflow defined at the terminal boundary condition of daughter 1. Other boundaries are complete absorption ($R=0$)

Figure 3.2 depicts the measurement sites at the inlet ($x = 0.00$, shown with red circles) and outlet ($x = 4.99$, illustrated with black circles).

3.2.2 PRESSURE WAVEFORMS IN TWO-CONSECUTIVE BIFURCATIONS

In these simulations, the models are further complex, and an additional bifurcation is added to the model. The inflow is first described at the inlet of the parent vessel and then moved to the terminal point of a daughter vessel in the first generation of bifurcation, and then a daughter vessel of second-generation bifurcation. Figure 3.3 is a schematic presentation of two-consecutive bifurcations and the location of inflow in each simulation. The measurement site is the inlet of the segments. The complete absorption boundary condition is used for the rest of the terminal points.

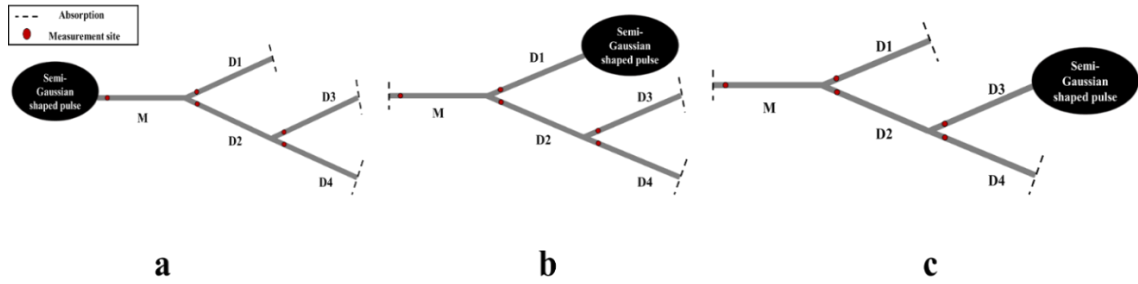


Figure 3.3. Two-consecutive bifurcations with different locations prescribed for inflow. Other than inflow, the boundary condition for distal ends are absorption ($R=0$).

The properties used for each vessel can be found in Table 3.2. It is worth mentioning that in this thesis, the bifurcation is the point that three-vessel are connected.

Table 3.2. The parameters used for modelling two-consecutive bifurcations.

Parameter	Description	Parent vessel	1st Bifurcation	2nd Bifurcation
r_0 (cm)	initial radius	0.86	0.60	0.35
A_0 (cm ²)	initial area	2.32	1.13	0.38
h (mm)	Thickness	1.29	1.26	1.05
E (kPa)	Young's modulus	400	400	400
L(m)	Length	5	5	5

The inflow shape is defined similarly to other models using Equation 3.3. In these simulations, other than explaining the behaviour of the reflected waves caused by bifurcations, the results of the simulations are validated by estimation of time and distance of the reflected waves.

3.2.3 PRESSURE WAVEFORMS IN A FIVE-CONSECUTIVE BIFURCATIONS

After explanation and validation of the waves and their reflections in the simple models, more complex structures are used to study the influence of bifurcations on pressure waveform travelling from the inlet of the parent vessel. The semi Gaussian-shaped inflow waveform is injected into the inlet of the parent vessel, followed by five generations of bifurcations, as demonstrated in Figure 3.4. The terminal boundary condition of one of the daughter vessels at 5th generation is blocked.

The changes in pressure measured at the inlet of the parent vessel to investigate whether the reflection originated from the blocked end reach to the inlet. The same model is simulated when there is no blockage at the 5th generation bifurcations, and the pressure at the inlet of this model is compared against the previous one.

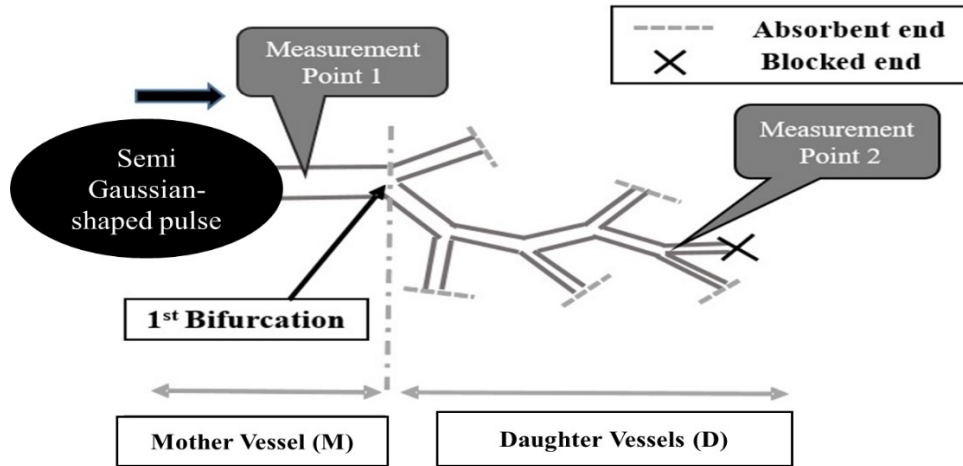


Figure 3. 4. Schematic presentation of the five consecutive bifurcations with one blocked terminal point in its fifth bifurcation.

The area ratio between each parent vessel and the daughter vessels is 1.15, which is in the range for well-matched bifurcation. Table 3.3 presents the values used for each segment.

Table 3. 3. The parameter used in five-consecutive bifurcations model.

Parameter	Description	Parent vessel	1st Bifurcation	2nd Bifurcation	3rd Bifurcation	4th Bifurcation	5th Bifurcation
r_0 (cm)	Initial radius	0.86	0.6	0.44	0.33	0.24	0.18
A_0 (cm ²)	Initial area	2.32	1.13	0.62	0.34	0.19	0.103
h (mm)	Thickness	1.29	1.26	1.05	1.02	1	0.98
E (kPa)	Young's modulus	400	400	400	400	400	400
c (m/s)	Wave speed	6.17	7.30	7.74	8.86	10.18	11.70

3.2.4 PRESSURE WAVEFORMS IN A 15-CONSECUTIVE BIFURCATION WITH INFLOW AT TERMINAL LOCATIONS

Finally, a structure of 15 consecutive bifurcations is simulated, as shown in Figure 3.5. The changes in pressure at the inlet of the parent vessel (M) are analysed in 15 different simulations. In each simulation, a semi Gaussian-shaped pulse is inserted at the terminal point of the daughter vessels, one at a time. The pressure calculated at the inlet of the parent vessel is compared with the amplitude of input pressure from the peripheral points. The boundary conditions of the other terminals are kept absorbent, to investigate the magnitude of the arrival waves from the specific terminal point to the parent vessel.

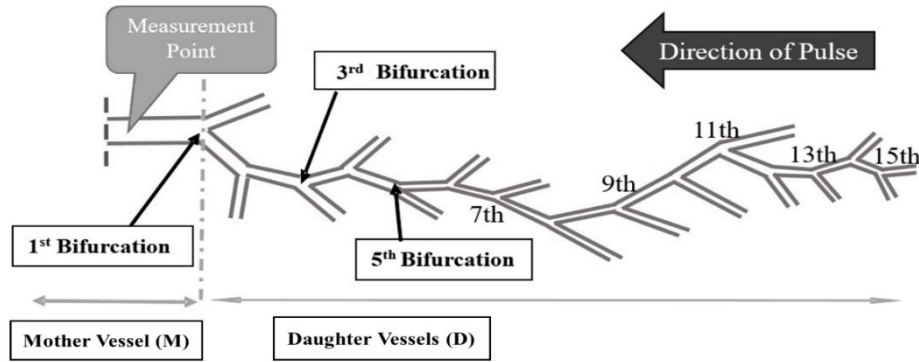


Figure 3. 5. A schematic presentation of 15-consecutive bifurcations. The inflow is injected at the end of daughter vessels in each generation of bifurcations one by one in 15 different simulations.

3.3. RESULTS

In this section, the results of the simulations are presented with a similar subgroup as the methodology. For example, the outcomes of the five-consecutive bifurcations (3.2.3) are in this section is under the subset of 3.3.3.

3.3.1 PRESSURE WAVEFORMS IN A SIMPLE BIFURCATION

1) FORWARD DIRECTION

The wave speed and reflection coefficient for each segment are calculated using Equations 1.2 and 2.63-2.65, respectively; the results are presented in Table 3.4.

Table 3. 4. The wave speed and reflection coefficient calculated for each vessel in a simple bifurcation model.

Segment	Vessel 1 (M)	Vessel 2 (D1)	Vessel 3 (D2)
Wave speed	6.17	6.52	6.52
Reflection coefficient	-0.2	-0.4	-0.4

With the values mentioned above and Equation 3.4, the timing and amplitude of the pressure waves at each vessel are estimated. The pressure measured at the inlet and outlet is illustrated with red and black lines, respectively. Figure 3.6 depicts the results of Simulation *a* in all vessels, with each wave having an alphabet letter as labels.

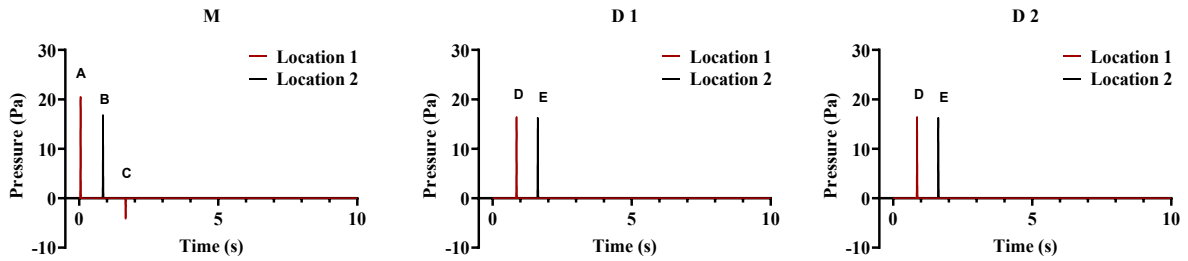


Figure 3. 6. The pressure variation in vessels of the bifurcation model. M is the mother/parent vessel, D1 is the first daughter vessel, and D2 is the second daughter vessel. The terminal boundary condition for both daughter vessels is absorption. (Simulation a) The pressure is estimated in two locations at each vessel; location 1 is close to its inlet and location 2 is at its outlet.

Table 3.5 consists of description each wave in the mother vessel, such as the path, the occurrence time, and amplitude of pressure in a bifurcation with absorbing boundary condition.

It is assumed that the positive direction is towards the right-hand side. If the wave is travelling in the forward direction, the route is shown with the vessel and its corresponding number, for example, V1 is moving in vessel 1 in the forward direction. While, if it is a reflected wave and travelling from right to left, the route has a negative sign behind it. For example, a reflection travelling vessel 1 is presented as $-V1$.

Table 3. 5. Pressure waves and their corresponding route, amplitude and time of occurrence in Simulation a. The values given by the simulations are compared against the values calculated by the theoretical equations.

Vessel 1 (M)			Time (s)		Amplitude (Pa)	
Wave	Location	Path	Simulation	Calculation	Simulation	Calculation
A	1	Input	0	0	20.62	-
B	2	V1	0.82	0.81	16.92	16.49
C	1	V1, -V1	1.64	1.62	-4.19	-4.12

The semi-Gaussian shaped inflow, defined with Equation 3.5, causes a pressure pulse with a peak value of $20.62 Pa$, labelled with letter A in Figure 3.6. This pressure wave travelled through the vessel and reached to location 2, which adjacent to the bifurcation. Hence, the peak pressure of wave B calculated by Equation 3.5 ($R_f = -0.2$) is $16.92 Pa$. The similar value was obtained from the simulations which computes the pulse propagation by solving the equations of conservation of mass and momentum and the tube-law.

As exhibited both in Figure 3.6 and Table 3.5 wave C is arising from the bifurcation, and since the reflection coefficient is negative and the initial pressure in the vessel is zero, the amplitude

of the pressure is negative, and an expansion wave travels back to the inlet. Using a single semi-Gaussian shaped inflow can show the influence of junctions on the wave in the arterial network models. Negative reflected pressure from a junction indicates that if a pressure wave with non-zero initial value reaches that junction, its amplitude is reduced. A similar approach to study the pattern of pulse waves is used in references (Wang and Parker, 2004; Alastruey *et al.*, 2009).

There are no existing reflections in daughter vessels since waveforms are entirely absorbed in their terminal ends.

The similar information about waves present in daughter vessels can be found in Table 3.6. Because of identical properties of daughter vessel, the waves are similar. Therefore, the descriptions are combined.

Table 3. 6. Information about the pressure waveforms present in the daughter vessels 1 and 2.

Vessel 2&3 (D1, D2)			Time (s)		Amplitude	
Wave	Location	Path	Simulation	Calculation	Simulation	Calculation
D	1	V1	0.82	0.81	16.39	16.49
E	2	V1,V2	1.59	1.57	16.35	16.49

The absorbing boundary conditions at daughter vessels cause minimum reflections. However, with blocking one of the daughter vessels in Simulation *b*, as shown in Figure 3.7, the reflections are three times more than Simulation *a*. The waves occurring at the same time but different amplitudes in vessels have the same alphabetic letter, but different numbers. For example, waves F, F1, and F2 are measured at 3.24 seconds in the mother vessel, daughter vessel 1 and daughter vessel 2, respectively.

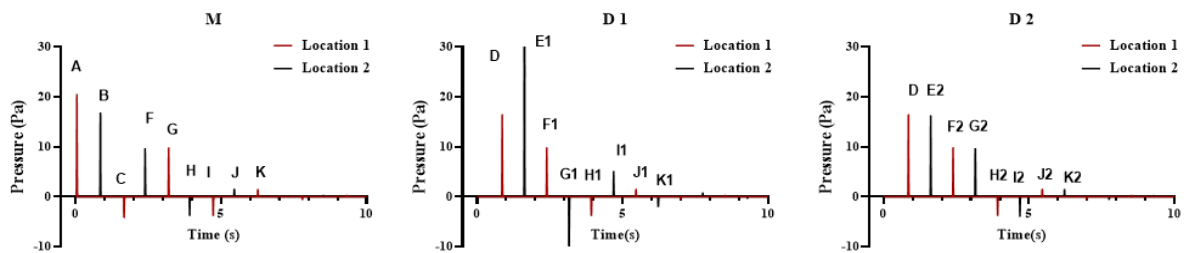


Figure 3. 7. Pressure waveforms in all vessels in a bifurcation. The terminal boundary condition for daughter vessel 1 is blocked while daughter vessel 2 has an absorbing boundary condition. (Simulation *b*) location 1 is close to its inlet and location 2 is at its outlet.

Information about each wave in the mother vessel in Simulation *b* is presented in Table 3.7.

3.3. Results

Table 3. 7. Pressure waves and their corresponding route, amplitude and time of occurrence in mother vessel (V1). The values given by the simulations are compared against the values calculated by the theoretical equations. (Simulation b)

Vessel 1 (M)			Time (s)		Amplitude (Pa)	
Wave	Location	Path	Simulation	Calculation	Simulation	Calculation
A	1	Input	0	0	20.62	20.62
B	2	V1	0.82	0.81	16.92	16.49
C	1	V1, -V1	1.64	1.62	-4.19	-4.12
F	2	V1, V2,-V2	2.39	2.34	9.8	9.89
G	1	V1,V2,-V2,-V1	3.17	3.15	9.75	9.89
H	2	V1, V2,-V2,V2,-V2	3.87	3.87	-3.89	-3.95
I	1	V1, V2,-V2,V2,-V2, -V1	4.69	4.68	-3.86	-3.95
J	2	V1, V2,-V2,V2, -V2,V2,-V2	5.43	5.41	1.53	1.58
K	1	V1, V2,-V2,V2,-V2,V2,-V2,V1	6.23	6.22	1.52	1.58

In Simulation *b*, the first three waveforms at the mother vessel are similar to the previous one. But, due to the blocked end at the daughter vessel 1, more reflections are returning towards the mother vessel. At the bifurcation the reflected waveform is partially transferred into the daughter vessel 2, also re-reflecting back to the endpoint. This re-reflection is again reflected, reaching the bifurcation and generating another reflection in both mother vessel and daughter vessel 2. These phenomena continue until the amplitude of the pressure waveform reaches to zero.

Table 3. 8. Pressure waveforms amplitude and time, and their routes in daughter 1. (Simulation b)

Vessel 2 (D1)			Time (s)		Amplitude (Pa)	
Wave	Location	Path	Simulation	Calculation	Simulation	Calculation
D	1	V1	0.82	0.81	16.39	16.49
E1	2	V1,V2	1.59	1.57	31.96	32.91
F1	1	V1, V2,-V2	2.36	2.34	9.8	9.89
G1	2	V1, V2,-V2,V2	3.12	3.11	-12.64	-13.14
H1	1	V1, V2,-V2,V2,-V2	3.89	3.87	-3.87	-3.95
I1	2	V1, V2,-V2,V2,-V2, V2	4.66	4.64	5	5.27
J1	1	V1, V2,-V2,V2,-V2,V2,-V2	5.42	5.41	1.53	1.58
K1	2	V1, V2,-V2,V2,-V2,V2,-V2,V2	6.2	6.18	-1.97	-2.11

Table 3.8 and 3.9 present the route of each wave and their calculated time of arrival and amplitude for daughter vessel 1 and 2.

Table 3. 9. Pressure waveforms amplitude and time, and their routes in daughter 2 with an absorbing end. (Simulation b)

Vessel 3 (D2)			Time (s)		Amplitude (Pa)	
Wave	Location	Path	Simulation	Calculation	Simulation	Calculation
D	1	V1	0.82	0.81	16.39	16.50
E2	2	V1, V2	1.59	1.5728	16.35	16.50
F2	1	V1, V2, -V2	2.362	2.34412	9.8	9.89
G2	2	V1, V2, -V2, V3	3.128	3.11	9.76	9.89
H2	1	V1, V2, -V2, V2, -V2	3.88	3.87	-3.89	-3.95
I2	2	V1, V2, -V2, V2, -V2, V3	4.66	4.64	-3.86	-3.95
J2	1	V1, V2, -V2, V2, -V2, V2, -V2	5.42	5.41	1.53	1.58
K2	2	V1, V2, -V2, V2, -V2, V2, -V2, V3	6.18	6.18	1.53	1.58

Finally, in Simulation *c*, where both daughter vessels are blocked, the same pattern in the first one second of the simulation is apparent. The occurrence time of the second reflected wave is similar to the previous simulation. (Figure 3.8) Though, the amplitude is double as it is an amalgamation of the two reflected waves caused by both daughter vessels. Table 3.10 is the description of waves in the mother vessel.

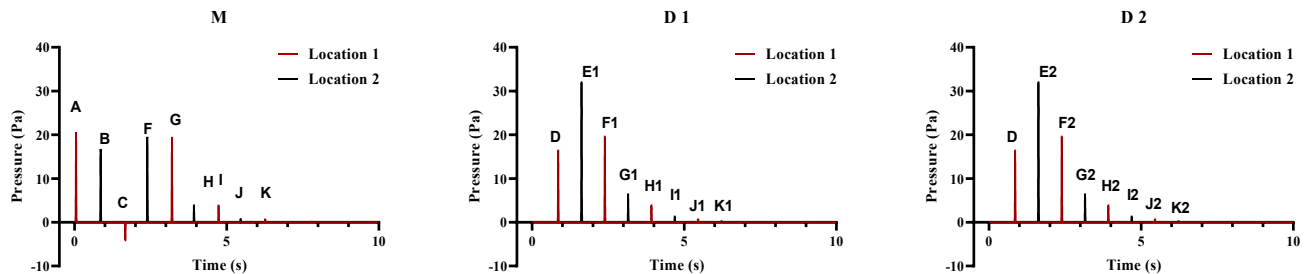


Figure 3. 8. Pressure waveforms in all vessels in a bifurcation. The terminal boundary conditions for both daughter vessels are blocked. (Simulation c)

Waves F to K are an amalgamation of two reflections coming from daughter vessels 1 and 2. Therefore the routes for the mentioned waves are written in parenthesis with two vessels.

The reflections in the daughter vessels are identical; therefore, only the waves in one of them are traced. Table 3.11 present the routes, amplitude and the time of arrival of different wave calculated using theoretical formulas and the results of simulations.

3.3. Results

Table 3. 10. Pressure waves and their corresponding route, amplitude and time of occurrence in mother vessel (V1). The values given by the simulations are compared against the values calculated by the theoretical equations. (Simulation c)

Vessel 1 (M)			Time (s)		Amplitude (Pa)	
Wave	Location	Path	Simulation	Calculation	Simulation	Calculation
A	1	Input	0	0	20.62	20.62
B	2	V1	0.82	0.81	16.92	16.49
C	1	V1, -V1	1.64	1.62	-4.19	-4.12
F	2	V1, (V2&V3), (-V2&-V3)	2.392	2.34412	19.65	19.78
G	1	V1, (V2&V3), (-V2&-V3), -V1	3.17	3.1545	19.51	19.78
H	2	V1, (V2&V3), (-V2&-V3), (V2&V3), (-V2&-V3)	3.87	3.87	3.97	3.31
I	1	V1, (V2&V3), (-V2&-V3), (V2&V3), (-V2&-V3), -V1	4.69	4.68	3.95	3.31
J	2	V1, (V2&V3), (-V2&-V3), (V2&V3), (-V2&-V3), (V2&V3), (-V2&-V3)	5.43	5.41	0.8	0.79
K	1	V1, (V2&V3), (-V2&-V3), (V2&V3), (-V2&-V3), (V2&V3), (-V2&-V3), V1	6.23	6.22	0.8	0.79

The highlighted waves are an amalgamation of two waves: 1) reflection caused by the bifurcation, 2) transmitted pressure from daughter vessel 2. Similar values are obtained for the second daughter vessel, as appeared in Figure 3.8.

Table 3. 11. Pressure waveforms amplitude and time, and their routes in daughter 1 and 2 with blocked ends. (Simulation c)

Vessel 2 (D1)			Time (s)		Amplitude	
Wave	Location	Path	Simulation	Calculation	Simulation	Calculation
D	1	V1	0.82	0.81	16.39	16.49
E1	2	V1, V2	1.59	1.57	31.96	32.91
F1	1	V1, V2, -V2	2.36	2.34	19.61	19.78
G1	2	V1, V2, -V2, V2	3.12	3.11	6.48	6.59
H1	1	V1, V2, -V2, V2, -V2	3.89	3.87	3.97	3.31
I1	2	V1, V2, -V2, V2, -V2, V2	4.66	4.64	1.31	1.31
J1	1	V1, V2, -V2, V2, -V2, V2, -V2	5.42	5.41	0.805	0.79
K1	2	V1, V2, -V2, V2, -V2, V2, -V2, V2	6.20	6.18	0.26	0.24

II) BACKWARD DIRECTION

In this bifurcation model, a narrow pulse is inserted from the terminal point of the first daughter vessel. Therefore, the first wave is occurring at the end of D1. As the waveform proceeds to bifurcation point, a reflection is generated in all vessels. The reflection can be seen at 0.78

seconds in the D2 vessel shown in Figure 3.9. Since the terminal boundary conditions are absorption, no reflections are originating from vessel 1 and vessel 3.

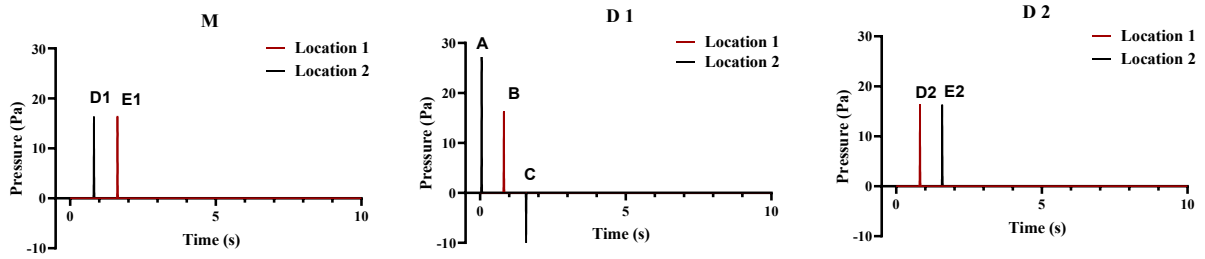


Figure 3. 9. The pressure variation in vessels of the bifurcation model. M is the mother vessel, D1 is the first daughter vessel, and D2 is the second daughter vessel. The inflow introduced to the system from the end of daughter 1 and terminal boundary conditions for other vessels are absorption.

The waves and their path in vessels are presented in three tables. Table 3.12 shows waves in the parent or mother vessel. Since the stream is entering the vessel from the right-hand side, the wave arrives first in location 2, $x = 4.99$ metres, and then reaches the site 1, $x = 0.00$. The simulated results demonstrate a good agreement with values calculated by the before-mentioned equations.

Table 3. 12. Pressure waves and their corresponding route, amplitude and time of occurrence in mother vessel (V1). The inflow is inserted from the daughter vessel to replicate a reflection. (Reverse direction)

Vessel 1 (M)			Time (s)		Amplitude (Pa)	
Wave	Location	Path	Simulation	Calculation	Simulation	Calculation
D1	2	-V2	0.78	0.76	16.39	16.35
E1	1	-V2, -V1	1.59	1.57	16.34	16.35

Table 3.13 shows the waves in daughter vessel 1 (D1), wherein pulse is prescribed at its outlet, $x = 5$ metres. Wave B is the transmitted wave at the bifurcation point, and wave C is the reflection caused by bifurcation.

Table 3. 13. Pressure waves and their corresponding route, amplitude and time of occurrence in Daughter1, where the inflow is injected. (Reverse direction)

Vessel 2 (D1, Input)			Time (s)		Amplitude (Pa)	
Wave	Location	Path	Simulation	Calculation	Simulation	Calculation
A	2	Input	0	0	27.25	27.25
B	1	-V2	0.78	0.76	16.38	16.35
C	2	-V2, V2	1.55	1.53	-10.82	-10.9

Finally, Table 3.14 indicates the waves in daughter vessel 2 (D2). The waves are similar to waves presented in vessel 1, with a small difference in time of arrival because of different values of wave speed.

Table 3. 14. Pressure waves and their corresponding route, amplitude and time of occurrence in Daughter2. The inflow is injected into daughter vessel 1. (Reverse direction)

Vessel 3 (D2)			Time (s)		Amplitude	
Wave	Location	Path	Simulation	Calculation	Simulation	Calculation
D2	1	-V2	0.78	0.76	16.39	16.35
E2	2	-V2, V3	1.55	1.53	16.34	16.35

3.3.2 PRESSURE WAVEFORMS IN TWO-CONSECUTIVE BIFURCATIONS

After validation and tracing the waves in a simple bifurcation, both in forward and backward directions, a two-consecutive bifurcation is studied. Same as previous simulations, the amplitude, and time of arrival of pressure waves are estimated in two sites using Equations 2.63-2.65 and compared with the values that are given by the simulations. Table 3.15 provides the values of wave speed and reflection coefficient in the vessels.

Table 3. 15. Wave speed and reflection coefficient calculated for vessels in two-consecutive bifurcations' model

Segment	Vessel 1	Vessel 2	Vessel 3	Vessel 4	Vessel 5
Wave speed	6.17	7.3	7.3	8.73	8.73
Reflection coefficient	0.097	-0.55	0.27	-0.64	-0.64

Pressure variations in time are measured in all vessel at their inlet and outlet, and each wave is labelled with a letter. For naming the waves, the vessel with input is the reference, and the labelling in that vessel starts from A. If any of the waves in other vessel have the same time of occurrence they will have the same alphabetic letter with their number next to it. Figure 3.10 shows the pressure waveforms in all vessels in Simulation *a*, in which the inflow is injected from the inlet of vessel 1; therefore, the labels start with letters A, B, etc. Since in vessels 2 and 3 waves are occurring at the same time as wave B, the labels for those waves are B2 and B3.

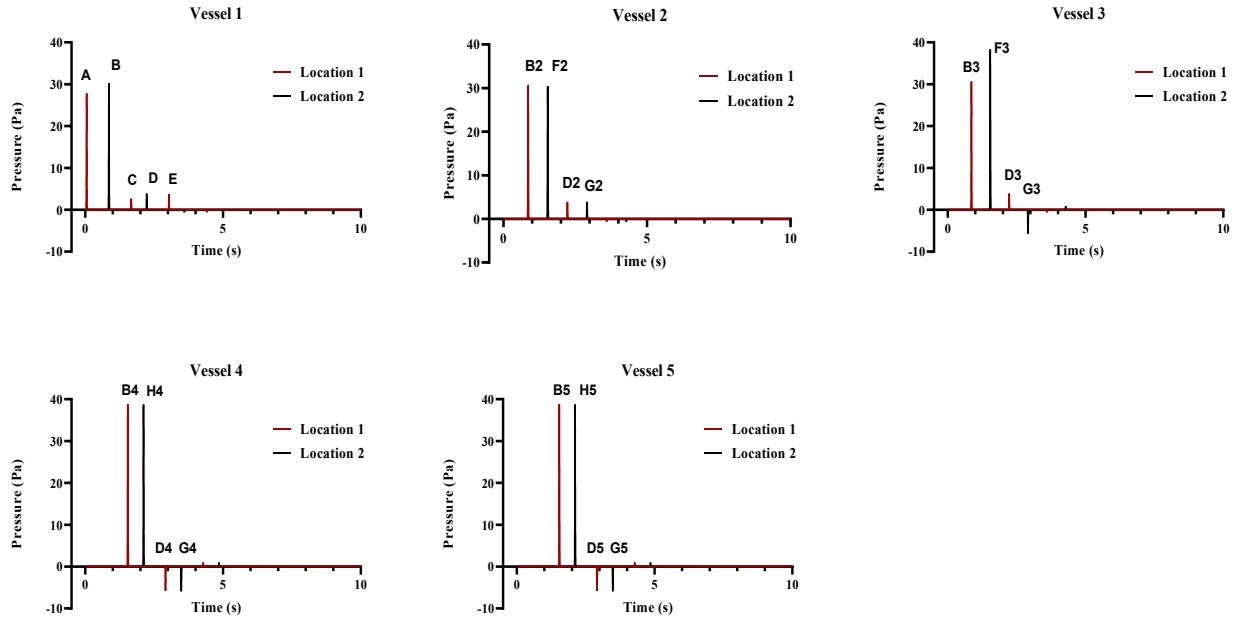


Figure 3. 10. The pressure variation in vessels of the two-consecutive bifurcation model. The inflow is introduced to the system from the inlet of vessel 1, and terminal boundary conditions for the rest of vessels are complete absorption. (Simulation a)

As the pressure wave travels through the first bifurcation, a reflection travels back (wave c). The transient pressure wave encounters the second bifurcation, and another reflection is generated in vessel 3 (wave F3). This reflection is trapped between the two bifurcations and partially being reduced after each reflection. Table 3.16 reports pressure waves in vessel 1.

Table 3. 16. Pressure waves and their corresponding route, amplitude and time of occurrence in vessel 1 in the two-consecutive bifurcations model. The inflow is injected into vessel 1. (Simulation a)

Vessel 1 (M, Input)			Time (s)		Amplitude (Pa)	
Wave	Location	Path	Simulation	Calculation	Simulation	Calculation
A	1	Input	0	0	27.87	27.87
B	2	V1	0.825	0.81	30.38	30.57
C	1	V1, -V1	1.642	1.62	2.7	2.71
D	2	V1, V3, -V3	2.2	2.18	3.76	3.78
E	1	V1, V3, -V3, -V1	3.01	2.98	3.742	3.78

The same reflections caused by the second bifurcation is evident in vessel 2, namely wave D2 and G2 in Table 3.17, although it is not connected to the second bifurcation and its boundary condition is absorption.

3.3. Results

Table 3. 17. Pressure waves and their corresponding route, amplitude and time of occurrence in vessel 1 in the two-consecutive bifurcations model. The inflow is injected into vessel 2. (Simulation a)

Vessel 2			Time (s)		Amplitude (Pa)	
Wave	Location	Path	Simulation	Calculation	Simulation	Calculation
B2	1	V1	0.828	0.81	30.53	30.57
F2	2	V1, V2	1.51	1.49	30.44	30.57
D2	1	V1, V3, -V3	2.2	2.17	3.75	3.78
G2	2	V1, V3, -V3, V2	2.87	2.86	3.74	3.78

The reflection caused by second bifurcation (wave F3) and re-reflections caused by the first bifurcation (wave D3) are evident in vessel 3, as shown in Table 3.18.

Table 3. 18. Pressure waves and their corresponding route, amplitude and time of occurrence in vessel 1 in the two-consecutive bifurcations model. The inflow is injected into vessel 3. (Simulation a)

Vessel 3			Time (s)		Amplitude (Pa)	
Wave	Location	Path	Simulation	Calculation	Simulation	Calculation
B3	1	V1	0.82	0.81	30.53	30.57
F3	2	V1, V3	1.51	1.49	38.33	38.82
D3	1	V1, V3, -V3	2.2	2.17	3.75	3.78
G3	2	V1, V3, -V3, V3	2.87	2.86	-5.73	-5.75

Tables 3.19 and 3.20 demonstrate the waves in vessel 4 and 5 in Experiment a. The pressure waveforms in these vessels are identical, with the same amplitude and arrival time.

Table 3. 19. Pressure waves and their corresponding route, amplitude and time of occurrence in vessel 1 in the two-consecutive bifurcations model. The inflow is injected into vessel 4. (Simulation a)

Vessel 4			Time (s)		Amplitude (Pa)	
Wave	Location	Path	Simulation	Calculation	Simulation	Calculation
B4	1	V1, V3	1.51	1.49	38.78	38.9
H4	2	V1, V3, V4	2.08	2.07	38.67	38.9
D4	1	V1, V3, -V3, V3	2.88	2.86	-5.8	-5.85
J4	2	V1, V3, -V3, V3, V4	3.46	3.44	-5.78	-5.55

Table 3. 20. Pressure waves and their corresponding route, amplitude and time of occurrence in vessel 1 in the two-consecutive bifurcations model. The inflow is injected into vessel 5. (Simulation a)

Vessel 5			Time (s)		Amplitude (Pa)	
Wave	Location	Path	Simulation	Calculation	Simulation	Calculation
B5	1	V1, V3	1.51	1.49	38.78	38.9
H5	2	V1, V3, V5	2.08	2.07	38.67	38.9
D5	1	V1, V3, -V3, V3	2.88	2.86	-5.8	-5.85
J5	2	V1, V3, -V3, V3, V5	3.46	3.44	-5.78	-5.55

In Simulation *b*, the impulse is inserted at the end of vessel 2, therefore the reference vessel is vessel 2, and as shown in Figure 3.11, the labels for waves in vessel 2 are A, B.

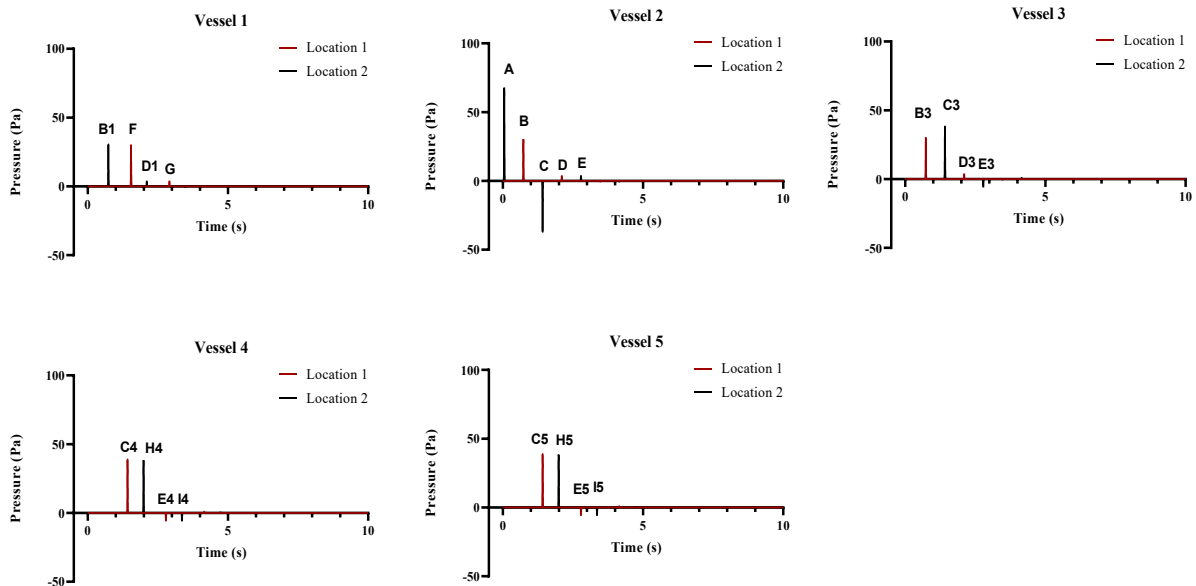


Figure 3. 11. The pressure variation in vessels of the two-consecutive bifurcation model. The inflow is introduced to the system from the outlet of vessel 2 to replicate a reflection wave behaviour, and terminal boundary conditions for the rest of the vessels are complete absorption. (Simulation b)

Since the input is coming from the left-hand side of the model, the initial wave in vessels 1 and 2 first appear at location 2; in other vessels, the first wave is a forward travelling wave. Table 3.21 presents the labels for the waves in vessel 1 and their paths and amplitude.

3.3. Results

Table 3. 21. Pressure waves and their corresponding route, amplitude and time of occurrence in vessel 1 in the two-consecutive bifurcations model. The inflow is injected into vessel 2 to replicate a reflection wave. (Simulation b)

Vessel 1 (M)			Time (s)		Amplitude (Pa)	
Wave	Location	Path	Simulation	Calculation	Simulation	Calculation
B1	2	-V2	0.7	0.68	30.53	30.47
F	1	-V2, -V1	1.51	1.49	30.37	30.47
D1	2	-V2, V3, -V3	2.08	2.05	3.75	3.7
G	1	-V2, V3, -V3, -V1	2.88	2.86	3.73	3.7

The inflow is injected from the end of vessel 2. Therefore, the timing of the waves present in vessel 2 is the reference for labelling waves in other vessels (Table 3.22). At the first bifurcation connecting vessel 1 to 2 and 3, wave B is transferred in vessel 1 as a reflection wave and in vessel 3 as an incident wave shown with B1 and B3, respectively.

Table 3. 22. Pressure waves and their corresponding route, amplitude and time of occurrence in vessel 2 in the two-consecutive bifurcations model. The inflow is injected into vessel 2 to replicate a reflection wave. (Simulation b)

Vessel 2 (Input)			Time (s)		Amplitude (Pa)	
Wave	Location	Path	Simulation	Calculation	Simulation	Calculation
A	2	Input	0	0	67.72	67.72
B	1	-V2	0.7	0.68	30.45	30.47
C	2	-V2, V2	1.38	1.39	-37.06	-37.15
D	1	V1, V3, -V3	2.08	2.05	3.75	3.7
E	2	-V2, V3, -V3, V2	2.76	2.73	3.73	3.7

The second bifurcation is where vessel 3 is connected to vessel 4 and 5, meaning that vessel 3 is the connecting vessel between two bifurcations. As displayed in Table 3.23, the reflection originating from two bifurcations are trapped in the vessel 3, and at each bifurcation, they lose part of their amplitude.

Table 3. 23. Pressure waves and their corresponding route, amplitude and time of occurrence in vessel 3 in the two-consecutive bifurcations model. (Simulation b)

Vessel 3			Time (s)		Amplitude (Pa)	
Wave	Location	Path	Simulation	Calculation	Simulation	Calculation
B3	1	0	0.7	0.68	30.52	30.47
C3	2	-V2, V3	1.38	1.39	38.27	38.7
D3	1	-V2, V3, -V3	2.07	2.05	3.75	3.7
E3	2	-V2, V3, -V3, V3	2.72	2.73	-5.72	-5.75

Part of the re-reflections is transferred into vessel 4 and 5 without any reflection waves travelling back since the waves are absorbed in their terminal boundary.

Table 3. 24. Pressure waves and their corresponding route, amplitude and time of occurrence in vessel 4 in the two-consecutive bifurcations model. The inflow is injected into vessel 2 to replicate a reflection wave. (Simulation b)

Vessel 4			Time (s)		Amplitude (Pa)	
Wave	Location	Path	Simulation	Calculation	Simulation	Calculation
C4	1	-V2, V3	1.38	1.39	38.76	38.7
H4	2	-V2, V3, V4	1.96	1.94	38.59	38.95
E4	1	-V2, V3, -V3, V3	2.75	2.73	-5.78	-5.75
I4	2	-V2, V3, -V3, V3, V4	3.33	3.31	-5.76	-5.86

Due to similar mechanical properties and length, the waves in vessels 4 and 5 are identical, as shown in Tables 3.24 and 3.25.

Table 3. 25. Pressure waves and their corresponding route, amplitude and time of occurrence in vessel 5 in the two-consecutive bifurcations model. The inflow is injected into vessel 2 to replicate a reflection wave. (Simulation b)

Vessel 5			Time (s)		Amplitude (Pa)	
Wave	Location	Path	Simulation	Calculation	Simulation	Calculation
C5	1	-V2, V3	1.38	1.39	38.76	38.7
H5	2	-V2, V3, V5	1.96	1.94	38.59	38.95
E5	1	-V2, V3, -V3, V5	2.75	2.73	-5.78	-5.75
I5	2	-V2, V3, -V3, V3, V5	3.33	3.31	-5.76	-5.86

Moving on to the Experiment *c*, where the inflow is introduced at the outlet of vessel 4, the ratio between the reflected wave reaching to vessel 1 and the flow wave reduces three times. Figure 3.12 depicts the pressure waveforms in all the vessels of Experiment *c*. Waveforms present in vessel 4 are the reference for waveforms in other vessels.

3.3. Results

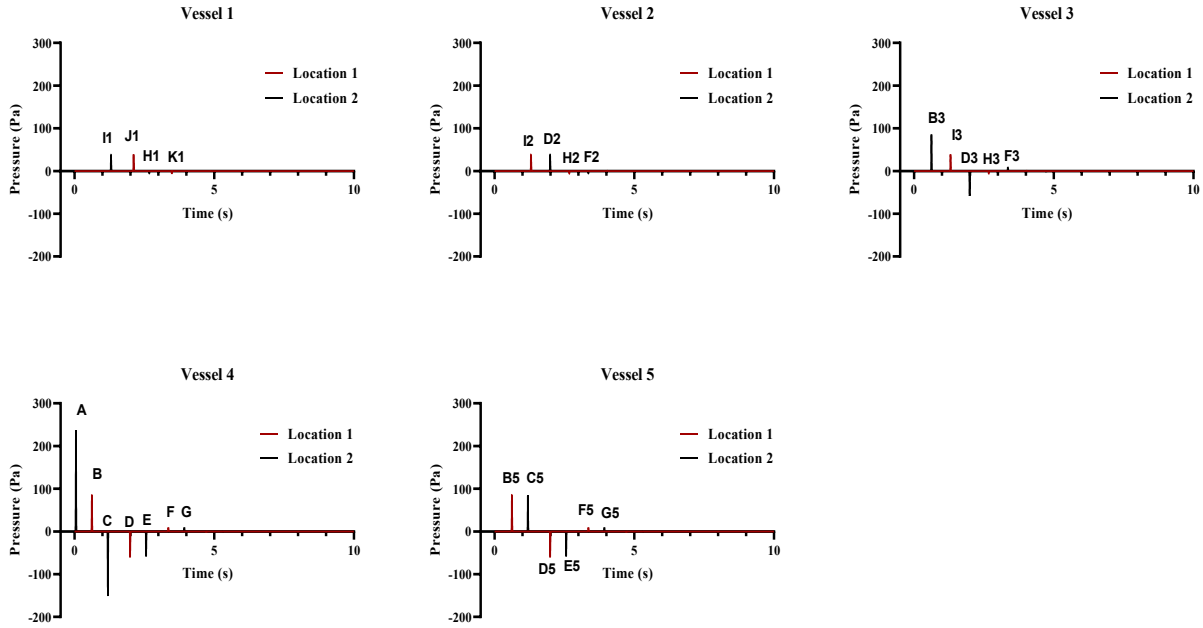


Figure 3. 12. The pressure variation in vessels of the two-consecutive bifurcations model. The inflow is introduced to the system from the outlet of vessel 4, and terminal boundary conditions for the rest of vessels are complete absorption. (Simulation c)

In Experiment *b*, the ratio of the reflection reaching the inlet of vessel 1 is 0.45, whereas, in Experiment *c*, the proportion reduces to 0.16. The amplitude of the waveforms in vessel 1 is reported in Table 3.26.

Table 3. 26. Pressure waves and their corresponding route, amplitude and time of occurrence in vessel 1 in the two-consecutive bifurcations model. The inflow is injected into vessel 4 to replicated distal reflections. (Simulation c)

Vessel 1			Time (s)		Amplitude (Pa)	
Wave	Location	Path	Simulation	Calculation	Simulation	Calculation
I1	2	-V4, -V3	1.28	1.26	38.56	38.62
J1	1	-V4, -V3, -V1	2.08	2.07	38.23	38.62
H1	2	-V4, -V3, V3, -V3	2.65	2.62	-5.74	-5.85
K1	1	-V4, -V3, V3, -V3, -V1	3.45	3.44	-5.71	-5.85

In this simulation, vessel 3 is the mutual vessel amongst two bifurcations; therefore, the same as previous simulations, the wave trapping phenomenon in vessel 3 can be observed in other vessels. Table 3.27 indicates the reflections reaching to vessel 2 as a forward travelling wave. Most reflections reaching vessel 2 are re-reflection of waves trapped between two bifurcations, and no reflections are originating for terminal points.

Table 3. 27. Pressure waves and their corresponding route, amplitude and time of occurrence in vessel 2 in the two-consecutive bifurcations model. The inflow is injected into vessel 4 to replicate a distal reflection. (Simulation c)

Vessel 2			Time (s)		Amplitude (Pa)	
Wave	Location	Path	Simulation	Calculation	Simulation	Calculation
I2	1	-V4, -V3	1.28	1.26	38.47	38.62
D2	2	-V4, -V3, -V2	1.96	1.94	38.23	38.62
H2	1	-V4, -V3, V3, -V3	2.64	2.62	-5.73	-5.85
F2	2	-V4, -V3, V3, -V3, -V2	3.33	3.31	-5.71	-5.85

Waveforms in vessel 3 are shown in Table 3.28. It is worth mentioning that the reflection coefficient for waves approaching vessel 3 alternates based on their direction. For example, wave approaching vessel 3 from vessel 1 and 2 are reflected by 27 per cent, while waves approaching vessel 3 are reflection by -55 %.

The amplitude of input increases with the reduction of the diameter of the vessel. The inflow for all simulations is the same waveform defined as Equation 3.4. The value for the inflow and the generated reflections in vessel 4 is reported in Table 3.29.

Table 3. 28. Pressure waves and their corresponding route, amplitude and time of occurrence in vessel 3 in the two-consecutive bifurcations model. The inflow is injected into vessel 4 to replicate a distal reflection. (Simulation c)

Vessel 3			Time (s)		Amplitude (Pa)	
Wave	Location	Path	Simulation	Calculation	Simulation	Calculation
B3	2	-V4	0.58	0.57	86.05	85.59
I3	1	-V4, -V3	1.27	1.26	38.42	38.47
D3	2	-V4, -V3, V3	1.96	1.94	-58.69	-60.12
H3	1	-V4, -V3, V3, -V3	2.65	2.62	-5.74	-5.71
F3	2	-V4, -V3, V3, -V3, V3	3.33	3.31	8.74	8.86

Finally, waveforms in vessel 5 are presented in Table 3.30. All waves are forward-travelling, and no reflections are generated in the vessel 5.

3.3. Results

Table 3. 29. Pressure waves and their corresponding route, amplitude and time of occurrence in vessel 4 in the two-consecutive bifurcations model. The inflow is injected into vessel 4 to replicate a distal reflection. (Simulation c)

Vessel 4 (Input)			Time (s)		Amplitude (Pa)	
Wave	Location	Path	Simulation	Calculation	Simulation	Calculation
A	2	Input	0	0	237.5	237.5
B	1	-V4	0.59	0.57	85.18	85.5
C	2	-V4, V4	1.15	1.14	-151.1	-152
D	1	-V4, -V3, V3	1.96	1.94	-59.39	-59.72
E	2	-V4, -V3, V3, V4	2.53	2.51	-59.15	-59.72
F	1	-V4, -V3, V3, -V3, V3	3.33	3.31	8.84	8.86
G	2	-V4, -V3, V3, -V3, V3, V4	3.9	3.88	8.81	8.86

Table 3. 30. Pressure waves and their corresponding route, amplitude and time of occurrence in vessel 5 in the two-consecutive bifurcations model. The inflow is injected into vessel 4 to replicate a distal reflection. (Simulation c)

Vessel 5			Time (s)		Amplitude (Pa)	
Wave	Location	Path	Simulation	Calculation	Simulation	Calculation
B5	1	-V4	0.58	0.57	86.06	85.5
C5	2	-V4, V5	1.16	1.14	85.56	85.5
D5	1	-V4, -V3, V3	1.96	1.94	-59.39	-59.72
E5	2	-V4, -V3, V3, V5	2.53	2.51	-59.15	-60.24
F5	1	-V4, -V3, V3, -V3, V3	3.33	3.31	8.84	8.86
G5	2	-V4, -V3, V3, -V3, V3, V5	3.9	3.88	8.81	8.86

The theoretical calculations are in agreement with the values given by the 1D model, both for the time of occurrence and amplitude of the waves.

3.3.3 PRESSURE WAVEFORMS IN FIVE-CONSECUTIVE BIFURCATIONS

Pressure and velocity are calculated at the inlet of five-consecutive bifurcations. The boundary conditions for all terminal vessels are, firstly, complete absorption, and then in the second simulation, one of the daughter vessels in the fifth bifurcation is blocked. Figure 3.13 (top) depicts the pressure and velocity at the inlet of the parent vessel where all the terminal points are absorbing. The results of the simulation where one of the daughter vessels of fifth-generation is blocked are shown in Figure 3.13 (bottom).

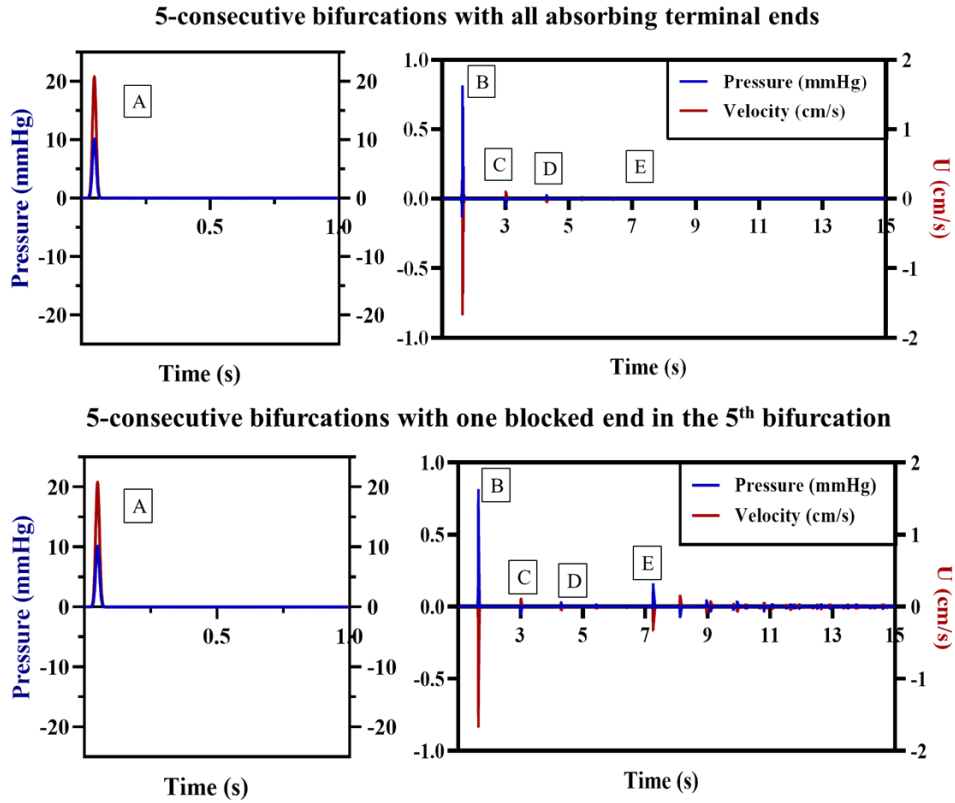


Figure 3. 13. Pressure and velocity variations in the stem vessel of the 5-consecutive bifurcations with all-absorbing terminal boundary conditions (top) and one blocked end in the fifth bifurcation (bottom). Each label in the figures corresponds to a wave. The left-hand picture is the input wave, and the right-hand side is a magnified view of the rest of pressures and velocities.

Same as previous studies, the waves are labelled, and the amplitude and time of occurrence are calculated and presented in Table 3.31. The difference in the results of two simulations in wave E, which is a result of reflection caused by the blocked end.

The reflection originating from the blocked terminal end in the 5th bifurcation arrived at the inlet of the mother vessel at 7.98 seconds. At 7.98 seconds, the existing amplitude of pressure is negligible compared to the input and overlapped with other artefacts whose source cannot be identified.

Table 3. 31. Pressure waves and their corresponding route, amplitude and time of occurrence in vessel 1 in the two-consecutive bifurcations model. The inflow is injected into vessel 2. (Simulation c)

Vessel 1 (Mother vessel)			
Wave	Path	Time (s)	Pressure (mmHg)
A	Input	0	10.14
B	V1, -V1	1.67	0.8156
C	V1, V2, -V2, -V1	3.02	-0.06
D	V1, V2, V3, -V3, -V2, -V1	4.18	0.03
E	V1, V2, V3, V4, V5, -V5, -V4, -V3, -V2, -V1	7.25	0.1548

There are many more reflection or re-reflection waves present in the pressure waveforms, however, due to complexity of tracing the waves after five bifurcations and small amplitude, they are neglected in this study, and only the primary waves are traced.

3.3.4 PRESSURE WAVEFORMS IN A 15-CONSECUTIVE BIFURCATIONS

The magnitude of pressure measured at the inlet of the parent vessel and the inflow at each terminal point, wherein inflow is injected, are compared against each other. Figure 3.14 shows the ratio of the pressure measured at the beginning of the mother vessel ($P(M)$) to pressure inserted at one of the daughter vessels in each simulation ($P(D)$). There is a two-fold drop in the ratio when the pulse is inserted from the first daughter vessel compared to when the impulse is inserted from the third generation of bifurcation.

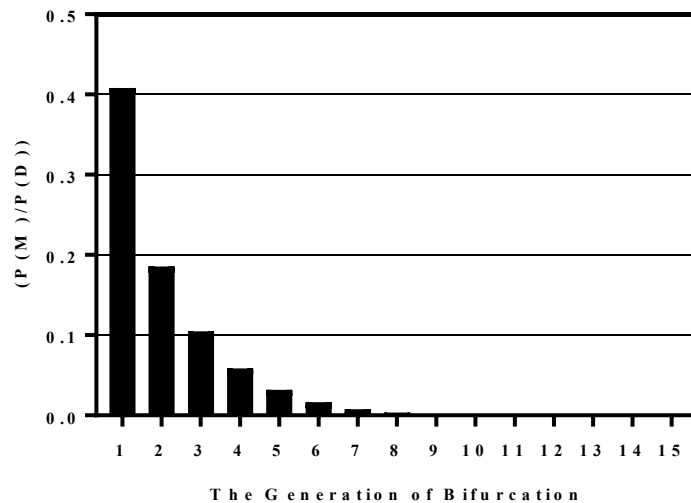


Figure 3. 14. The rate of the measured pressure in the mother vessel, $P(M)$, over the pressure measured in the daughter vessels, $P(D)$, in 15 generations of bifurcations.

As it is shown in Figure 3.14, there is an exponential decay of the ratio with the increase in the number of bifurcations. After the 7th bifurcation, the ratio tends to zero, which means no reflections can be sensed at the stem vessel if there is a blockage after 7th bifurcation.

3.4 DISCUSSION

This study aims to investigate how bifurcations affect the magnitude of reflected waves, and how far reflected waves can travel towards the heart with a discernible quantity. This could be achieved by considering a series of bifurcations ending with complete absorbent boundary condition, extracting the reflections originating from the bifurcations only. Since the length and

the wave speed of the segments are known, the transient time of the reflections can be calculated theoretically using the equation $t = \Delta L/c$.

Similar to many branches of applied mathematics, it is necessary to analyse simple models before increasing the complexity of the modifying feature present in reality. Therefore, the analysis started with a consideration of a single bifurcation with a combination of different terminal boundary conditions such as absorption and blocked for the daughter vessel.

Caro et al. (1978) presented a theoretical analysis of pulse wave propagation. The pulse is expected to be partially reflected at the bifurcation, travelling back to the inlet of the mother vessel. Another part of the waves continues moving in the daughter vessels, and if they encounter clamping or a reservoir, they are reflected and travel back to the bifurcation site and consequently reflected again. Eventually, these reflections and re-reflections diminish in magnitude as a result of wave dissipation.

Khair and Parker (2002) experimentally studied a mismatch bifurcation where the area ratio was $\alpha=0.5$, and one daughter vessel is clamped 70 cm away from the bifurcation, and the other daughter vessel is connected to an open-air reservoir 105 cm away. They have noticed the reflections and re-reflections anticipated in (Caro et al., 1978). Also, some of the waves appeared as a single summation wave. They concluded that in a physiological environment, where there is a very short interval between the arrival of the reflected waves, and reflections and re-reflections are arising from a large number of networks of bifurcations, the localising of the origin of the reflection is hopelessly complicated. In this study, the authors aimed to localise the source of each reflection and follow the path the waves took.

In our study, a similar approach is taken to study the reflections numerically. A numerical model of a symmetrical bifurcation is used to investigate the reflections arising only due to the bifurcation. Hence, the terminal boundary condition for the daughter vessel is completely absorbent, initially. Then, the model is simulated with one blocked daughter vessel and two blocked daughter vessels. With only one blocked terminal point, the number of reflections increases 4-times.

Other than tracing the incident, reflection, and re-reflection waves at two sites in each vessel, there are demonstrated cases that the wave is an amalgamation of two separate reflections. Also, all the values provided by the simulations were validated using the relative equations. In all calculations, there is a difference of less than four per cent between the simulated values in simulations and the manually calculated values.

In the next step, two-consecutive bifurcations were studied, and the location of injecting the inflow is moved from the inlet of the mother vessel and then from the outlet of one of the daughter

vessels at each bifurcation. Similar to previous simulations, the pressure was estimated at two sites in each vessel, and also each value was validated using the relevant equations.

To the best of author's knowledge, this study is first in the literature to replicate a reflection in a system of vessels and trace the waves in their backward direction.

The primary outcome of this study is a demonstration of how the reflected waves are re-reflected between bifurcations. This phenomenon is also known as “wave-trapping” and also mentioned in (Davies *et al.*, 2012). The authors separated the waves into their incident and reflected components in a validated physiological arterial model. They concluded that each bifurcation transmits most of the wave, and a small reflection is travelling back. The reflection travelling back from the second bifurcation encounters with a different reflection coefficient, and therefore most of it is reflected. However, they did not consider the reflections arising from the end of the vessels, which is discussed in this chapter.

Following the results of previous simulations, a five-consecutive bifurcations model is simulated with the pulse described at its stem vessels inlet. First, all the terminal points are entirely absorbent, and then one of the daughter vessels at the fifth generation is blocked. By comparing the pressure and velocity changes, there is negligible change in the pressure at the estimated time for the reflection from the blocked end to reach the inlet. Based on the results of the first simulation, reflected waveforms are discernible when originating from the two initial bifurcations. As the wave travels throughout the model, the magnitude of the reflection decreases and even the reflection from the blocked terminal point is too small to be discerned without magnification of the period 10-15s (Figure 3.13).

Hence, in the next sets of simulations, the imposed 'artificial reflection' is large enough to be detected at the inlet of the mother vessel. The pressure measured in the mother vessel, $P(M)$, was compared against the pressure that was imposed at terminal points of each daughter vessels, $P(D)$, and the results are presented as a ratio (R_p) of the measured pressures. The results show a significant decay in the amplitude of reflected waves reaching the root of the mother vessel, which may indicate that more than half of each wave's amplitude was re-reflected and trapped between each bifurcation. The results of these simulations provided an overview of the ratio of reflections originating from the endpoint of a different generation of bifurcations, as shown in Figure 3.14.

There are some limitations to this study. Energy loss in bifurcations is disregarded in the simulations, while findings of (Mynard and Valen-Sendstad, 2015) suggest more accuracy in the estimation of pressure by considering the energy loss at bifurcations.

Also, compared to the existing models of the arterial system in the literature, the models studied here are relatively simple. However, they reproduce the features of reflected waves in a branching system similar to the arterial tree by easy-to-grasp mechanisms. The absence of reflected waves generated from other terminal points might be an oversimplification, but it allowed the tracking of changes in pressure waveform passing different bifurcations.

Moreover, although not physiological, the length of 5 metres of each segment was used to prevent the overlapping of waves. In contrast to the arterial system, with multiple sites of reflection from tapering and peripheral resistances, the models in this study focus on the effect of the reflections solely due to bifurcations.

3.5 CONCLUSION

Determining a location for wave reflections can be an oversimplification of the matter and might overlook the fact that some reflections are an amalgamation of multiple reflections or re-reflections. A significant decrease in the amplitude of the reflected wave reaching the inlet of the mother segment is evident in all simulations. With the increase in the number of bifurcations, as is the case in vivo, single reflections originating at the periphery may not be discernible at the aortic root. Further work is required to examine the decay of the reflected waves in a more significant number of segments and bifurcations similar to those of the arterial system. Introducing the effect of tapering vessel can give more insight into the propagation of pressure in the arterial system, which will be addressed in the next chapter.

CHAPTER 4

ANALYSIS OF THE RESPONSE OF THE ARTERIAL TREE TO A REFLECTED WAVE

4.1 INTRODUCTION

In Chapter 3, the role of bifurcations in the reduction of the amplitude of pressure was investigated. The computational models in the previous chapter started from easy-to-grasp structures, and the level of their complexity increased. In some of the experiments, a reflection was induced from the peripheral ends, and the amplitude of the turbulences reaching to the parent vessel was measured. In this chapter, a validated computational model of the arterial tree replica is utilized to examine the changes in the amplitude of induced pulse from a peripheral vessel reaching to ascending the aorta.

As it has been suggested in many studies, the reflected wave travelling from the periphery are not significant enough to be sensed at the ascending aorta. Some authors used canine subjects and occluded the arterial tree in different locations along the aorta (Bos *et al.*, 1976; Khir and Parker, 2005), and some others occluded the vessels in computational models to examine the hypothesis (Westerhof *et al.*, 2008). The region of the terminal abdominal aorta is considered to be the major origin of the reflections (Mills *et al.*, 1970; Murgu *et al.*, 1980). On the other hand, some investigators have shown that reflections can arise from many points rather than a single point (Bos *et al.*, 1976; Westerhof *et al.*, 2008).

In an experimental work that was executed by (Peterson and Gerst, 1956), the authors introduced controlled volume pulses from peripheral locations, such as the femoral and iliac artery, in living dogs. There was no evidence of the induced waves reaching the aortic root. They concluded that the reflected waves might not affect the arterial pulse contour, and the arterial tree progressively damps the reflection waves. Since *in vivo* experiments are not feasible to conduct such studies, a 1D-numerical model of the large arterial vessels is used to test the theory. A pulse is inserted in peripheral vessels and the generated waves by being reflected or transient are systematically followed.

The human arterial system can be modelled based on mathematical governing equations with different levels of precisions. Recent studies have shown that 1D models can capture the

main features of the area, pressure and flow waveforms in human conduit arteries, using in vivo measurement (Olufsen *et al.*, 2000; Steele *et al.*, 2003; Davies *et al.*, 2012; Willemet, Lacroix and Marchandise, 2013) and in vitro experiments (Matthys *et al.*, 2007). Therefore, in this study, the validated model extracted from (Matthys *et al.*, 2007) is used. Matthys *et al.* (2007) studied the wave propagation in a human arterial replica and validated the results using the nonlinear 1D models.

Several lumped parameter, or zero-dimensional (0-D), models are usually coupled to 1D models of large arteries to mimic micro-circulation occurring in the capillary beds. In vivo observations shows that in large arteries, the periodic mean pressure and flow distribution depends on peripheral and arterial resistance. In addition, the diastolic decay of pressure in large arteries are influenced by all the peripheral compliances and resistance of the system (Alastruey *et al.*, 2008). The terminal reflection coefficient can be estimated using

$$R_t = \frac{R - Z_0}{R + Z_0}, \quad (4.1)$$

where $Z_0 = \rho c/A_0$ and R is the terminal resistance. For more information about the mathematical formulation of the lumped parameter models, the reader is referred to Chapter 2, Section 2.5 of this thesis.

It worth mentioning that the main aim of this study is to examine the response of the combination of arterial tapering and bifurcation to reflected waves, and the aim is not to replicate the precise physiological environment of the human body.

In section 4.2, the methodology and the computational model's specifications are presented. Results and discussion can be found in Section 4.3 and Section 4.4, respectively. Finally, the conclusion is included in Section 4.5.

4.2 METHODOLOGY

The aim is to investigate the hypothesis that the reflection originated from the periphery is losing most of its amplitude as it reaches to the aortic root. Hence, a semi Gaussian-shaped pulse is induced to the end of a peripheral vessel. The changes of pressure and velocity are monitored along the route of the pulse until the ascending aorta. Using a pulse as the input is a convenient method to measure the response of the system, and it can show the reflections and changes in the amplitude of the pulse (Wang and Parker, 2004; Alastruey *et al.*, 2009).

There is no inflow wave from the heart in the system used in this study. However, the boundary condition for the heart is complete absorbent in one simulation and complete reflector

in another. With these simulations, the possible influence of the arterial valve on the amplitude of reflected pressure reaching the ascending aorta could be investigated. In reflector case, the closed aortic valve (CV) during diastole is modelled, while an absorber boundary condition can be the open aortic valve (OV) during systole, with compromising the output of the left ventricle.

The computational model used in this study was built on the 1:1 silicon replica of 37 largest conduit arteries of the circulatory system, mimicking three generations of bifurcations in the arterial tree (Matthys *et al.*, 2007). For example, the 3rd generation of bifurcation in this model is where the iliac artery is bifurcating into anterior and posterior tibial vessels.

Also, the arterial replica's large vessels are linearly tapered, and the smallest branches had a constant cross-sectional area. The geometrical values of the arterial segment are presented in Table 4.1.

The geometrical properties of vessels, such as wall thickness, diameter and length, were measured using a ruler, calliper and micrometre at the inlet, midpoint and the outlet of the segments after dissecting the model. After performing tensile tests on the sample strips of replica, a constant Young's modulus of 1.2 MPa was measured within the range of pressure of the experiment.

A semi Gaussian-shaped flow wave with a peak value of 2.22 ml s^{-1} is inserted into the left femoral artery, for both close-valve and open-valve, to produce pressure with an amplitude of 20 mmHg, significant enough to reach the ascending aorta. The shape of the inflow is defined as

$$Q(t) = 2.22 * 10^{-6} \exp(-100000(t - 0.05)^2) \text{ m}^3\text{s}^{-1}. \quad (4.1)$$

The terminal vessels, except the right anterior tibial, are coupled to a single resistance Wk model. The initial conditions for all segments are $(A(x, 0), U(x, 0), P(x, 0)) = (A_0(x), 0, 0)$. This model has been used in several studies (Matthys *et al.*, 2007; Alastruey *et al.*, 2011; Boileau *et al.*, 2015).

According to the literature, this model was able to capture the main feature of the in vitro waves in first, second and third generations of bifurcations. Figure 4.1 depicts the schematic representation of the computational arterial structure and inflow. The path that a wave travels to reach the aortic root is shown with a red highlight in Figure 4.1. Across this path, the wave crosses segments 34, 30, 29, 28, 27, 25, 23, 17, 15, 10, 8 and 1 of the Table 4.1. The pressure and velocity in the beginning and the middle point of the segment is used for the analysis.

Table 4. 1. The geometrical and peripheral resistance of segments in the computational arterial tree model.

Segment	Arterial vessel	Length (cm)	$R_{in} \rightarrow R_{out}$ (cm)	Peripheral Resistance (10^9 Pa s m^{-3})
1	Ascending aorta	3.6	1.44→1.30	-
2	Innominate	2.8	1.10→1.30	-
3	R. carotid	14.5	0.54→0.39	2.67
4	R. subclavian I	21.8	0.44→0.33	-
5	R. subclavian II	16.5	0.33→0.28	-
6	R. radial	23.5	0.21	3.92
7	R. ulnar	17.7	0.21	3.24
8	Aortic arch I	2.1	1.30→1.25	-
9	L. carotid	17.8	0.56→0.37	3.11
10	Aortic arch II	2.9	1.25→1.18	-
11	L. subclavian I	22.7	0.44→0.34	-
12	L. subclavian II	17.5	0.34→0.28	-
13	L. radial	24.5	0.21	3.74
14	L. ulnar	19.1	0.21	3.77
15	Thoracic aorta I	5.6	1.18→1.10	-
16	Intercostal	19.5	0.41→0.32	2.59
17	Thoracic aorta II	7.2	1.10→0.93	-
18	Celiac I	3.8	0.4	-
19	Celiac II	1.3	0.43	-
20	Splenic	19.1	0.18	3.54
21	Gastric	19.8	0.19	4.24
22	Hepatic	18.6	0.33→0.29	3.75
23	Abdominal aorta I	6.2	0.93→0.80	-
24	L. renal	12	0.26	3.46
25	Abdominal aorta II	0.7	0.79	-
26	R. renal	11.8	0.26	3.45
27	Abdominal aorta III	10.4	0.78→0.59	-
28	R. iliac-femoral I	20.5	0.39→0.34	-
29	R. iliac-femoral II	21.6	0.34→0.23	-
30	R. iliac-femoral III	20.6	0.23→0.21	-
31	L. iliac-femoral I	20.1	0.40→0.33	-
32	L. iliac-femoral II	19.5	0.33→0.22	-
33	L. iliac-femoral III	20.7	0.23→0.21	-
34	R. anterior tibial	16.3	0.15	Inflow
35	R. posterior tibial	15.1	0.15	5.65
36	L. posterior tibial	14.9	0.16	4.59
37	L. anterior tibial	12.6	0.15	3.16

In the simulations, the density and viscosity of the blood are constant and assigned to be 1050 kg m^{-3} and 2.5 mPa s , respectively.

The same structure is also tested with an inflow wave with double pulse width to a) test the reproducibility of the data, and b) to investigate the influence of the size of the pulse on the response of the system.

$$Q(t) = 2.22 * 10^{-6} \exp(-100000(t - 0.05)^2) \text{ m}^3\text{s}^{-1}. \quad (4.1)$$

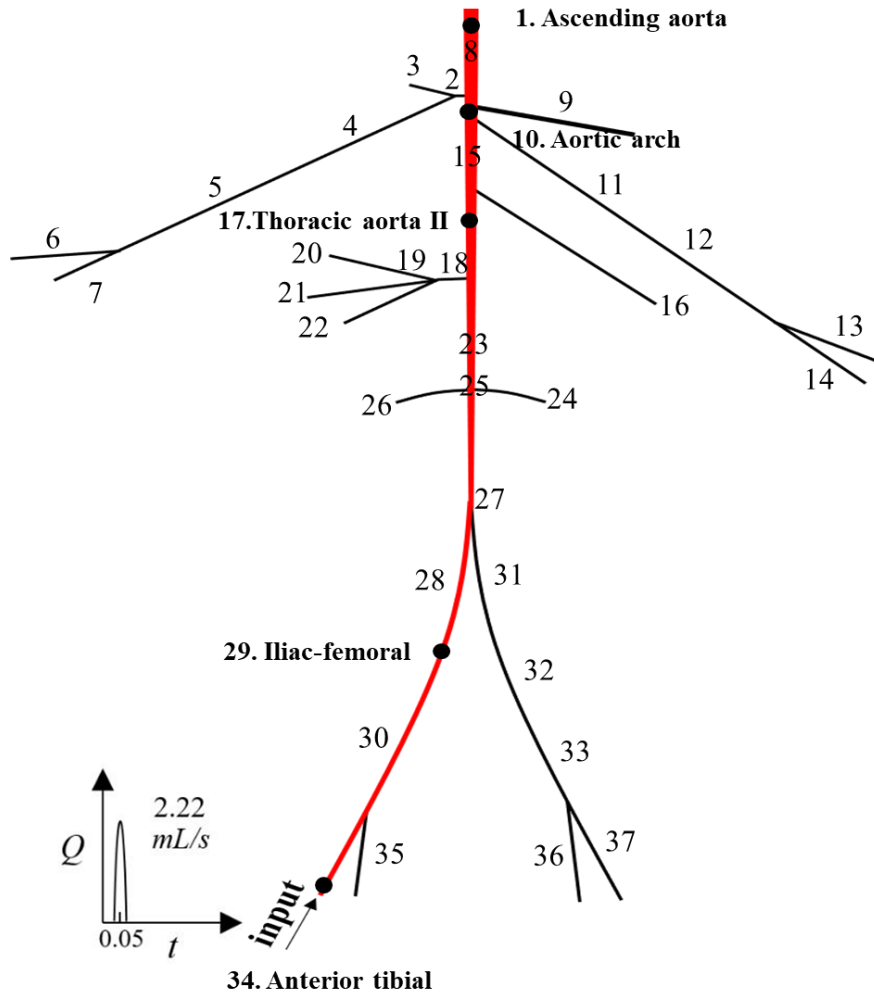


Figure 4. 1. A schematic representation of the arterial tree model and the impulse. Each number stands for a segment which is further explained in Table 4.1. The estimated pressure and velocity of the black dots are shown in Figure 6.2.

Inducing a pulse as a reflection to a system can cause confusion in the previously defined notions. For example, although the generated pulse is travelling from a distal location, it is not a reflected wave because it is not generated as an outcome of encountering of an incident wave to a reflection site.

Hence, it is necessary to establish a system of definition for this study. Any wave regardless of its source travelling from the distal locations towards the heart is a backward wave, and any wave travelling from the heart towards the peripheral beds is a forward travelling wave. It is worth mentioning that a reflected wave can move in both forward or backward directions. For

example, if a reflection reaches the closed aortic valve, it is again reflected in the forward direction.

The backward pressure is calculated using Equation 2.67 and differentiation of pressure and velocity resulted from the numerical experiments. In the simulations, the density and viscosity of the blood are constant and assigned to be 1050 kg m^{-3} and 2.5 mPa s , respectively. The wave speed at each location is calculated using the Moens-Korteweg equation (Equation 1.2).

4.3 RESULTS

The pressure and velocity in 11 different locations along the aorta and iliac artery are estimated. Figure 4.2 depicts the results in five locations in both the open valve and close valve simulations. The input pulse pressure is shown in the right anterior tibial artery. The pressure in both open and close valve at anterior tibial is similar, while at the ascending aorta, the amplitude of the closed valve is about 1.7 times higher than the open valve.

The amplitude of pressure and velocity reduces as the pulse travels towards the ascending aorta, with only 1 % of the pressure amplitude and 1.6 % of the velocity amplitude reaching the ascending aorta. A consecutive presentation of the pressure waves on the route of the pulse towards the ascending aorta is shown in Figure 4.3. At $t = 0.161$ seconds the wave encounters with the iliac bifurcation, and there is a sudden reduction in the amplitude of the pulse.

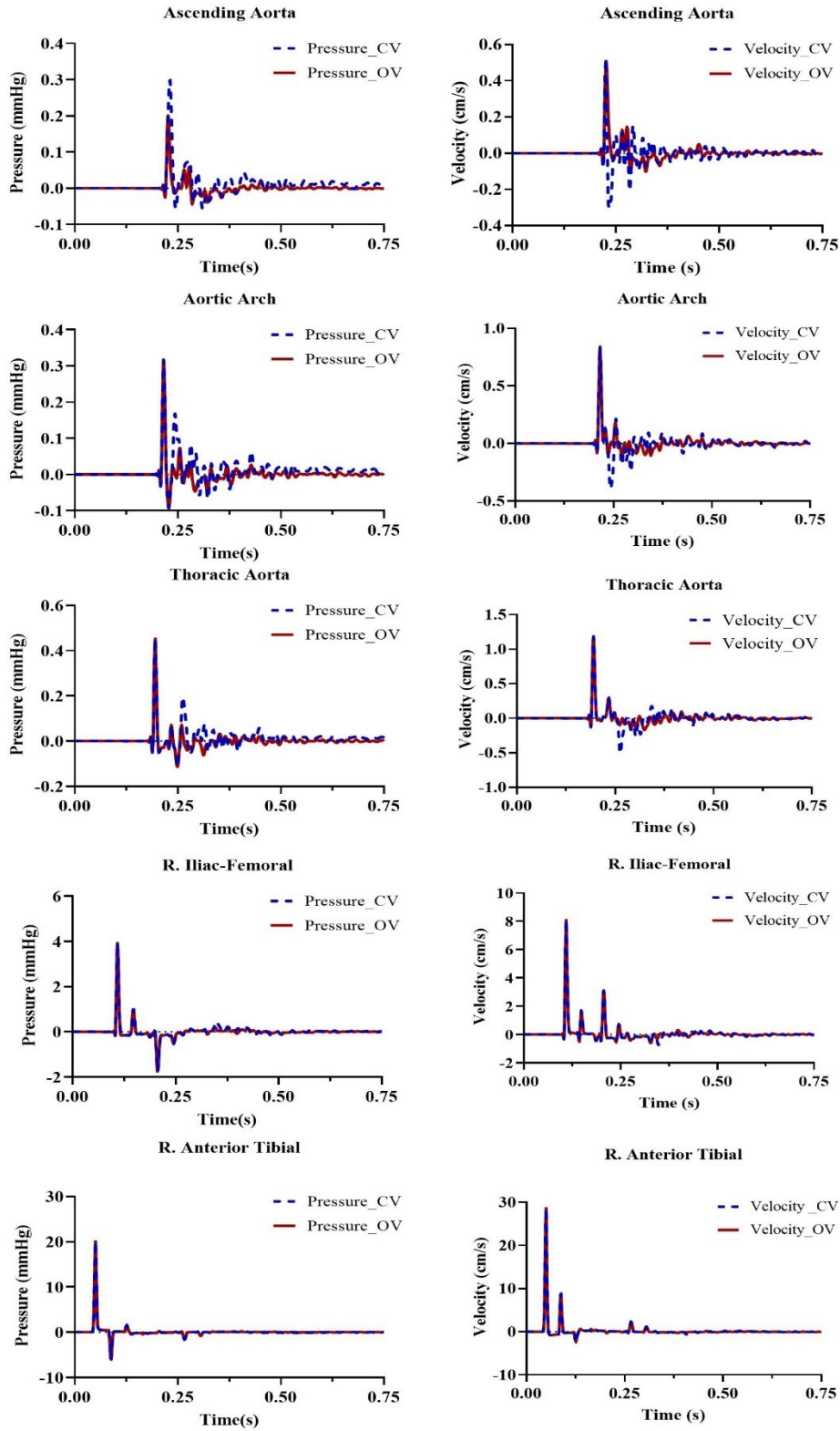


Figure 4. 2. The estimated pressure (left column) and velocity (right column) in five locations along the aorta and iliac artery in open valve (OV) and close valve (CV) conditions.

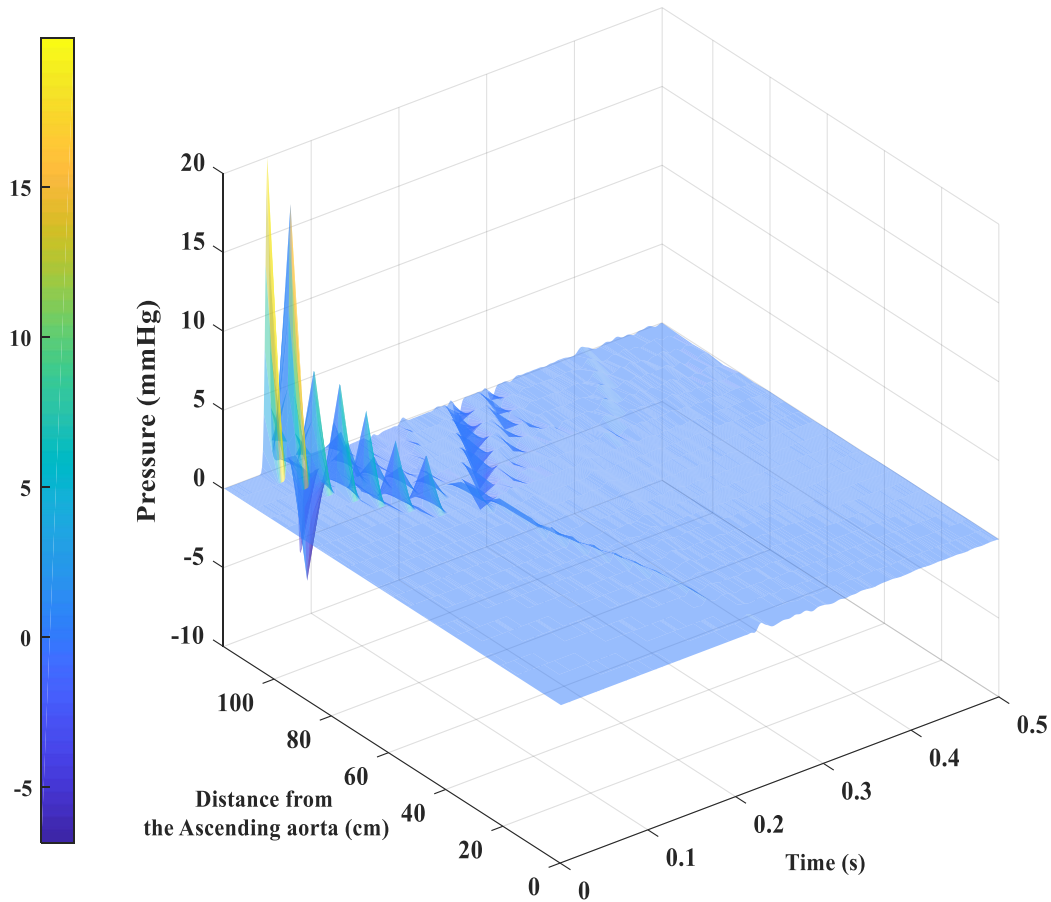


Figure 4. 3. The pressure amplitude of pulse travelling the arterial tree in the reverse direction with a close valve. The inflow is induced at R. anterior tibial, about 118 centimetres away from the ascending aorta.

Compared to the inflow, the turbulence arriving the ascending aorta is not significant. The same trend can be seen in the changes in the velocity, as shown in Figure 4.4.

The pressure is separated into its forward and backward travelling components using the method presented by (Parker and Jones, 1990). Since the direction of the reflection is assigned to be in the backward direction, the changes in amplitude of the pressure show the response of the arterial tree to an imposed reflected wave arising from peripheral limbs.

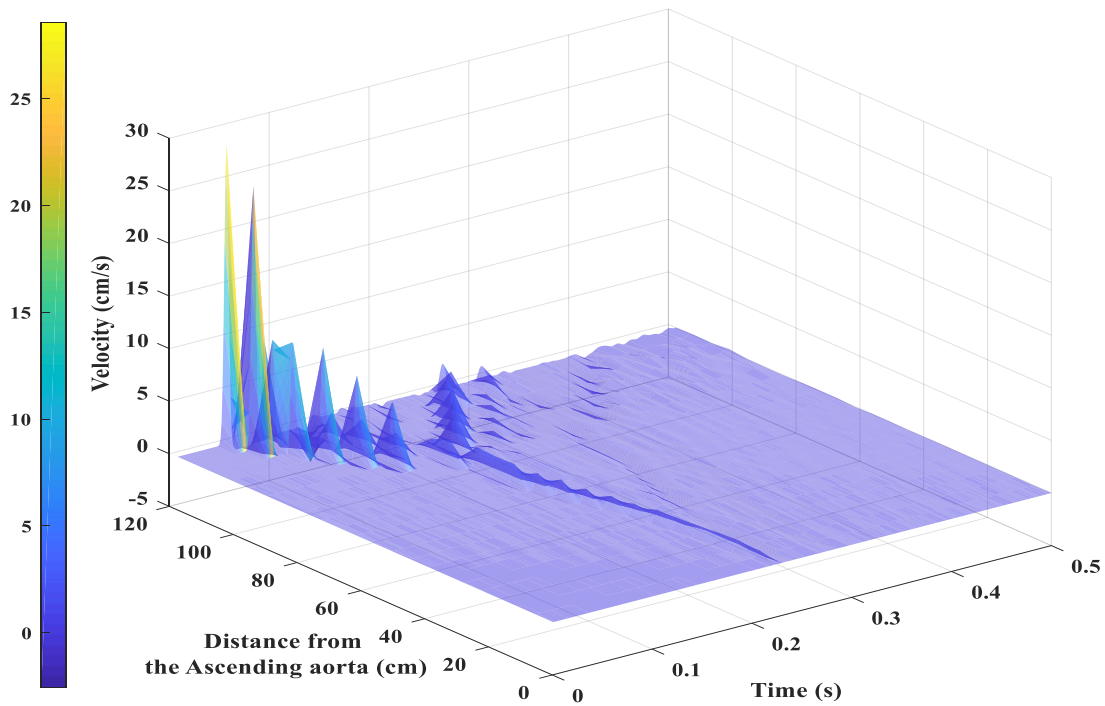


Figure 4. 4. The velocity amplitude of pulse travelling the arterial tree in the reverse direction with a close valve (CV). The inflow is induced at R. anterior tibial, about 118 centimetres away from the ascending aorta.

Figure 4.5 shows the backward component of pressure in different locations of the aorta from the terminal region of abdominal to the ascending aorta (33.5 cm). In addition, the forward pressure along the left iliac artery is shown on the left (58.50 cm).

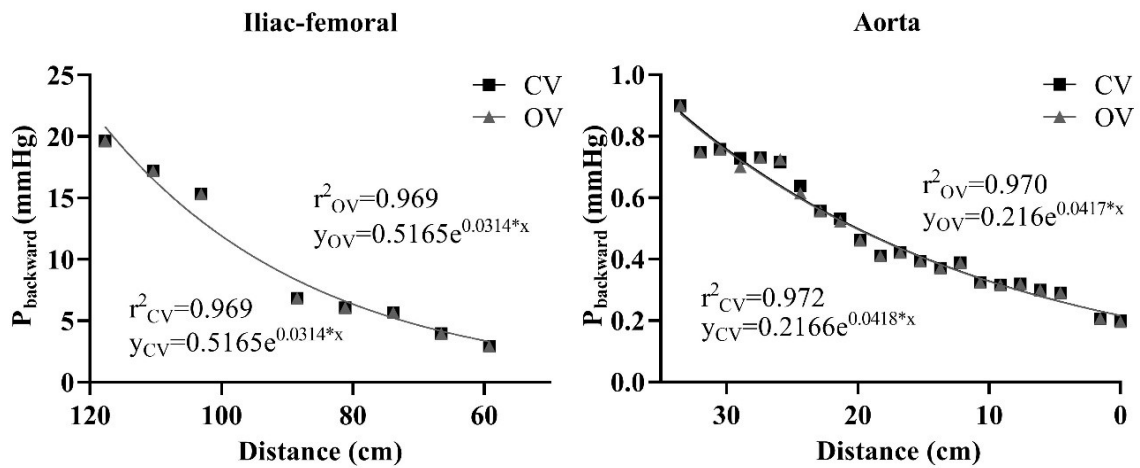


Figure 4. 5. The backward pressure component of the pulse induced at the R. anterior tibial in iliac-femoral (left) and the aorta (right), both in CV and OV conditions. The locations are separated into two different graphs so that the difference between the values in the aorta be visible

As shown in the figure above, the backward pressure reduces 19 mmHg before reaching to the distal part of the abdominal aorta, indicating that a reflected wave starting from the end of femoral loses 95 % of its amplitude. There is no significant difference between the OV and CV conditions in the backward pressure.

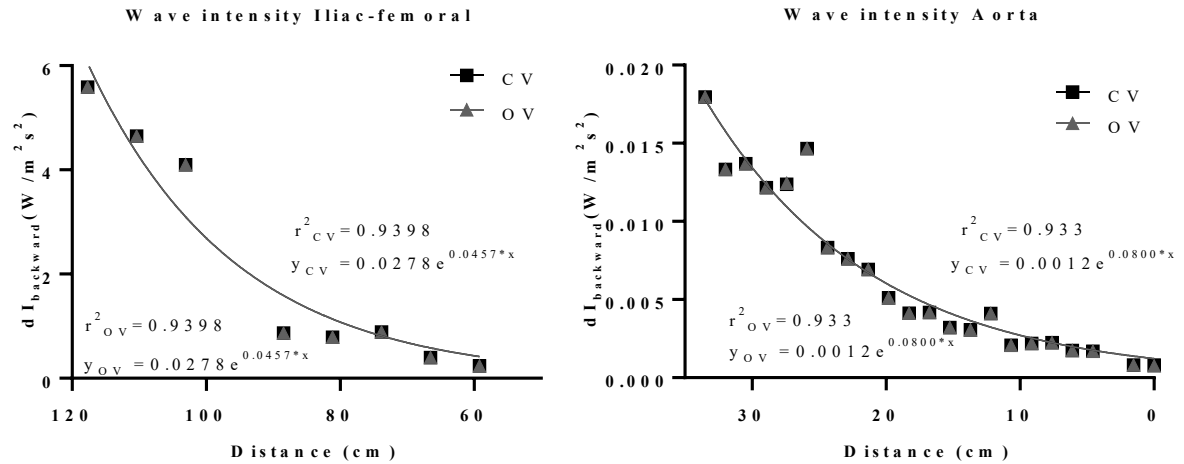


Figure 4. 6. Wave intensity analysis in the backward direction for the imposed pulse at the R. anterior tibial. The left figure shows the intensity in the right distal iliac, and the right figure shows the intensity in the aorta. The locations are separated into two different graphs so that the difference between the values in the aorta be visible

The changes in the intensity of the wave are more significant than the pressure. As shown in Figure 4.6, the wave intensity at the inlet of the right anterior tibial is $6 W/m^2 s^2$, while the intensity at the distal part of the abdominal aorta is approximately $0.018 W/m^2 s^2$.

To further scrutinize the pressure in the arterial system, a single tapered arterial vessel is chosen, and alterations in the pressure at the inlet, midpoint and the outlet of the vessel are compared. Figure 4.7 depicts the pressure along the right iliac artery before the iliac bifurcation.

The pressure at point 3 is the inflow to the vessel. The reduction of pressure at point 2 is caused by friction. The reflection coefficient of iliac bifurcation influences the pressure reaching to point 1 in addition to the reduction caused by tapering and friction. The reflection coefficient at the iliac bifurcation as the wave approaches from the right iliac is -0.5.

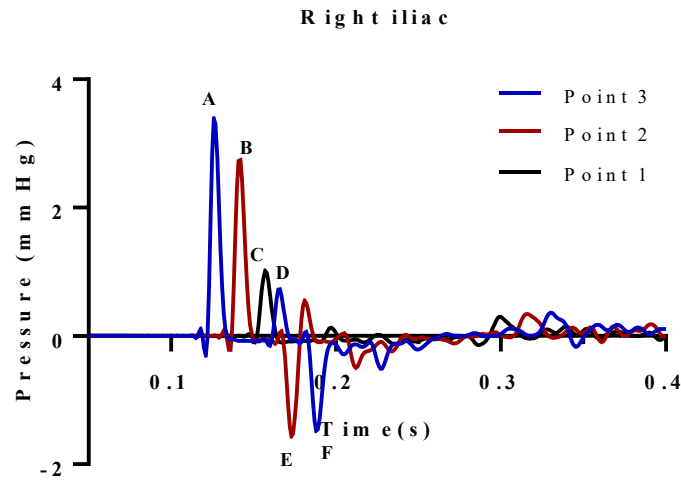


Figure 4. 7 Pressure waves in the right iliac artery at the distal point, midpoint and proximal to the iliac bifurcation.

Each wave is labelled alphabetically, and the description of the waves are presented in Table 4.2. When the pressure is travelling towards the aorta (A to B), the reflection caused by tapering is higher compared to the re-reflection travelling away from the aorta (E to F).

Table 4. 2. Description of the waves in the right iliac artery shown in Figure 4.7

Wave	Amplitude (mmHg)	Description
A	3.386	The pressure travelling from the anterior tibial loses 16.614 mmHg
B	2.741	A decrease of 0.645 mmHg due to tapering and friction of the vessel
C	1.011	A reduction due to tapering, friction and bifurcation ($R_f = -0.5$)
D	0.727	A possible re-reflection from distal iliac and femoral
E	-1.563	the reflection caused by the bifurcation
F	-1.475	Wave E with 0.088 mmHg reduction due to friction

Furthermore, the pressure transfer at the iliac bifurcation is shown in Figure 4.8 shows that a higher proportion of the transient wave is travelling toward the left iliac (43 %) compared to the distal abdominal (32 %).

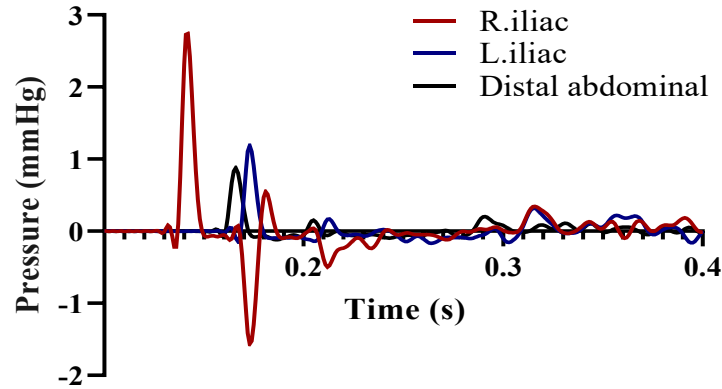


Figure 4. 8. The pressure transfer at the iliac bifurcation with a pulse induced from right anterior tibial. The middle point of each vessel is selected.

Similar simulation is done with an inflow with a pulse with doubled width. The pressure and velocity pattern through the route of the pulse travelling to the ascending aorta is presented in Figure 4.9.

With a higher pulse width, the reflection is overlapped and less discrete. However, the amplitude and contour of the pressure wave below the abdominal are similar in both pulses. The most significant effect of higher pulse width can be noticed at the ascending aorta. The pressure in OV and CV changed from 0.2 and 0.3 mmHg to 0.27 and 0.6 mmHg.

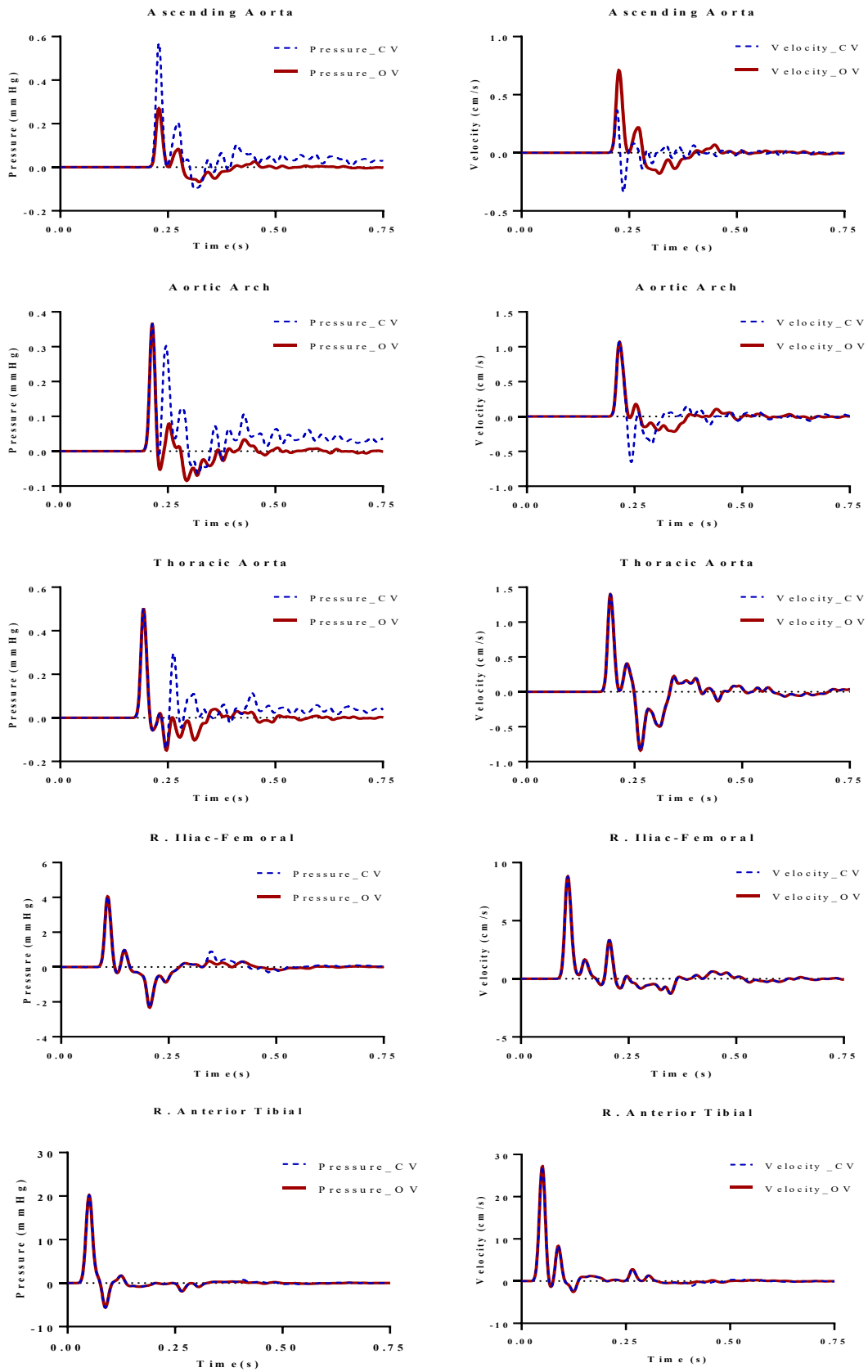


Figure 4. 9. The estimated pressure (left) and velocity (right) at five locations in the arterial tree as the pulse is inserted in the right anterior tibial.

The results of wave intensity analysis, as shown in Figure 4.10, for the pulse with higher width within the iliac-femoral vessel is similar to the previous simulations, while along the aorta wave intensity is about 20 % less.

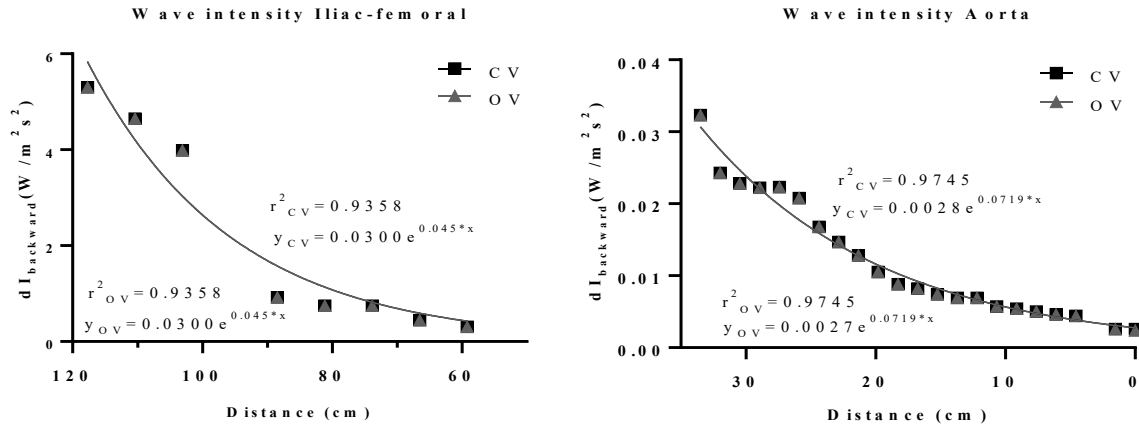


Figure 4.10. Wave intensity analysis in the right iliac- femoral artery (left) and the aorta (right) as the pulse travels towards the ascending aorta. The locations are separated into two different graphs so that the difference between the values in the aorta be visible

4.4 DISCUSSION

In this chapter, the findings of the previous chapter are expanded by comparing the amplitude of the pressure of the wave reaching to the ascending aorta as the right anterior tibial being its origin. The wave loses most of its amplitude before reaching to the abdominal aorta due to friction and the tapered structure of the arterial tree. Furthermore, by reaching the iliac bifurcation, in addition to 50% reflection, about 40% of the wave is diverted towards the left iliac artery. Finally, by comparing the pressure induced to the system and the pressure at the root, only 1 % of the amplitude of the initial wave survives the reflections and reaches to the ascending aorta. This finding is in agreement with the results reported in (Peterson and Gerst, 1956). Since they were performing their experiment on a living dog with a pumping heart, not sensing any changes in pressure at the root can be expected. As the results show, only 1 per cent of the wave amplitude reached the ascending aorta.

Using an arterial inflow as well as a pulse in an arterial tree model can confirm the findings of the study by (Peterson and Gerst, 1956). Hence, a limitation of this study can be the absence of a pumping heart and its influence on the response of the system.

In the reference (Alastruey *et al.*, 2009), the authors used a single wavefront at the root of 1D model of the 55 conduit arteries to study the conduit components of a 1D model of the 55 conduit arteries and the pattern of the reflections occurring in the arterial tree. They reported

that the changes in the pressure waves associated with the reflection could be both positive and negative. However, the amplitude of the wave regardless of their sign inclines exponentially. Although the pulse in this chapter is not inserted from the aortic root, the reflections absolute value tends to decrease exponentially. Moreover, our results are in agreement with (Hiland and Anliker, 1973), which report an exponential decay pattern in the amplitudes of the waves travelling in either direction.

In Figure 4.7, the estimated pressure at three points in the right iliac artery is shown. It could be seen that the pressure loss when pressure is travelling towards the aorta is higher than when the wave is travelling towards the periphery. The same phenomenon was observed in (Hiland and Anliker, 1973; Reuderink, Sipkema and Westerhof, 1988), where they reported the reflected waves to dissipate faster than the downward travelling waves, and they related this difference to the tapering of the aorta. Similarly, it could be assumed that the tapering augments the reflection of the waves. However, a quantitative analysis of the effect of tapering on waves and pressure is absent in the literature.

The condition of the aortic valve in our study only affects the pressure amplitude at the ascending aorta, which almost doubles the absolute value in the CV. The changes in other sites of the arterial tree are not significant.

Another limitation of this study is that the energy loss at the bifurcations is neglected, which can further reduce the amplitude of the pressure travelling towards the aorta and provide more precise estimation (Mynard and Valen-Sendstad, 2015).

The backward direction is considered to be the direction that the pulse travels from the periphery to the root or the direction of the 'imposed reflection'. The amplitude of the transient backward pressure diminished exponentially as it travelled along the iliac and then the aorta. By reaching to the iliac bifurcation, 15 mmHg of the pressure wave is lost (Figure 4.5). There is no significant difference between CV and OV in the pressure.

Using wave intensity analysis can be beneficial since it takes into account the effects of fluid viscosity, the vessels' wall viscoelastic properties and frictional effects (Parker, 2009). Therefore, the wave intensity is used to study the response of the arterial vessels to a reflected pulse wave.

The exponential decay of the backward intensity, as shown in Figure 4.6, is higher compared to the pressure. The intensity of the wave arriving in the root is almost zero. To the best of our knowledge, this is the first study to evaluate the wave intensity of an imposed reflection. However, it is expected to be negligible as it is being reflected by either tapering of the arterial tree or the bifurcations.

Doubling the pulse width caused overlapping of waves and an increase in pressure in the aorta. This rise of pressure is also influencing the wave intensity. As shown in Figure 4.10, the intensity values in the aorta are higher at the same sites compared to the values of intensity of the shorter pulse across the aorta. The wave intensity in iliac and femoral vessels are similar for both pulses, suggesting that the overlapping of reflections and re-reflections caused by higher width is more effective in the aorta.

4.5 CONCLUSION

Using a 1D arterial model, the results of this chapter show that only 1% of the magnitude of pressure of a reflected wave originated at the iliac artery can be seen in the aortic root. About 75 % of the wave is lost before reaching the distal aorta before the iliac bifurcation.

The results indicate that reflections generated at distances more than 100 *cm* cannot be discerned at the ascending aorta. Therefore, it can be hypothesized that the reflected waves seen in the ascending aorta in vivo are generated more proximally in the aorta, produced by either the local discontinuity in the structure or the neck and cerebral circulations.

The results also indicate that arterial bifurcations and tapering cause a large reduction in the magnitude of reflected waves. Quantitative analysis for separating the effect of tapering from the bifurcations will be examined in Chapter 6.

CHAPTER 5

IMPACT OF TAPERING ON THE PRESSURE AMPLITUDE AND REFLECTIONS

5.1 INTRODUCTION

One of the known normal characteristics of the arterial system is its tapered structure, i.e. the gradual reduction of the cross-sectional area of the vessels (Caro *et al.*, 2011). Analysing the dynamics of blood flow in tapered structures is vital for understanding the development of pressure. Furthermore, according to findings of (Hickson *et al.*, 2010; Charlton *et al.*, 2019), with ageing the diameter at the level of the ascending aorta and the aortic arch increases while the diameter of descending aorta remains the same. This means an increased tapering angle with ageing and hence the interest in the effect of tapering and its variation.

Any discontinuity in the geometry or the elasticity of the arterial system generates reflections. Due to the spatially varying elastic properties of the vessels and the branching structure of the arterial tree, wave reflections are always present in vessels. These reflected waves can also be re-reflected multiple times (Alastruey *et al.*, 2009; Davies *et al.*, 2012), causing intricate patterns in the pressure waveform. Although the identification of reflection site has been the focus of many studies, understanding of the matter is still not completely comprehensive (Segers *et al.*, 2017).

While the changes in capillary blood vessels can be well-captured with Windkessel (Wk) models (Stergiopoulos, Young and Rogge, 1992; Olufsen, 1999), and the impact of bifurcations has been previously studied (Greenwald, Carter and Berry, 1990; Khir and Parker, 2002; Mynard and Valen-Sendstad, 2015; Abdullateef *et al.*, 2019), the direct influence of tapering and its contribution to the reflections needs more research.

The earliest research considering the changes of cross-sectional area and its mechanical effects was conducted by Patel *et al.* (1963), where the dimensions of various sites along the aorta were measured in 30 living dogs. However, the rate of tapering varies from species to species, and the ratio presented by Patel *et al.* does not justify the tapering rate in human. Later, some studies approached the matter using the concept of admittance in the cardiovascular system (Lighthill, 1967; Pedley, 2003). The drawback of this approach is the inability to study

the axial location of the reflections. Therefore, they assumed that if the reduction in the cross-sectional area is sufficiently gradual and occurs over a considerably longer length compared to the wavelength, the reflected energy caused by the tapering is small and can be neglected as the wave travels through the vessel.

Regarding the alteration in pressure (P), Fung (1996) proved that if the energy transmits completely while the cross-sectional area is decreasing gradually, the amplitude of the pressure is proportional to the square root of the characteristic impedance (Z):

$$P = \text{constant} \times \sqrt{Z}, \quad Z = \frac{\rho c}{A}, \quad (5.1)$$

where ρ denotes blood density; A is the cross-sectional area of the vessel, and c is the pulse wave velocity or wave speed. With a reduction in the cross-sectional area, there is a corresponding increase in admittance and pressure.

Bauer et al. (1972) used an experimental setup consisting of three uniform vessels with diameters being inversely proportional to their impedances, and the waves were analysed in the frequency domain. Their results only showed the alteration in the amplitude of pressure but yielded no information about the location of the origin of the reflected wave. Another experimental study was conducted by Reuderink et al. (1988), using the pressure measurement at three different points, i.e. the ‘three-point method’, to study the effect of tapering and to validate the propagation coefficient. The authors use Womersley’s theory to calculate the longitudinal and transversal impedance and compare the results with the foot-to-foot method. They concluded that the increase in the tapering angle leads to higher discrepancies. In their study, they attempted to prove that the reflections are not generated by one isolated origin but a superimposition of multiple reflection sites. Nevertheless, re-reflected waves were not considered.

Segers and Verdonck (Segers and Verdonck, 2000) evaluated the tapered aorta as segments of a transmission line mathematical model. They concluded the reflection present in the aorta is the outcome of two interacting phenomena: the continuous reflection caused by tapering and reflections originating from the diaphragm level. Using the frequency domain approach, they observed that the constant reflection caused by tapering is hidden in the input impedance pattern.

A study by Mu et al. (2013) examined the effect of tapered angles on the distribution of blood flow, considering the effect of gravity. They computationally modelled a single carotid artery with three different tapering angles. They concluded that gravity had no relation with tapering angles, and with the larger tapering angle, the distribution of the blood flow pressure

is improved. There was no conclusion on how tapering affects the reflections and the amplitude of pressure.

More recently, Mynard and Smolich (2014) computationally assessed the waves in diastole using a 1D-Wk mathematical model, and they compared changes of diameter in three different simulations: two-stepwise and three-stepwise diameter reduction and a continuous tapered structure; their results showed that in conical vessel waves are merged, and the pressure decays smoothly.

To the best knowledge of author's knowledge, most of the previous studies on the problem of tapering have applied the transmission line theory using frequency-based methods, and none investigated the effect of tapering on wave intensity analysis (WIA). Therefore, this work aims to examine the impact of vessel tapering on the changes of pressure and flow waveforms using a 1D time-domain model. Also, the aim is to investigate the effect of varying the tapering angle on WIA.

5.2 METHODOLOGY

Five different sets of simulations (studies) are used to study the reflected waves in a tapered vessel. The first study revisits the traditional approaches used in (Lighthill, 1967; Pedley, 1980, 2003), which is a stepwise reduction of the area in a vessel, in the time domain (Section 5.2.1). In the second study, there is a comparison between a straight vessel, a continuously tapered vessel, and a 4-stepwise reduction and five stepwise reductions in the diameter to highlight the difference amongst methods of modelling tapering (Section 5.2.2). A combination of the stepwise tapered vessel connected to a bifurcation is examined in three different lengths (Section 5.2.3). The fourth simulation is a model of the thoracic aorta which is used for studying the effect of varying tapering angles (Section 5.2.4). Then a more complex model of the aorta consisting of the thoracic aorta connected to an iliac bifurcation is studied in Section 5.2.5. The branches along the abdominal aorta are compromised.

5.2.1 REFLECTIONS IN THREE-STEPWISE AREA REDUCTION

In order to analyse the discrete reflections originating from a tapered structure, a vessel composed of three 5-metre long segments with stepwise decreasing diameter was designed. This model aims to trace the path of reflections and their time of occurrence in a simple setup, where the effect of tapering is magnified by using the stepwise reduction of the diameter.

Table 5. 1. The dimensions and properties used in the structure with a three-stepwise reduction in diameter.

Property	Description	Value (unit)
L_1, L_2, L_3	Length	5 (m)
A_{in1}	Diastolic area of segment 1	3.14 (cm ²)
A_{in2}	Diastolic area of segment 2	2.98 (cm ²)
A_{in3}	Diastolic area of segment 3	2.83 (cm ²)
h	Wall thickness	1.2 (mm)
E	Young's modulus	500 (kPa)
ρ	Blood density	1050 (Kg/m ³)
μ	Blood viscosity	4 (mPa s)

A half-sinusoid flow wave is prescribed at the inlet of the structure. Changes in pressure are measured at the inlet of each segment. The decrease in the diameter was uniform, each succeeding part has a diameter 10% smaller than the previous one, to represent a crude effect of a tapered structure. The dimensions and properties are presented in Table 5.1.

The 5-metre long segments provide enough distance and travel time for reflections to emerge separately, since the calculated PWV_{MK} is 6.17 m/s. Figure 5.1 depicts the schematic representation of the structure and the locations where the pressure is estimated.

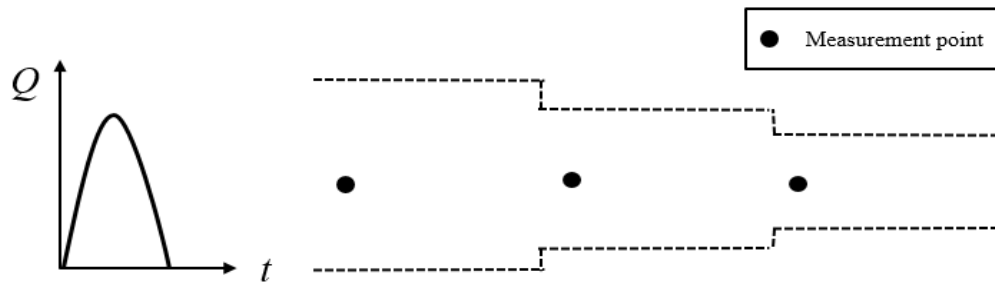


Figure 5. 1. A schematic representation of a tapered structure with a three-stepwise reduction in their diameter

5.2.2 REFLECTIONS IN STEPWISE DIAMETER REDUCTION AND CONTINUOUSLY TAPERED VESSEL

The three factors that describe tapering are the inlet area, the outlet area, and the length of the structure. A comparison between four and five stepwise reductions in the diameters of the vessel and the continuously tapered vessel is made, as shown in Figure 5.2. The inlet and outlet diameter of all structures are kept unchanged in the tapered structures. The tapering angle (Θ) is calculated using

$$\tan\theta = \frac{D_{in} - D_{out}}{2L}, \quad (5.2)$$

where L is the length, D_{in} and D_{out} are the diameter at the inlet and outlet of all the vessels. The length of the vessel was assigned to be two metres to highlight the overlapping of the reflected waves. The angle of tapering in this study is 0.5 degrees, which falls into the range of physiological tapering (Segers and Verdonck, 2000).

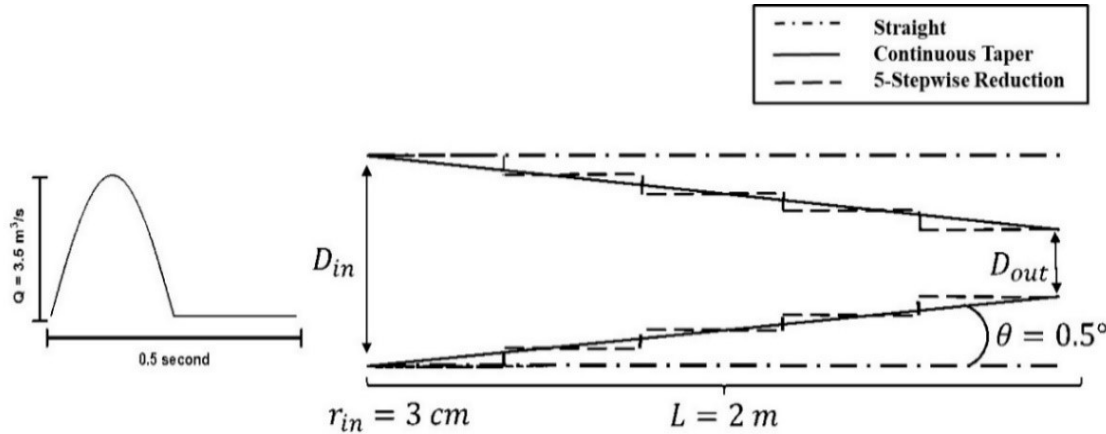


Figure 5. 2. Stepwise tapering of a vessel compared to a continuously tapered vessel. The tapering angle in all the structures is similar

The diameter at the inlet is 6 cm, and it reduces to 2.5 cm at the outlet. The dimensions and properties used in the models are presented in Table 5.2.

Table 5. 2. The properties used in the comparison of 4 stepwise, five stepwise diameter reduction, continuous tapered, and straight vessel

Property	Description	Value (unit)
L	Length	2 (m)
A_{in}	Diastolic area of the inlet	28(cm ²)
A_{out}	Diastolic Area of outlet	4.94(cm ²)
h	Wall thickness	1.2 (mm)
E	Young's modulus	500 (kPa)
ρ	Blood density	1060 (Kg/m ³)
μ	Blood viscosity	4 (mPa s)

To avoid the reflections for at the outlet, the terminal boundary condition is complete absorption.

5.2.3 A COMBINATION OF STEPWISE TAPERING AND A BIFURCATION

A stepwise tapered bifurcation, as shown in Figure 5.3, is simulated with three different lengths of segments to study the contribution of their reflections and the overlapping of waves

as the segments become shorter. In the first case, the length of the mother vessel is 30 metres in total, which consists of six segments that are 5 metres. The daughter vessels are 5 metres each, divided into five, 1-metre segments. In the next analysis, each segment is 16 times shorter than the previous structure, resulting in the mother vessel and daughter vessel to be 0.312 metres and 0.062 metres, respectively.

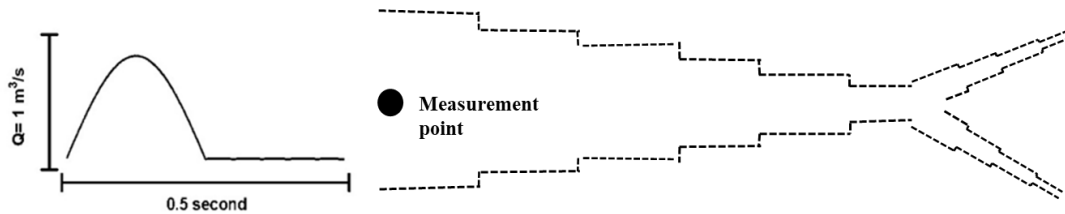


Figure 5. 3. A combination of a stepwise tapering and bifurcation. The measurement point is located at the inlet of the parent vessel.

Finally, in the third case, the length of the mother vessel is 0.469 metres, with six 0.078 metres segments, and the length of the branches is 0.390 metres in total. The total length in the last case is reduced to 0.859 metres, resembling the length of the aortic trunk and the iliac bifurcation. The blood viscosity and density in all simulations are 4 mPa s and 1050 kg/m^3 , respectively. The inlet boundary condition is a half-sinusoid flow waveform. The duration of the flow is 0.5 second, and the peak of flow is 20 Lit/min . As in the previous section, the outlets of the daughter vessels are entirely absorbent. The length and diastolic area of segments are presented in Table 5.3.

Table 5. 3. The dimension of vessels used in tapered vessels and a bifurcation. In simulation 1, the segments are 5 metres long, and in simulation 2, the length of each segment is 0.3125 metres, and in simulation 3, the segments are 0.07 metres.

Property	Simulation 1		Simulation 2		Simulation 3	
	Parent vessel	Daughter vessels	Parent vessel	Daughter vessels	Parent vessel	Daughter vessels
L , Length (m)	30	15	1.87	0.94	0.55	0.27
A_d , Diastolic area (cm^2)	3.14	1.18	3.14	1.18	3.14	1.18
h , Wall thickness (mm)	1.20	1.20	1.20	1.20	1.20	1.20
E , Young's modulus (kPa)	400	400	400	400	400	400

5.2.4 TAPERING IN THE UPPER THORACIC AORTA

The model used for the upper thoracic aorta is a single vessel with constant wall thickness, connected to a three-element Wk model as the terminal boundary condition, and has been

previously used in various studies (Xiao, Alastruey and Figueroa, 2014; Boileau *et al.*, 2015). The three elements of Wk model are the proximal resistance, R_1 , distal resistance, R_2 , and compliance, C . R_1 is connected in series with the parallel combination of R_2 and C (Figure 5.4).

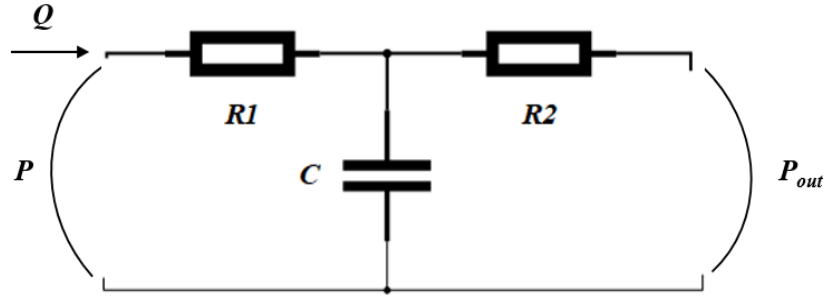


Figure 5. 4. The three-element Windkessel model connected to the outlet of the thoracic aorta.

Table 5.4 shows the values which are used in the model. The outlet cross-sectional area varies in relation to the tapering angle. The physiological tapering angle in human vessels has been reported to be up to 1.5 degrees (Segers and Verdonck, 2000). The inflow boundary condition is also described in (Xiao, Alastruey and Figueroa, 2014).

Table 5. 4. The properties used in the thoracic aorta model taken from (Xiao, Alastruey and Figueroa, 2014)

Property	Description	Value (unit)
L	Length	24.1 (cm)
A_{in}	Diastolic Area of the inlet	4.5(cm ²)
h	Wall thickness	1.2 (mm)
E	Young's modulus	400(kPa)
$A(x,0)$	Initial cross-sectional	3.06 (cm ²)
$U(x,0)$	Initial flow velocity	0
$P(x,0)$	Initial pressure	0
ρ	Blood density	1060 (Kg/m ³)
μ	Blood viscosity	4 (mPa s)
R_1	Wk resistance	1.175 x 10 ⁷ (Pa s m ⁻³)
R_2	Wk resistance	1.116 x 10 ⁸ (Pa s m ⁻³)
C	Wk compliance	1.016 x10 ⁻⁸ (m ³ Pa ⁻¹)

According to (Epstein *et al.*, 2015), if the nonlinearities and the inertia terms are neglected, and it is assumed that pulse wave transit durations along a vessel is much smaller than the duration of the cardiac cycle, then the arterial compliance (C_v) and resistance (R_v) can be derived by

$$C_v = \frac{K_1}{\rho}, \quad K_1 = \int_0^l \frac{A_0}{c_0^2} dx, \quad (5.3)$$

$$R_v = 2(\gamma + 2)\pi\mu K_2, \quad K_2 = \int_0^l \frac{1}{A_0^2} dx. \quad (5.4)$$

c_0 is the wave speed at the initial value of the cross-sectional area (A_0), μ is the viscosity of the blood, and $\gamma = 9$ is a constant value used for the shape velocity profile. A detailed explanation of the calculation of the vessel's resistance and compliance is provided in Appendix I.

5.2.5 TAPERING IN THE AORTA AND ILIAC BIFURCATION

A symmetrical iliac bifurcation is connected to the upper thoracic aorta with its side-branches; namely, brachiocephalic, left carotid and left subclavian and the descending thoracic aorta. The descending thoracic aorta is modelled as a straight vessel with constant wall thickness and no side-branches, as shown in Figure 5.5. According to the finding of (Hickson *et al.*, 2010), with ageing the aortic arch increases both in length and cross-sectional area, therefore in this study, different tapering angles are only applied on descending aorta. The linear tapering is implemented by changing the diameter at the end of the descending aorta using Equation 5.2. The area and the wall thickness of other segments are kept constant.

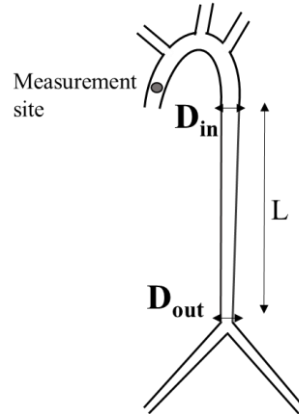


Figure 5. 5. Schematic representation of the model consisting of the upper thoracic aorta and its side-branches connected to the iliac bifurcation

The terminal boundary condition for the iliac vessels is a three-element Wk model. The parameters used in the models are presented in Table 5.5. The blood viscosity and density are 2.5 mPa s and 1040 Kg/m^3 , respectively. The initial pressure and velocity are defined as $(A_0, U_0) = (A_d, 0)$.

The inlet diameter kept unchanged so that the interaction of the input boundary condition and the model remains the same. Also, the area ratio of the aorta (the parent vessel) and the iliac vessels (the daughter vessels) are 0.97 (Hardy-Stashin, Meyer and Kauffman, 1980;

Greenwald, Carter and Berry, 1990) in all simulations, which means the iliac cross-sectional area is changed with the outlet area of the aorta to keep the ratio constant.

Table 5. 5. Parameters used in the aorta and iliac bifurcation model.

Segment Number	Arterial segment	Length (cm)	R _{in} (mm)	R _{out} (mm)	Peripheral resistance (10 ¹⁰ Pa s m ⁻³)	Peripheral compliance (10 ⁻¹⁰ m ³ Pa ⁻¹)
1	Ascending aorta	6	17.8	17.8	-	-
2	Aortic arch I	2	15.3	15.3	-	-
3	Aortic arch II	3.9	6.6	6.6	-	-
4	Aortic arch III	5.2	7.86	7.86	-	-
5	Brachiocephalic	3.4	7.8	7.8	0.06141	22.2
6	Left carotid	13.9	10	10	0.1366	2.821
7	Left subclavian	3.4	9.53	9.53	0.139	12.16
8	Descending Aorta II	24	12.60	12.60→8.44	-	-
9	Right common iliac	8.5	12	9.27→6.26	0.02644	31
10	Left common iliac	8.5	12	9.27→6.26	0.02644	31

5.3 RESULTS AND DISCUSSION

In this thesis, simplified arterial haemodynamic models are used to highlight wave reflection patterns and their corresponding time of arrival. The tapering was first defined with a stepwise reduction of the cross-sectional area, which was proposed in earlier studies (Bauer, Pasch and Wetterer, 1972; Hall, 1974; Pedley, 1980; Mynard and Smolich, 2014). Then, the results of each model are discussed respectively. Because different models are used, presenting the results and discussing each of the studies in parallel is a better approach.

5.3.1 REFLECTIONS IN THREE-STEP AREA REDUCTION

The pressure at the inlet of each segment is presented in Figure 5.6. The description of each pressure pulse is shown in Table 5.6. The negative sign behind the segment number stands for the reflection route in the backward direction.

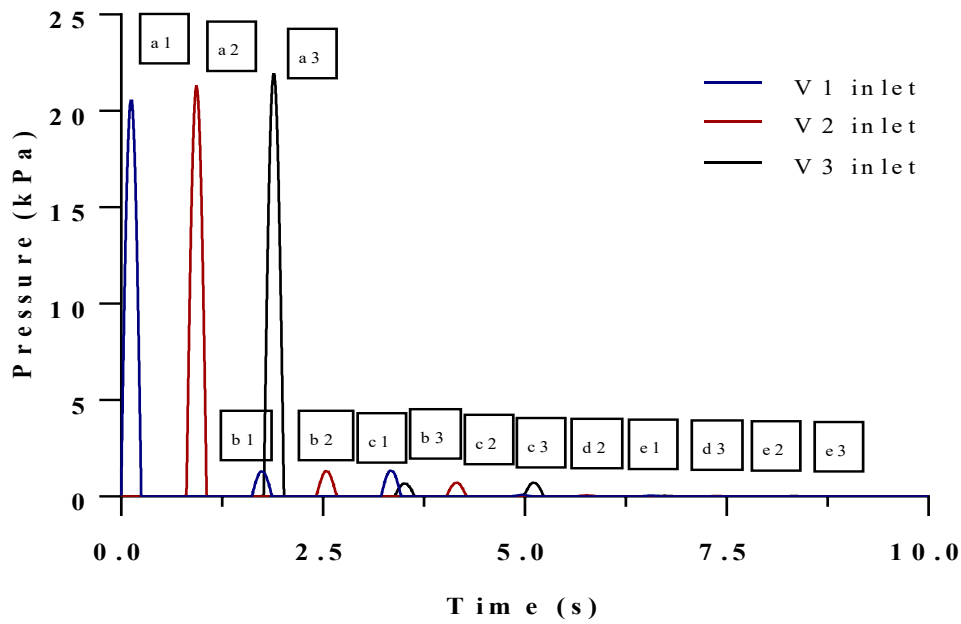


Figure 5. 6. The pressure in the inlet of the first (blue), second (red), and third (green) segments in the three stepwise model.

As the pulse travels across each junction with decreasing cross-sectional area, the pressure increases (waves a1, a2, and a3). In addition, a reflection travelling back to the inlet is generated at each junction and (waves b1, b2). After the first junction, the reflections are re-reflected (wave d1), and the amplitude of the wave reduces. In some cases, reflections overlap each other and emerge as one reflection (wave b2). Other than the waves mentioned above, many other reflections appear in the pressure. However, it is not feasible to allocate their origin since they may be a reflection of a re-reflected wave or an amalgamation of two or more re-reflections.

These results, although obtained from a simplified model with non-physiological dimensions, show the difficulties of resolving the ongoing debate of localizing the origin of the reflections.

The PWV_{MK} of each segment was calculated at the inlet and compared with the PWV_{ff} in Table 5.7. The values reported in Table 5.7 were used for the calculation of the arrival time of reflections in each segment. The local pulse wave velocity could estimate the time of arrival of reflections correctly, and similar to results of the simulations.

Table 5. 6. Description of each pressure wave appearing in the simulation of three-step area reduction model

Wave	Path	Time (s)	
		Simulation	Theoretical
a1	Input	0	0
a2	1	0.808	0.81
b1	1, -1	1.615	1.62
a3	1, 2, 3	1.762	1.767
b2	1, 2, -2	2.405	2.409
c1	1, 2, -2, -1	3.214	3.219
b3	1, 2, -2, 2, 3	3.372	3.367
c2	1, 2, -2, -1, 1	4.026	4.029
d1	1, 2, -2, 2, -2, -1	4.835	4.819
c3	1, 2, -2, -1, 1, 2, 3	4.978	4.987
d2	1, 2, -2, 2, -2, -1, 1	5.633	5.629
e1	1, 2, -2, 2, -2, 2, -2, -1	6.438	6.418
d3	1, 2, -2, 2, -2, -1, 1, 2, 3	6.614	6.581
e2	1, 2, -2, 2, -2, 2, -2, -1, 1	7.266	7.228
e3	1, 2, -2, 2, -2, 2, -2, -1, 1, 2, 3	8.204	8.186

Since the reflections that aroused from tapering are closely dependent on the local mechanical properties of the arterial wall, applying the foot-to-foot method is not convenient for locating their origin.

Table 5. 7. A comparison of the local pulse wave velocity (PWV_{MK}) at the inlet of each segment using the Moens-Korteweg equation their mean value (PWV_{mean}) and the regional pulse wave velocity using the foot-to-foot method (PWV_{ff}).

$PWV1_{MK}$	$PWV2_{MK}$	$PWV3_{MK}$	PWV_{mean}	PWV_{ff}
6.172 (m/s)	6.252 (m/s)	6.332 (m/s)	6.252 (m/s)	6.253 (m/s)

While in previous studies (Bauer, Pasch and Wetterer, 1972; Pedley, 1980; Reuderink, Sipkema and Westerhof, 1988; Mynard and Smolich, 2014) the frequency-domain was used for the analysis of the stepwise taper, using a time-domain based analysis gave us the ability to estimate the axial distance of the reflections as shown in Table 5.6. Figure 5.7 shows the method of calculation of the time and location of each reflection and the pattern of their generation.

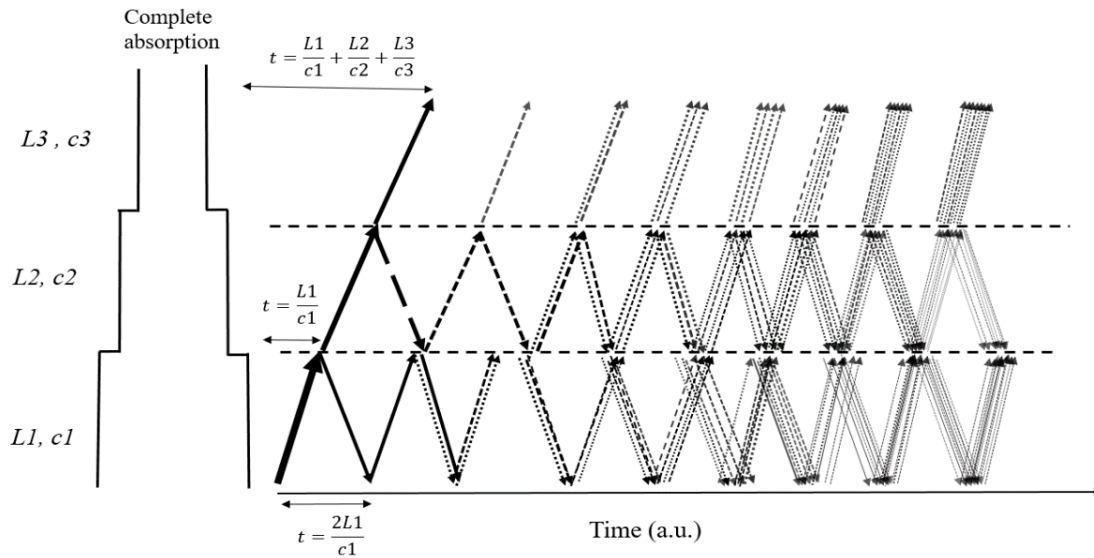


Figure 5. 7. A schematic representation of stepwise tapering consisting of three segments and emerged reflections pattern. The length of all the segments $L1$, $L2$, and $L3$ are 5 metres. $c1$, $c2$ and $c3$ denote for wave speed in the respective segments.

5.3.2 REFLECTIONS IN STEPWISE DIAMETER REDUCTION AND CONTINUOUSLY TAPERED VESSEL

A systematic comparison concerning different methods of implementing tapering in 1D, such as continuous taper or stepwise reduction, and a straight segment was performed. The pressure waves at the inlet (A) and after 1.5 metres (B) are shown in Figure 5.8. The inlet area and flow were kept constant in all simulations, which should generate the same input flow. Nevertheless, the continuous tapered structure presents a higher peak pressure compared to the other structures (Figure 5.8A).

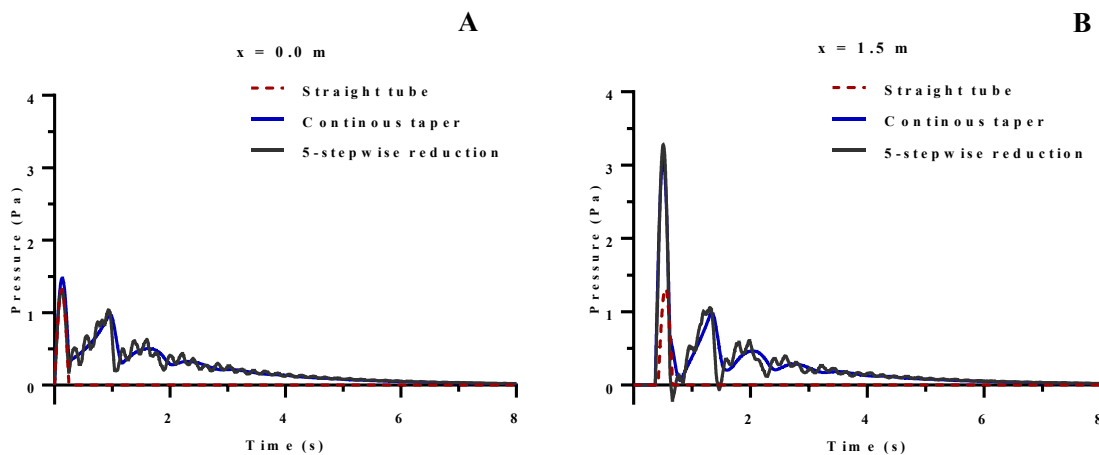


Figure 5. 8. The pressure in the inlet (A) and the outlet (B) of a continuous tapered, 5-step diameter reduction, 4-step diameter reduction and a straight vessel.

The increase in input pressure is due to the increase of impedance in the first segment, which is in agreement with the findings of (Segers and Verdonck, 2000). Besides, the continuous taper causes a smooth increase of reflections travelling to the inlet while the stepwise reductions cause sudden oscillations (Figure 5.8A). As the number of stepwise segments increases, the pressure fluctuation decreases and the amplitude is closer to the continuous taper. While the pressure amplitude in a straight vessel remains unchanged, there is a 3-folded increase in pressure for the tapered structures.

In contrast to the inlet, the pressure at the outlet (Figure 5.8B) is higher when the tapering is defined as stepwise reduction. This shows how tapering can smoothen the pressure wave as the cross-sectional area is reduced. This result is in agreement with that found by (Mynard and Smolich, 2014), studying the effect of tapering on reflections and the smooth pressure decay in diastole.

In Figure 5.9, wave intensity analysis is performed at the inlet of all the structures. In a straight vessel, first, there is FCW which is caused by the first part of a half-sinusoidal wave, where $dP > 0$. Following the FCW, there is a FEW caused by the second part of half-sinusoid ($dP < 0$). Since there is complete absorption at the outlet, no reflected wave is generated in the straight vessel. The same trend can be seen in all structures in the first 0.25 second of the wave. While in a continuous taper as the wave reaches the outlet of the vessel, the change in the cross-sectional area causes a reflected wave travelling backwards (at $t = 1.08$ s). The inflow boundary condition is reflective. Hence, an immediate forward wave is seen at the same timing.

By comparing the WIA for 4-step and 5-step reduction of diameter in the vessel, there are two significant observations: 1) the intensity of reflected waves in the 5-step reduction of diameter is smaller compared to the 4-step reduction. 2) the time of arrival of the first reflection in the 5-step reduction of diameter is earlier. Both of these observations are expected because: 1) the steps are smaller in the 5-step reduction of diameter, and the generated reflection is smaller consequently. 2) both structures have identical wave speed at the inlet; the length of the segments in the 5-stepwise reduction of diameter is shorter compared to 4-step reduction; thus, the reflection arrives earlier. In addition, the BCW in the 5-step diameter reduction model is not symmetrical with FCW due to the interruption of the reflected wave arriving earlier.

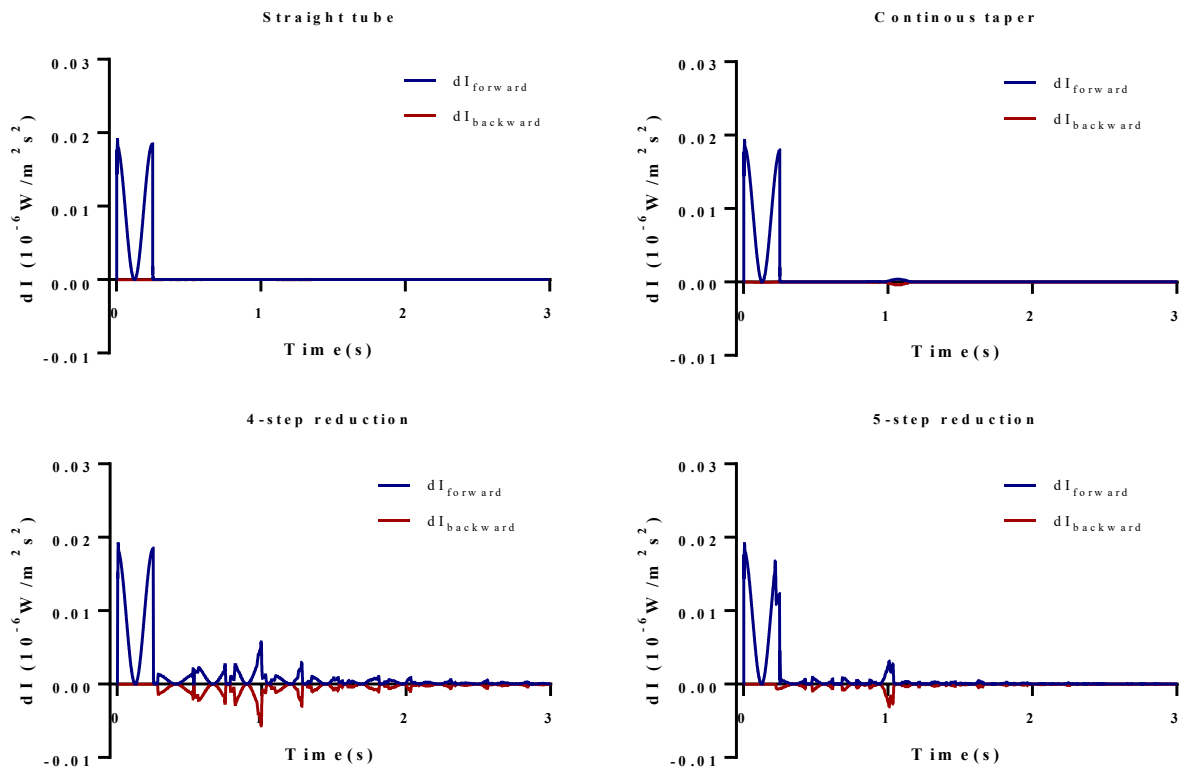


Figure 5. 9. Wave intensity analysis in a straight vessel, a continuously tapered vessel, 4-step reduction of diameter, and 5-step reduction of diameter.

5.3.3 A COMBINATION OF STEPWISE STRUCTURE AND BIFURCATION

A comparison is conducted between stepwise structures when the segments are 5-metres in length and when the length of the segments are reduced to, first 0.312 metres, and then 0.078 metres. Figure 5.10 shows the computed pressure at the inlet of all the structures. Each junction, which is an imitation of the effect of tapering, causes a reflected wave to travel towards the inlet. A higher reflection is generated as the flow perturbation reaches the bifurcation, and the staggered arrangement of the daughter vessels creates a fluctuation in the reflections originated from the bifurcation.

All three models have the same inlet area. Therefore, the flow should produce the same pressure amplitude at their inlets. However, Figure 5.10 shows a higher pressure in Experiment 3 compared to the other simulations. This difference indicates that since the reflections do not have enough axial distance to emerge separately, they overlap each other and cause an increase in input impedance and, as a consequence, the pressure amplitude elevates. The reflections from the reduction of diameter are manifested as constant pressure, while the reflection from the bifurcation causes a peak in pressure. The staggered definition of the daughter vessels caused a higher amplitude for the peak pressure, but the corresponding ripple effect, which is

evident in Experiment 1 disappears in Experiment 3. The results of this study show the location and the time of occurrence of the reflections in long vessels. The length reduction adds complexity to the allocation of the origin of each reflection, which is also reported in (Segers and Verdonck, 2000),(Mynard and Smolich, 2014). Therefore, WIA is used at the inlet of each structure to study the reflections and their occurrence time (Figure 5.10 bottom).

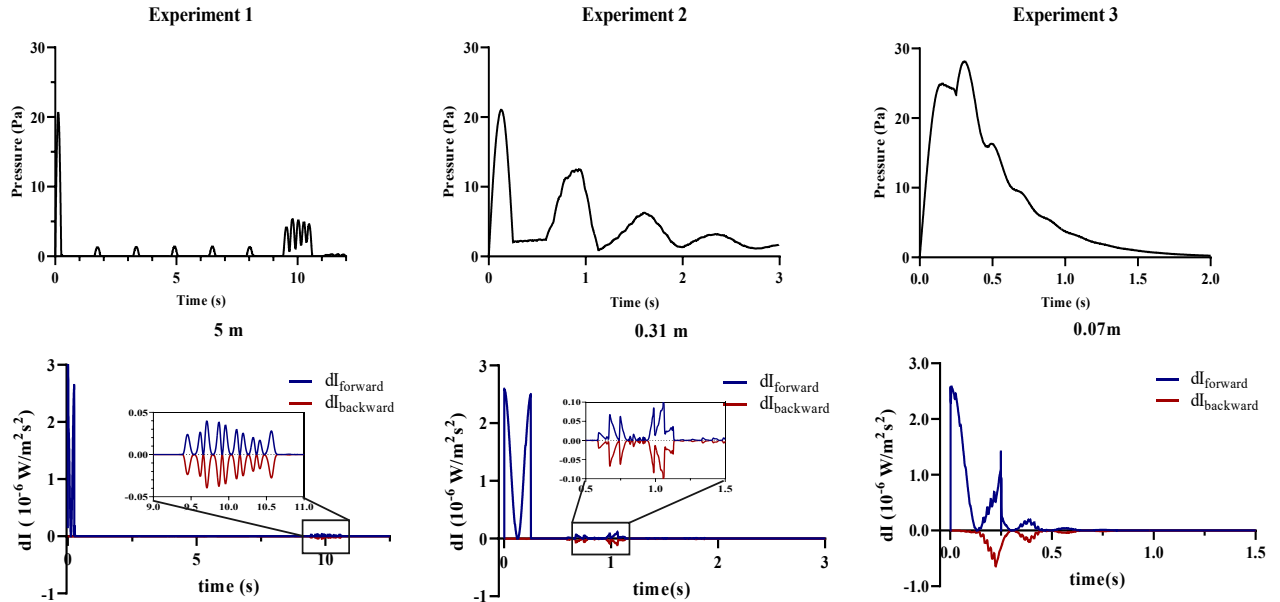


Figure 5. 10. The pressure (top) and wave intensity analysis (bottom) at the inlet of a stepwise structure with segments 5 metres long (Experiment 1), 0.312 metres (Experiment 2), and 0.078 metres (Experiment 3). All the structures have the same mechanical properties except the axial length of its consisting segments. The structure ends with a bifurcation, where the daughter vessel diameter is reduced in the same manner.

Experiment 1 shows that only the reflections originating from the tapered bifurcation are detectable at the inlet. The same phenomenon is seen in Experiment 2. However, the occurrence time of reflection reaching to the inlet is decreased. Finally, Experiment 3 shows the amalgamation of the reflection, which is increasing the amplitude of backward wave intensity. It can be noticed that the FEW is decreasing when the reflection (BCW) is emerging, and it is not symmetrical with FCW.

5.3.4 TAPERING IN THE UPPER THORACIC AORTA

With an increase in the tapering angle, and constant wall thickness, the PWV_{MK} increases at each cross-section. The difference in the PWV_{ftf} is 1 m/s from no taper to the highest tapering angle. The angles and the corresponding PWV_{MK} in the inlet and outlet, as well as mean and foot-to-foot PWV, is presented in Table 5.8.

Table 5. 8. Different tapering angles in thoracic aorta and the value pulse wave velocity in the inlet, outlet, mean, and the foot-to-foot method.

Tapering angle $\Theta(^{\circ})$	PWV _{MK, inlet} (m/s)	PWV _{MK, outlet} (m/s)	PWV _{mean} (m/s)	PWV _{ff} (m/s)
1.375	5.016	6.974	5.995	6.352
1.250	5.016	6.696	5.856	6.351
1.125	5.016	6.448	5.732	6.034
0.875	5.016	6.026	5.520	6.032
0.750	5.016	5.844	5.429	5.746
0.625	5.016	5.677	5.346	5.485
0.375	5.016	5.382	5.199	5.247
0.00	5.016	5.015	5.015	5.028

Also, the changes in diameter and area of the inlet and outlet of the upper thoracic aorta in each simulation with different tapering angle are provided in Table 5.9. The values reported here are rounded with 0.001 degrees of accuracy.

The pressure and pulse pressure change have more evident differences, as shown in Figure 5.11. The peak pressure in the inlet of the thoracic aorta changes 5.72 kPa from 0° to 0.87°.

Table 5. 9. The changes in the angle of tapering and the outlet diameter in the upper thoracic model.

Simulation	Tapering angle (degree)	$\tan(\theta)$	D _{in} (cm)	D _{out} (cm)	A _{in} (cm ²)	A _{out} (cm ²)
1	1.500	0.026	2.400	1.136	4.524	1.013
2	1.375	0.024	2.400	1.241	4.524	1.21
3	1.250	0.022	2.400	1.347	4.524	1.424
4	1.125	0.02	2.400	1.452	4.524	1.656
5	1.000	0.017	2.400	1.557	4.524	1.905
6	0.875	0.015	2.400	1.663	4.524	2.171
7	0.750	0.013	2.400	1.768	4.524	2.455
8	0.625	0.011	2.400	1.873	4.524	2.756
9	0.500	0.009	2.400	1.979	4.524	3.075
10	0.375	0.007	2.400	2.084	4.524	3.411
11	0.250	0.004	2.400	2.189	4.524	3.765
12	0.000	0.000	2.400	2.400	4.524	4.524

The increase in mean pressure can be explained by the increase of arterial resistance in the thoracic aorta, which is in agreement with the results of (Redheuil *et al.*, 2011; Martin *et al.*, 2013). In addition, the higher pulse pressure is reported in ageing population following the drop

of diastolic pressure which is also can be seen in Figure 5.11 (O'Rourke and Nichols, 2005; Martin *et al.*, 2013)

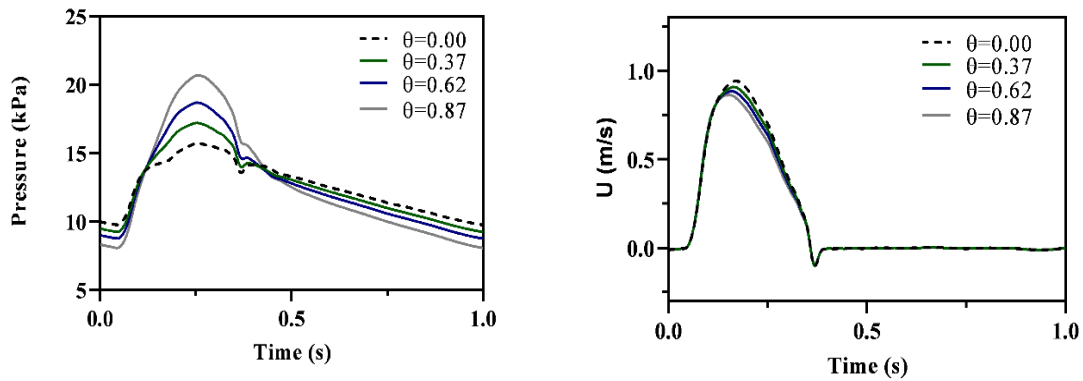


Figure 5. 11. The measured pressure and velocity at the inlet of the thoracic vessel in different angles of tapering.

Furthermore, lower arterial compliance causes higher peak pressure in the aorta since the damping ability of the arterial wall is lower (Caro *et al.*, 2011). Linear separation of the pressure at the inlet of the aorta with different angles is shown in Figure 5.12.

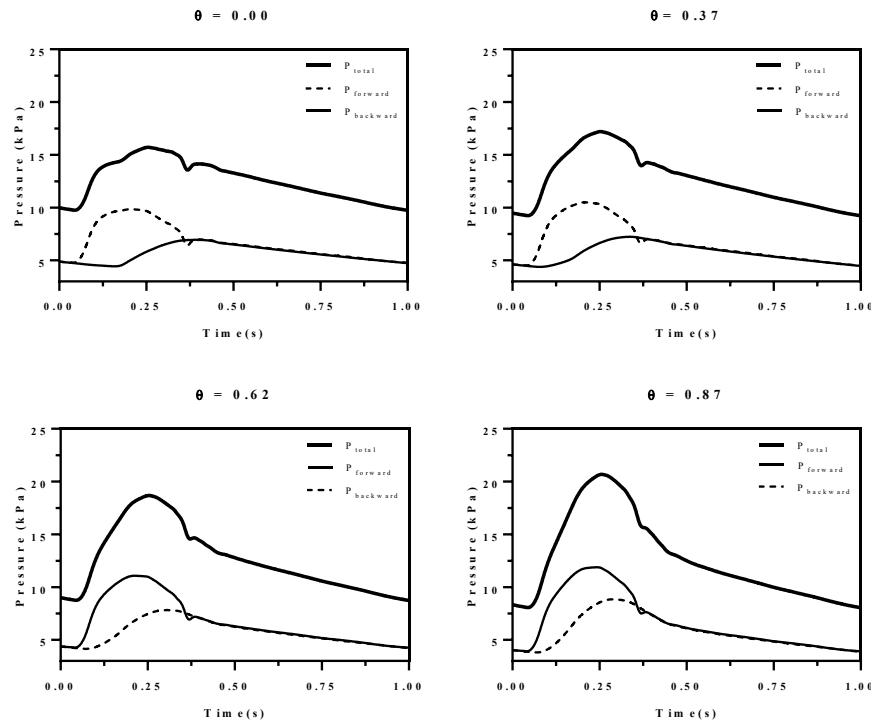


Figure 5. 12. Forward and backward components of the pressure measured at the inlet of the upper thoracic aorta in different tapering angles.

The arrival time of the backward travelling pressure (P_b) reduces as the difference in the inlet and outlet diameter increases, while the amplitude of both forward (P_f) and backward travelling pressure elevates.

The arterial compliance and resistance, computed using Equation (5.3) and (5.4) respectively, are presented in Figure 5.13. According to (O'Rourke and Hashimoto, 2007), the age-associated increase in systolic blood pressure is due to the diminution of arterial compliance. The outcomes of this study show that with a higher angle of tapering, arterial compliance decreases regardless of the value of Young's modulus. Consequently, the amplitude of systolic pressure rise with changes in diameters, which is in agreement with the results of clinical studies (Mitchell, 2008).

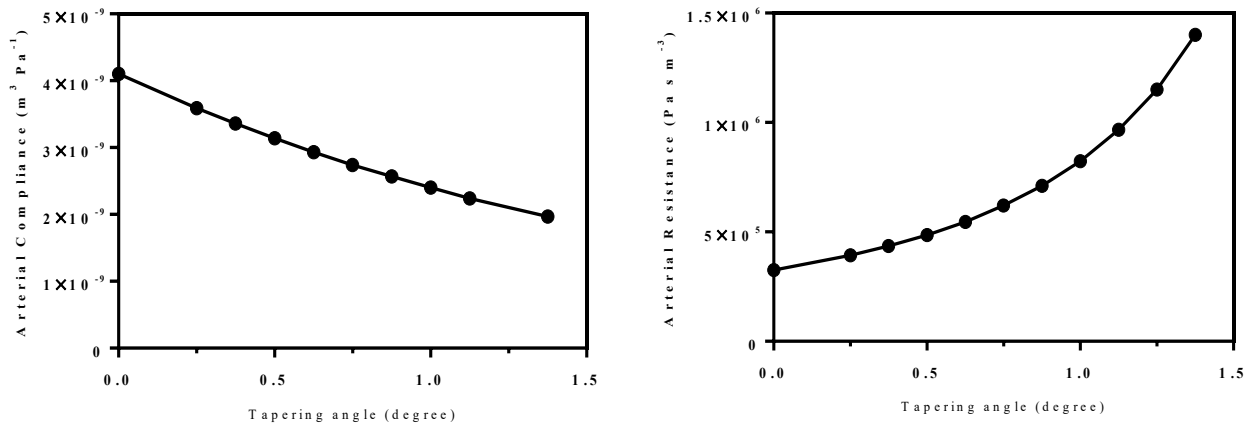


Figure 5. 13. The arterial compliance (left) and resistance (right) changes with increased tapering angles.

Finally, WIA is used to study the reflections at the inlet of the thoracic aorta. A straight vessel causes a backward reflection due to the terminal resistance. As the cross-sectional area of the outlet becomes narrower, the amplitude of backward wave intensity increases. This surge is also evident in the forward wave intensity, which is anticipated because of the alteration in the arterial compliance and resistance.

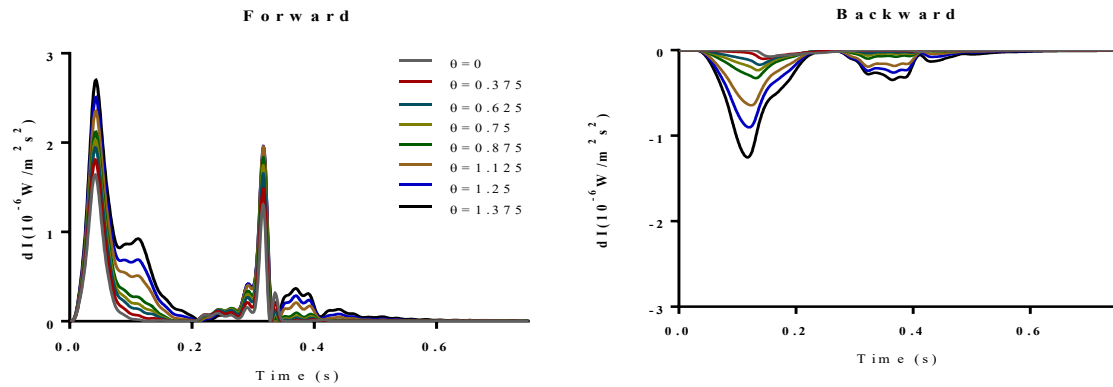


Figure 5. 14. Wave intensity analysis at the inlet of the thoracic aorta with different tapering angles.

While tapering causes an evident difference in the pressure at the inlet of the thoracic aorta, there is negligible difference in the time of arrival of the backward waves (Figure 5.14).

The small variance of PWW_{ff} with tapering might explain the reason behind the time difference, which causes the reflected waves to arrive at the inlet at approximately the same time. In this model, the wall thickness and Young's modulus are considered to be constant throughout the vessel. However, according to (O'Rourke, Farnsworth and O'Rourke, 2008), the arterial wall becomes thinner towards the periphery.

5.3.5 TAPERING IN THE DESCENDING AORTA AND ILIAC BIFURCATION

The changes in diameter value had the same trend as the upper thoracic aorta model. A higher value of mean pressure, pulse pressure and systolic pressure is observed with an increase of tapering angle (Figure 5.15).

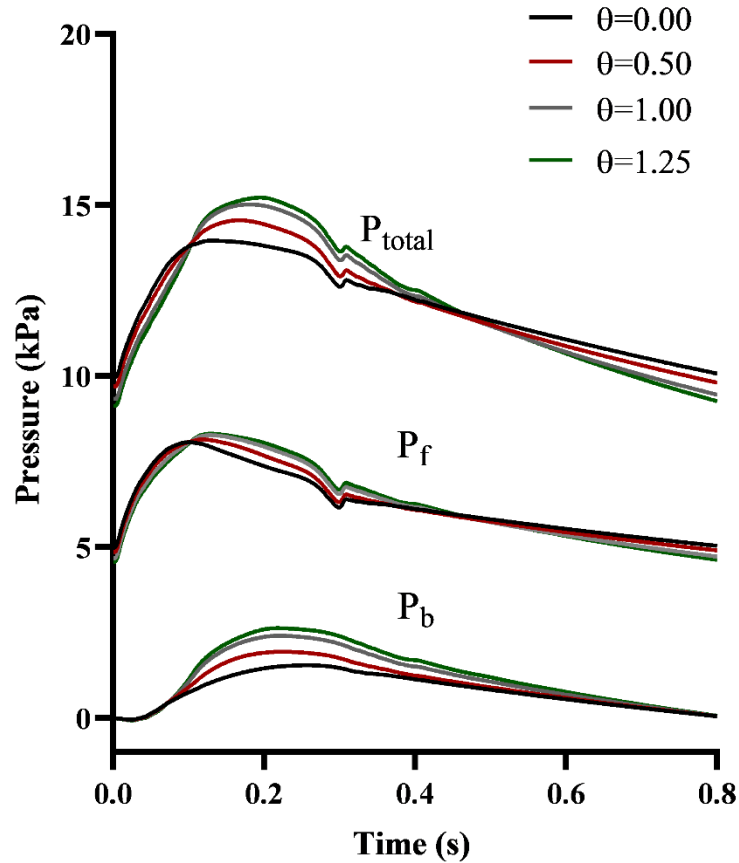


Figure 5. 15. Pressure waveforms measured at the ascending aorta in the model of the aorta and iliac bifurcation.

The forward and backward components of the pressure measured at the inlet are shown in Figure 5.15. The increase in both forward and backward components of the pressure is noticeable in this model. Nevertheless, the changes in the forward direction are lower compared to the backward component.

Figure 5.16 shows wave intensity in the aorta when connected to the iliac bifurcation. Forward compression wave's amplitude has a small increase due to the constant properties of measurement location in all tapering angles. The BCW is growing in amplitude, and there is a gradual backward shift in time, which shows the early arrival of the reflections. The area ratio of the bifurcation is 0.97 in all the angles. Therefore, the reflection caused by bifurcation is kept constant, and the changes can be related solely to the effect of tapering. However, according to (Greenwald, Carter and Berry, 1990), the area ratio in iliac bifurcation decreases with ageing because the parent vessel cross-sectional area expands while the cross-sectional area of the iliac vessel stays the same. In (Mynard and Valen-Sendstad, 2015), the pressure at the junctions are calculated, and they reported a higher accuracy of the simulations. Therefore,

consideration of pressure losses at each junction is recommended in future studies to enhance the results.

Also, reflections originating from the side branches of descending aorta are neglected in this study, which can limit the accuracy of this model.

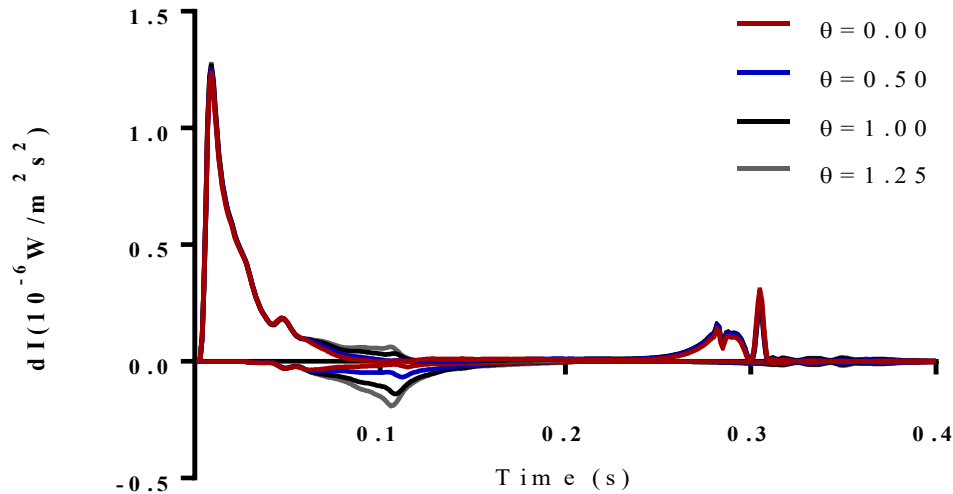


Figure 5. 16. Wave intensity analysis at the ascending aorta. The model consists of the aorta connected to the iliac bifurcation. The tapering angle is changing in the descending aorta.

According to (O'Rourke and Nichols, 2005; Hickson *et al.*, 2010; Martin *et al.*, 2013), pulse pressure and aortic impedance increase with stiffening of the vessel wall. In the simulations, the same influence is noted on pulse pressure and aortic impedance with increasing the angle of tapering. On the other hand, the changes in the arterial tree caused by ageing affect the proximal aorta more than its distal parts. Reference (Charlton *et al.*, 2019) reported no changes in the length of distal sections of the aorta and carotid and iliac arteries with ageing. In the ascending aorta both the length and width increases, while in descending aorta only the diameter changes. This phenomenon means that in the descending aorta, the angle of tapering increases with age.

Moreover, the results show a decrease in arterial compliance as the tapering angle increase. Decrease of vascular compliance with ageing has been reported in clinical investigations (Chemla *et al.*, 1998; López-Beltrán *et al.*, 1998; Resnick *et al.*, 2000).

The average values reported in (Hickson *et al.*, 2010) for length and diameter for different age groups are used in this study. The result can be seen in Figure 5.17. Findings of this study are in agreement with the clinical values measured from 162 healthy subjects aged 18 to 77 years. Moreover, results provide a range of tapering angle for each decade of age group. Only the values reported for the descending aorta is used in this study.

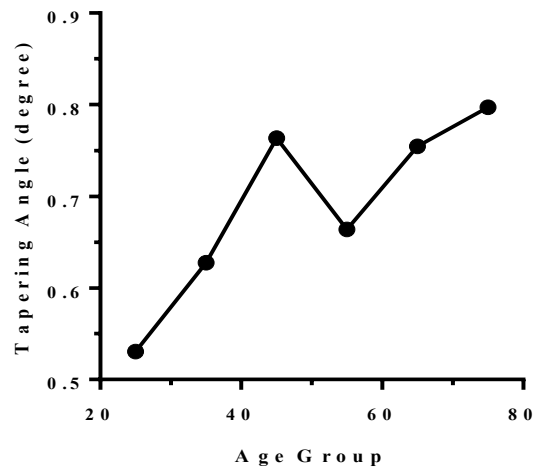


Figure 5. 17. The reported variation of tapering angle in descending aorta with ageing in Hickson *et al.* (2010)

The results show an increase in tapering angle in each age decade, except in 50-60. This exception appears to be an outlier due to the noise of the data.

It is known that ageing causes properties such as arterial wall thickness, elasticity and the wall layers to change (O'Rourke and Hashimoto, 2007; Caro *et al.*, 2011). It is reported that the elastic changes are smaller than geometrical changes in the arterial wall and can be neglected (Wemple and Mockros, 1972).

5.4 LIMITATIONS

In all the current simulations, Young's modulus is considered to be constant in each vessel and tapering angle. This consideration enables the opportunity to focus on the alteration of diameter through aorta only. The changes of the cross-sectional area are affecting the stiffness of each segment, by β , which is calculated using Equation 2.27, causing the tapering to affect the stiffness without changing Young's modulus. Consideration of changes in elasticity can provide a more precise understanding of an ageing arterial wall.

In addition, the prescribed input boundary condition is constant even in cases that the tapered vessel becomes narrower. The similar inflow disregards the changes of the left ventricle with age and its response to changes in the proximal artery. Based on findings of (Redheuil *et al.*, 2011; Kim *et al.*, 2017) left ventricle increases in mass and the walls changes (concentric remodelling), hence, changing the inflow boundary condition or the coupled model of the heart with each tapering angle can improve the results of this work.

Another limitation of this work is using the linear wave separation technique for examining the effect of tapering. Because tapering introduces additional nonlinearity into the system and

as a consequence assumption on linearity can cause more substantial errors in the results, especially in steeply tapered vessels (Mynard *et al.*, 2012). Therefore, nonlinear analysis of the waves might provide a further understanding of the matter.

It is worth mentioning that the mathematical theories consider vessels as uniform circular vessels where the cross-sectional area and distensibility vary continuously. Though, real blood vessels are of variable cross-sections and curved. Using the 1D model might be a crude heuristic method for the analysis of tapering since it neglects any flow movement in other directions. Nevertheless, a comparison study between 1D and 3D model was conducted (Xiao, Alastruey and Figueroa, 2014), and the predictions of both simulations were in good agreement.

5.5 CONCLUSION

To conclude, it is possible to show clear and discrete reflection sites in long segments (5 metres). However, as the wave continues to travel, the reflections and re-reflections amalgamation cascades, limiting the ability to find the reflection sites. For segments with physiological lengths, the overlapping of the reflections causes an increase of pressure at the inlet of the computational models. Tapering not only causes a continuous reflection in the arterial structure but also increases the impedance of the system, which augments both peak and pulse pressures.

Additionally, the pressure variation throughout the segment is smoother in vessels with continuous tapered compared with stepwise changes in vessel area.

Increasing the tapering angle, as it can be seen in the ageing descending aorta, is associated with an increase in the peak pressure due to the increase of the segment resistance, and an increase in pulse pressure due to the decrease in arterial compliance. Also, increasing the tapering angle caused an increase in the magnitude of both the forward and backward wave intensity.

Prospectively, a study of a larger number of arterial tree segments than used in the current study with different tapering angles will provide more accurate information on the values of reflections with ageing, which will be discussed in Chapter 6. The effect of changes in Young's modulus, arterial wall thickness, nonlinearity and left ventricle concentric remodelling with tapering and ageing should also be included in the future studies.

IMPACT OF TAPERING IN THE ARTERIAL TREE

6.1. INTRODUCTION

Arterial wave reflection and their influence on the contour of the pressure in the aorta has been the focus of many studies. Any alteration in mechanical properties of arterial structure can cause a wave travelling to reverse direction, which can be entrances, branches and even obstructions, therefore keeping track of the reflections can become hopelessly complicated (STREETER, KEITZER and BOHR, 1963). Some researchers focused on finding the origin of the reflections (Burattini and Campbell, 1989; Segers and Verdonck, 2000; Segers, Ernst R Rietzschel, *et al.*, 2007; Westerhof *et al.*, 2008) and some have looked for markers linking the pathologies to amplitude or timing of reflections (Stergiopoulos *et al.*, 1996; Mitchell *et al.*, 2004, 2014; Swillens *et al.*, 2008; Murakami, 2017; Quail *et al.*, 2017). Although it is more than half a century that the concept of reflection was introduced, there are many debates about the allocation of the origin of reflections (Segers *et al.*, 2017).

In chapter 5, the effect of tapering and the tapering angle was studied using different models. In one of the physiological models, simulating the upper thoracic aorta connected to the iliac bifurcation, with compromising the side branches in the abdominal region, it is noticed that with no tapering the pulse pressure and peak pressure are lower.

On the other hand, in Chapter 4, the path of reflection wave travelling towards the aortic root was investigated in a computational tapered arterial tree model. Results showed that only 1 % of the reflection starting from the anterior tibial reaches the ascending aorta. The reason behind of significant reduction of amplitude lies in the multi-branching and tapered structure of the conduit vessels of the arterial tree. A palpable reduction of reflections at the iliac bifurcation is observed, which agrees with literature. Also, the outcome shows that the reduction of waves amplitude when travelling towards the root is higher than in the opposite direction.

Segers and Verdonck (2000) used an elastic arterial replica of large conduit arteries to study the pattern of reflection waves in the aorta and compared the in vitro results with the computational estimations. Their main aim was to examine the effect of tapering on the

reflections. After separation of pressure to its incident and reflected components, they observed continuous reflections in different locations of the replica. Furthermore, they concluded that the reflection present in in vivo measurement of the aorta is an interaction between the small reflection arising from tapering and reflections originating at the level of the diaphragm.

Later, the same observation was made in vivo (Davies *et al.*, 2012), where pressure and velocity measured in 10 cm distances along the aorta showed no significant changes in arrival time of the reflected waves. They hypothesized that the re-reflections of the waves cause an entrapment along the way and prevents the distal waves from being sensed at the proximal aorta.

In complicated branched network, such as the arterial tree, the reflected waves are resultant from many sites, thus, to avoid the complications of previous studies, the complexity of the system is reduced in this study. The design of this computational experiment is constructed based on the results of the previous chapters, by only focusing on the influence of tapered arterial tree with 55 segments and, similar to chapter 4, there is no heart at the inlet of the ascending aorta. Since imposing these conditions are impossible to accomplish in animals or the human, we performed this analysis using 1D modelling of blood flow in the arterial.

6.2. METHODS

The 55-segment arterial tree used in this chapter is derived from anatomically detailed arterial models developed by Blanco *et al.* (Blanco *et al.*, 2015). The model consists of 61 arterial segments, consisting of the largest 55 vessels of the human arterial system. This model is validated (Reymond *et al.*, 2009) and has been used in several studies (Alastruey *et al.*, 2008; Davies *et al.*, 2012; Willemet and Alastruey, 2014; Boileau *et al.*, 2015; Epstein *et al.*, 2015). The pulse wave propagation is compared in the tapered structure versus a non-tapered one. As mentioned before in this study, the focus is *only* on the role of tapering in the amplitude reduction of reflected waves travelling back towards the aortic root. For this goal to be achieved, the results of tapered and non-tapered models are compared. However, this comparison requires keeping the reflections coefficient at the respective bifurcations of both models similar.

In order to construct the non-tapered model, we use the dimensions used in (Boileau *et al.*, 2015) with similar terminal boundary conditions consisting of the three-element Wk model. The non-tapered arterial tree is designed based on the following steps: 1) an average of the cross-sectional diameter at inlet and outlet of each arterial vessel is calculated and used as the

constant diameter of the vessel without the tapering. 2) The reflection coefficient and the area ratio of the daughter to mother vessels at each bifurcation in the tapered model is calculated, and it is applied to area ratios in the non-tapered model. Table 6.1 presents the dimensions of the segments and the peripheral resistance and compliance values, in tapered and non-tapered arterial tree models. All values are rounded by three decimal points.

Vessels are modelled as thin, incompressible, elastic and homogeneous segments. The blood is considered to be homogenous, incompressible and Newtonian fluid with $\rho = 1050 \text{ kg/m}^3$ and $\nu = 4 \text{ mPa s}$.

The Young's modulus is constant throughout the arterial tree ($E = 225 \text{ kPa}$), and the wall thickness is calculated by an empirical equation (Blanco *et al.*, 2015).

$$h = R_0 [\acute{a} \exp(\acute{b} R_0) + \acute{c} \exp(\acute{d} R_0)], \quad (6.1)$$

where R_0 is the initial radius (related to A_0), and $\acute{a} = 0.2802$, $\acute{b} = -5.0531 \text{ cm}^{-1}$, $\acute{c} = 0.1324$ and $\acute{d} = -0.1114 \text{ cm}^{-1}$.

The same equation is used for the non-tapered segments, which means the R_0 is constant along the segment. The initial condition for area and velocity are $(A(x, 0), U(x, 0)) = (A_0(x), 0)$. The wave speed for each segment is calculated using the Equation 2.32.

Generating a pulse from the end of the *profunda femoris* vessel can cause confusion in the understanding the previously defined notions about the waves. For example, usually, a backward wave corresponds to a reflected wave travelling towards the heart, or an incident wave is the wave generated from the left ventricle and travels in the forward direction.

While in this study, a wave is travelling towards the heart without being a reflection from an incident wave. Hence, there is a necessity to set regulation for interpretation of the results. Any wave travelling from distal locations towards the aortic root is travelling in the backward direction, and any wave which is travelling from the aortic root to the distal locations is travelling in the forward direction. These waves can be either generated as an inflow or be a result of reflection.

6.2.1 FORWARD DIRECTION

First, the tapered and non-tapered systems are simulated with a flow rate extracted from the physiological flow reported (Murgo *et al.*, 1980). The shape is defined as a function of harmonics and then the function is defined as the input for the arterial network. The terminal boundary condition, which is 3-element Wk model, is presented in Table 6, and the schematic representation of the model and the inflow is presented in Figure 6.1(No.1).

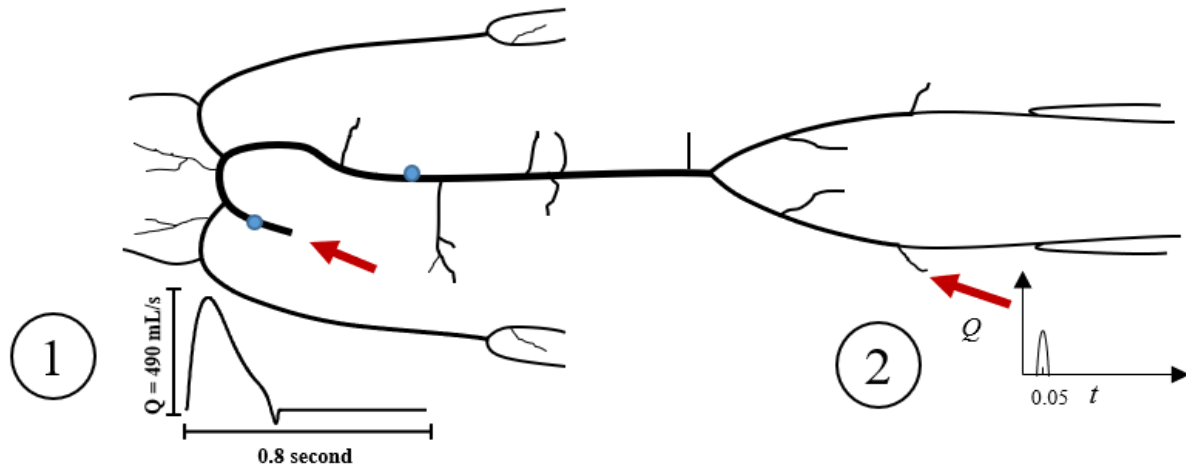


Figure 6. 1. The schematic representation of the arterial model and the induced inflow. Blue solid circles indicate the measurement sites. The first Red arrow indicates the direction of the wave in the forward direction and the second red arrow shows the direction of the wave in the backward used in the second simulation.

6.2.2 BACKWARD DIRECTION

Similar to Chapter 4, the boundary condition at the aortic root is simulated as an absorber and then as a complete reflector. A semi Gaussian-shaped pulse is induced as the inflow to the system from the left *profunda femoris* artery or segment 71 in Table 6.1, causing an initial pressure wave with an amplitude of 10 mmHg in both models. The equation for the induced flow pulse is as below

$$Q(t) = 3.33 * 10^{-5} \exp(-10000(t - 0.05)^2) \text{ m}^3/\text{s}. \quad (6.2)$$

The schematic representation of the model is presented in Figure 6.1. It shows the location of insertion of inflow and the locations where the pressure and velocity were estimated in the backward direction (No.2). The terminal boundary condition for rest of the arterial network, except the *left profunda femoris* artery, is similar to the values reported in Table 6.1.

In Table 6.1, some segments are connected to each other, either in the form of a simple junction or a bifurcation. Hence those segments are not terminal vessels and do not have the terminal resistance and compliance. The terminal resistance and compliance represent the resistance and compliance of the capillary bed. For example, segment 1, which is aortic arch I, is connected to the brachiocephalic trunk and aortic arch II. Therefore, there is no terminal boundary condition for it. On the contrary, since the model is limited to the common carotid artery (CCA) (i.e. its bifurcations are not modelled as segments), the response of the daughters of the CCA are modelled as terminal resistance and compliance.

Table 6. 1. Diameter values in the tapered and non-tapered arterial model. Column four consists of the radius of the tapered segments at the inlet and outlet, and column five is the radius used for the non-tapered arterial tree. In the backward direction simulations, segment 71 is changed to a source of a pulse, and it is highlighted with grey.

Number	Arterial Vessel	Length (cm)	Tapered Radius (cm)	Non-tapered Radius (cm)	Peripheral resistance $R_t(R_1)$ (10^{10} Pa s m ⁻³)	Peripheral Compliance (10^{-10} m ³ Pa ⁻¹)
1	aortic arch I	7.44	1.595→1.295	1.203	-	-
2	brachiocephalic trunk	4.73	0.673→0.616	0.543	-	-
3	aortic arch II	0.96	1.295 → 1.257	1.203	-	-
4	Subclavian R I	1.57	0.490→0.418	0.431	-	-
5	Common carotid R	8.12	0.448 →0.333	0.421	0.905 (0.181)	0.313
6	Vertebral R	20.44	0.134→0.134	1.335	-	-
7	Subclavian R II	4.112	0.418 →0.230	0.431	-	-
8	Axillary R	12.000	0.230→0.208	0.431	-	-
9	Brachial R	22.311	0.208 → 0.183	0.431	-	-
10	Radial R	30.089	0.138 → 0.138	0.431	0.577 (0.115)	0.491
11	Ulnar R I	2.976	0.141 → 0.141	0.431	-	-
12	Common interosseous R	1.627	0.096 → 0.096	0.023	-	-
13	Ulnar R II	23.926	0.141 → 0.141	0.338	0.587 (0.117)	0.482
14	Posterior interosseous R	23.056	0.068 → 0.068	0.676	2.391 (0.478)	0.118
15	External carotid R	6.090	0.227 → 0.227	0.287	0.469 (0.094)	0.603
16	Internal carotid R	13.211	0.277 → 0.277	0.351	0.288 (0.058)	0.983
17	Common carotid L	12.132	0.448 →0.333	0.421	-	-
18	Aortic arch III	0.698	1.257 →1.228	1.203	-	-
19	External carotid L	6.090	0.227 → 0.227	0.287	0.471 (0.094)	0.601
20	Internal carotid L	13.211	0.277 → 0.277	0.351	0.289 (0.058)	0.980
21	Subclavian L I	4.938	0.490 → 0.348	0.431	-	-
22	Aortic arch IV	4.306	1.228 → 1.055	1.203	-	-
23	Vertebral L	20.415	0.134 → 0.134	0.133	0.962 (0.192)	0.294
24	Subclavian L II	4.112	0.348 → 0.230	0.431	-	-
25	Axillary L	12.000	0.230 → 0.208	0.431	-	-
26	Brachial L	22.311	0.208 → 0.183	0.431	-	-
27	Radial L	31.088	0.138 → 0.138	0.431	0.567 (0.113)	0.499
28	Ulnar L I	2.976	0.141 → 0.141	0.431	-	-
29	Common interosseous L	1.627	0.096 → 0.096	0.431	-	-
30	Ulnar L II	23.926	0.141 → 0.141	0.338	0.599 (0.120)	0.473
31	Posterior interosseous L	23.056	0.068 → 0.068	0.067	2.399 (0.480)	0.118
32	Thoracic aorta I	0.990	1.055 → 1.036	1.203	-	-
33	Posterior intercostal R 1	19.688	0.141 → 0.141	0.140	12.460 (2.491)	0.023
34	Thoracic aorta II	0.788	1.036→1.022	1.203	-	-
35	Posterior intercostal L 1	17.803	0.140 → 0.140	0.140	12.780 (2.556)	0.022
36	Thoracic aorta III	1.556	1.022 → 0.992	1.203	-	-

6.2. Methods

37	Posterior intercostal R 2	20.156	0.155 → 0.155	0.155	11.620 (2.324)	0.024
38	Thoracic aorta IV	0.533	0.992 → 0.982	1.203	-	-
39	Posterior intercostal L 2	18.518	0.155 → 0.155	0.155	11.720 (2.344)	0.024
40	Thoracic aorta V	12.156	0.982 → 0.754	1.203	-	-
41	Thoracic aorta VI	0.325	0.754 → 0.749	1.203	-	-
42	Celiac trunk	1.682	0.335 → 0.321	0.537	-	-
43	Abdominal aorta I	1.399	0.749 → 0.732	1.203	-	-
44	Common hepatic	6.655	0.269 → 0.269	0.449	0.167 (0.034)	1.692
45	Splenic I	0.395	0.217 → 0.217	0.362	-	-
46	Left gastric	9.287	0.151 → 0.151	0.252	17.170 (3.434)	0.016
47	Splenic II	6.440	0.217 → 0.217	0.362	0.237 (0.047)	1.197
48	Superior mesenteric	21.640	0.393 → 0.393	0.636	0.109 (0.021)	2.596
49	Abdominal aorta II	0.432	0.732 → 0.726	1.203	-	-
50	Renal L	2.184	0.271 → 0.271	0.252	0.113 (0.023)	2.503
51	Abdominal aorta III	1.198	0.726 → 0.711	1.203	-	-
52	Renal R	3.772	0.310 → 0.310	0.524	0.113 (0.023)	2.495
53	Abdominal aorta IV	5.409	0.711 → 0.643	1.203	-	-
54	Inferior mesenteric	9.024	0.208 → 0.208	0.688	1.196 (0.240)	0.237
55	Abdominal aorta V	4.222	0.643 → 0.590	1.203	-	-
56	Common iliac R	7.643	0.450 → 0.409	0.916	-	-
57	Common iliac L	7.404	0.450 → 0.409	0.916	-	-
58	External iliac R	10.221	0.338 → 0.319	0.756	-	-
59	Internal iliac R	7.251	0.282 → 0.282	0.631	0.207 (0.041)	1.366
60	Femoral R I	3.159	0.319 → 0.314	0.291	-	-
61	Profunda femoris R	23.839	0.214 → 0.214	0.214	0.137 (0.034)	1.653
62	Internal iliac R	31.929	0.314 → 0.269	0.291	-	-
63	Femoral R II	13.203	0.269 → 0.237	0.291	-	-
64	Popliteal R I	38.622	0.117 → 0.117	0.144	1.226 (0.245)	0.231
65	Anterior tibial R	0.880	0.237 → 0.235	0.291	-	-
66	Popliteal R II	3.616	0.235 → 0.235	0.291	-	-
67	Tibiofibular trunk R	38.288	0.123 → 0.123	0.291	1.058 (0.211)	0.268
68	Posterior tibial R	10.221	0.338 → 0.319	0.756	-	-
69	Internal iliac L	7.251	0.282 → 0.282	0.631	0.208 (0.041)	1.362
70	Femoral L I	3.159	0.319 → 0.314	0.291	-	-
71	Profunda femoris L	23.839	0.214 → 0.214	0.214	0.1371(0.034)	1.653
72	Femoral L II	31.929	0.314 → 0.269	0.291	-	-
73	Popliteal L I	13.203	0.269 → 0.237	0.291	-	-
74	Anterior tibial L	38.622	0.117 → 0.117	0.144	1.227 (0.245)	0.231
75	Popliteal L II	0.880	0.237 → 0.235	0.291	-	-
76	Tibiofibular trunk L	3.616	0.235 → 0.235	0.291	-	-
77	Posterior tibial L	38.288	0.123 → 0.123	0.291	1.058 (0.212)	0.268

6.3. RESULTS

6.3.1 FORWARD DIRECTION

Figure 6.2 depicts the estimated pressure and velocity in two locations of the aorta. The tapered arterial causes higher pulse pressure and peak pressure across the aorta compared to the non-tapered measurements.

A higher value of velocity is estimated in the ascending aorta when the vessels are not tapered ($\Delta U_{peak} = 3.39$). Though, at the thoracic aorta the value of velocity is higher in tapered structure than non-tapered ($\Delta U_{peak} = 7.49 \text{ cm/s}$). Thus, the tapered structure augments the increase of velocity. The alteration is more evident in the pressure than the velocity values. The difference in pulse pressure of tapered and non-tapered in the ascending aorta and thoracic aorta is 10.11 mmHg and 11.23 mmHg , respectively. Similar augmentation of pressure reduction is evident in the peak pressure between the ascending aorta and the thoracic aorta.

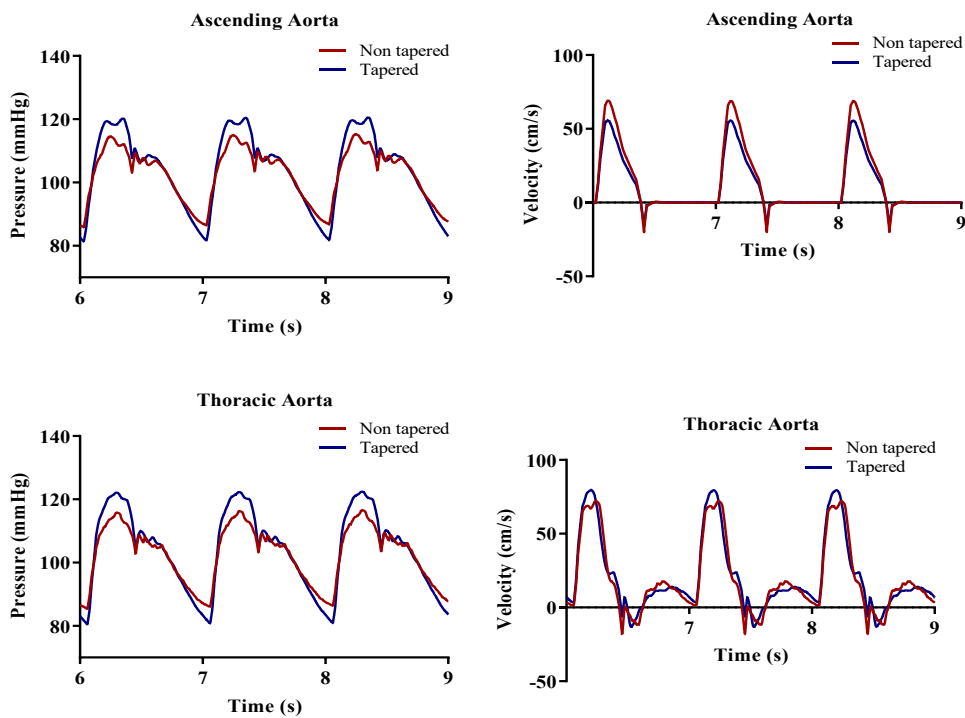


Figure 6. 2. Pressure (left) and velocity (right) at the ascending aorta (top row) and thoracic aorta in tapered and non-tapered arterial structures.

The wave intensity is calculated at two locations of the aorta, as shown in Figure 6.3. The forward intensity is higher in the tapered system both at the ascending aorta and the thoracic aorta. Also, the time of arrival of the backward wave intensity is earlier compared to the non-tapered structure.

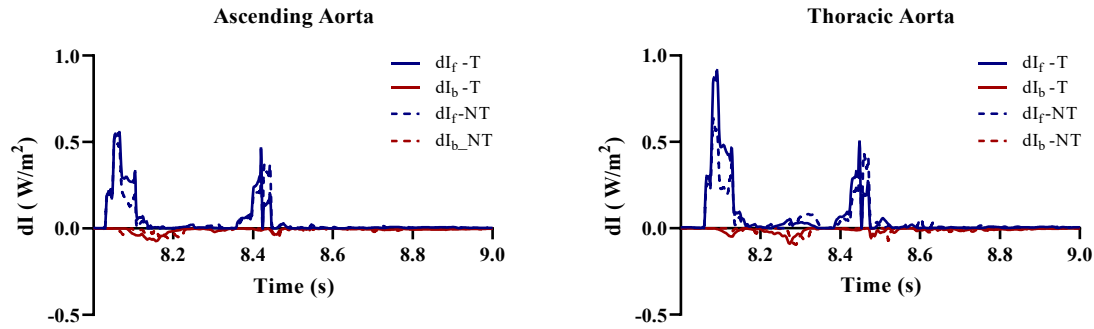


Figure 6. 3. Wave intensity analysis at the ascending aorta and thoracic aorta when the arterial tree is tapered (T) and non-tapered (NT)

The forward intensity is growing faster through the aorta in the tapered arterial tree, changing from 0.56 to 0.91 W/m^2 . In the non-tapered structure, the intensity only changes 0.11 w/m^2 .

6.3.2 BACKWARD DIRECTION

In these simulations, a semi Gaussian-shaped pulse is induced to the system from the left *profunda femoris*. In order to avoid confusion, the changes in the pressure and intensity are considered to be in the backward direction. As shown in Table 6.1, the radius of each vessel differs in the tapered and non-tapered model, and mostly it is higher in the non-tapered structure. Since diameter and pressure at each cross-section influence each other (Tube-law), to compare the results, the ratio of the value measured at the inlet of the pulse to the values of each location is used. Figure 6.4 depicts the ratio of the backward component of pressure throughout the aortic arch to the aortic root.

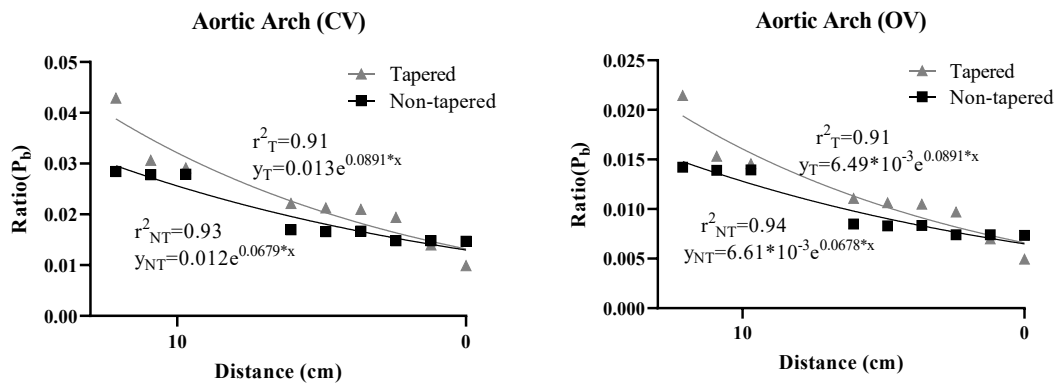


Figure 6. 4. The ratio of the backward pressure along the aortic arch and ascending aorta. The simulations are done in CV (left) and OV (right) conditions. In each figure, the ratios for the tapered and non-tapered structure is presented.

As shown in Figure 6.4, the values of OV is half of the values in the CV condition. The backward pressure is reducing exponentially in both tapered and non-tapered structure, and about 0.02-0.04 proportion of the pressure reaches the distal aorta, meaning that 98 per cent of the wave is dissipated, already. The ratio of the pressure in the tapered system is higher than the non-tapered. However, the slope of the reduction of the tapered structure is higher than non-tapered, meaning that the damping for the pulse is higher in the tapered arterial tree.

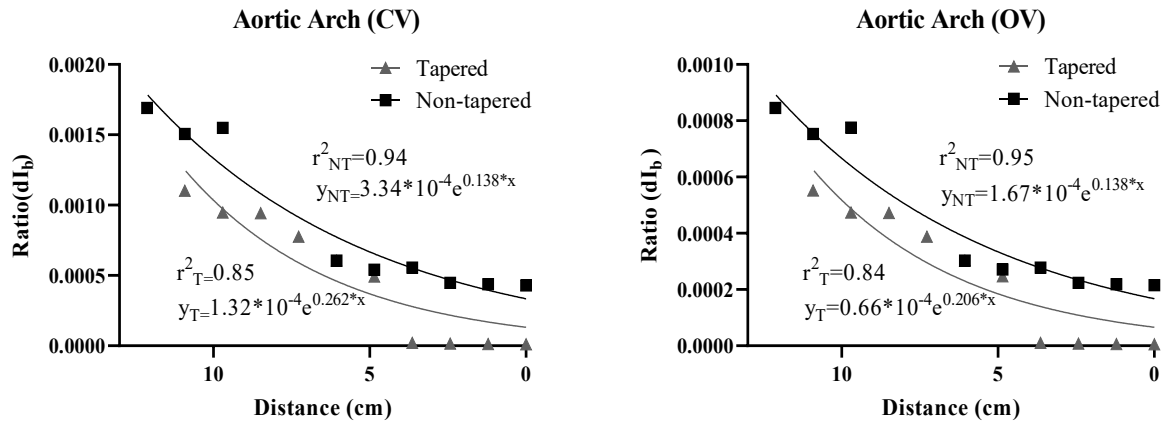


Figure 6. 5. The backward wave intensity ratio across the aortic arch when the pulse is travelling towards the ascending aorta in CV and OV conditions.

The WIA is implemented for the aortic arch in both arterial systems. In Figure 6.5, the ratio of the backward intensity is shown. Across the aortic arch, the wave intensity of the tapered structure is dropping faster, and it is lower compared to non-tapered one. Similar to the pressure, the values for the CV is double the values for OV.

6.4. DISCUSSION

In this chapter, we studied the impact of tapering in an arterial tree with 55 large arterial vessels. Unlike the simple arterial model that we used in chapter 5, this arterial tree consists of many more segments in interaction with each other. For limiting the sources of reflections only to the tapering, the non-tapered arterial tree has a similar area ratio to the tapered arterial tree at bifurcations.

Initially, both systems are compared using a physiological inflow induced from the heart (Murgo *et al.*, 1980). Both systems had similar timing in pressure and velocity; however, the pulse pressure and peak pressure were higher in the tapered system. A similar observation has been reported in (Abdullateef, Mariscal-Harana and Khir, 2020), where they increased the angle of tapering from 0 to 1.25° in a thoracic aortic model. The authors also reported an increase in arterial resistance and a decrease in arterial compliance when a vessel is tapered.

Consequently, in this study, the tapered arterial tree has a higher arterial resistance which explains the higher peak pressure. The non-tapered structure has higher arterial compliance and therefore, lower arterial pulse pressure. Keeping Young's modulus constant throughout the arterial tree reduced the complexity of our study. Also, according to (Wemple and Mockros, 1972), the elastic tapering in the arterial tree has a minor effect on the waves.

Wave intensity at the ascending aorta shows negligible differences in the forward direction. At the same time, the earlier arrival of reflection is evident in Figure 6.3. The forward wave intensity in thoracic aorta has a significant difference between tapered and non-tapered arterial tree; which is anticipated because the pressure and velocity rise more in the tapered structure compared to the non-tapered arterial tree (Figure 6.2). Similar results have been reported in (Abdullateef, Mariscal-Harana and Khir, 2020).

As the inflow is inserted from the distal limbs, the tapering of the arterial tree shows a higher ability to damp the wave travelling to the ascending aorta. The difference in the amplitude of the backward pressure reduces exponentially across the route of the wave. (Figure 6.4) The values of backward pressure in the tapered arterial tree is lower than values estimated in non-tapered structure. However, the inflow in both systems is similar. Changes are 99.95 % in tapered and 98.52 % for non-tapered. Similar exponential reductions are reported in (Feng, Long and Khir, 2007), where the authors used uniform elastic tubes.

Analysis of the wave intensity showed the exponential reduction of the backward intensity as the pulse travelled across the tree for both tapered and non-tapered structures. However, the wave dissipation in tapered arterial tree both in CV and OV conditions is higher, and the amplitude of wave intensity reaches zero. Also, the values for CV is doubled compared to OV, because the wave arriving at the closed valve reflects 100%.

There can be some reasons that the difference between tapered and non-tapered systems are not significant in our study. The main reason is that the reflection coefficients of the bifurcations are similar in both models, and bifurcations are the primary sources of reflections. Also, the changes due to tapering are small. Since the intensity has a component similar to the forward pressure but squared, the changes are more evident in the forward pressure than the forward intensity.

6.5. LIMITATIONS

In order to reduce the sources of the reflections in the non-tapered arterial tree and to focus only on reflections caused by tapering, the area ratio at all of the bifurcations is kept similar to

the tapered arterial tree. However, similar ratios can cause the vessels to have diameter values higher than the validated computational physiological model. The effect of this difference can be minimised by using a pulse with similar pulse pressure and using a ratio of the input value and the estimated values at different locations (Feng, Long and Khir, 2007). Moreover, the alteration in the diameter causes changes in the values of the wave speed, i.e. another different variable between the two models.

A constant Young's modulus helped us with limiting the variables. However, it is reported that the vessels' stiffness increases with distance from the heart (Learoyd and Taylor, 1966; Wemple and Mockros, 1972; Avolio, 1980; Myers and Capper, 2004). Thus, changing the value of Young's modulus according to its distance from the heart could provide a more accurate prediction of the response of the system to reflections. Moreover, according to (Reuderink *et al.*, 1989), neglecting the viscoelastic behaviour of the vessels' wall causes an underestimation in the damping ability of the system.

Another limitation of this study can be the absence of a pumping heart and the waves generated from the left ventricle, which can provide a more physiological response of the arterial tree to a reflection travelling from the periphery.

6.6. CONCLUSION

Only 1% of the magnitude of the reflection initiated from peripheral limbs can reach to the aortic root. The pressure waveform decays exponentially travelling in their backward towards the aortic root. Tapering caused a higher dissipation of the pressure wave compared to non-tapered, indicating this might be a natural physiological mechanism to protect the *in vivo* heart from the return of the reflected waves.

GENERAL DISCUSSION

Understanding the response of the arterial tree to pressure and flow waves is important as it may assist in diagnostic purposes and planning for treatments. For example, there is strong evidence that with ageing, pulse pressure increases due to arterial stiffening (Franklin *et al.*, 1997; Segers, Ernst R. Rietzschel, *et al.*, 2007; Nyhan *et al.*, 2011). However, the factors affecting the morphology of the pressure waveform in the ascending aorta are not fully understood. Furthermore, in particular, the origin of reflected waves present in the ascending aorta is a controversial topic (Segers *et al.*, 2017).

To better understand the underlying mechanism, there is a need to consider the role that the vascular system plays in the formation of the pressure waveform, as well as the heart. One approach to acquire this knowledge is modelling the cardiovascular system, as the arterial tree is very complex due to the multi-branching nature and the variation of the mechanical properties across the system.

A simplification of the physiological conditions can help in understanding the function of the arterial tree (Westerhof, Elzinga and Sipkema, 1971), and models are useful tools for such studies. 1D models have been widely used for the analysis of the global circulation in the arterial tree, and have been validated against *in vivo* (Davies *et al.*, 2012; Willemet, Lacroix and Marchandise, 2013) and *in vitro* (Matthys *et al.*, 2007) experiments. In this thesis, a 1D model is used to study wave reflections in a multi-branching system such as the arterial tree. The primary focus is to examine the influence of the physiological characteristics of the arterial tree on reflections, namely the mechanical properties, bifurcations and the tapering.

This problem is revisited by using a new approach. Rather than studying wave propagation as it travels from the heart to the periphery (forward direction), the route of a reflected wave travelling towards the heart (backward direction) is studied. This research is focused on answering a specific question; given the significant reflection coefficient at the bifurcations in the backward direction, how far can the wave travel, and whether all reflected waves would reach the ascending aorta.

A reflection is imposed from a distal location in the system, and the propagation of this wave towards the parent vessel is examined. The analysis started by focusing on the impact of the bifurcations and the increase in the number of consecutive bifurcations. The results showed that after the fifth generation of consecutive bifurcations, 95% of the reflected wave is dissipated. Also, the phenomenon of wave trapping between the consecutive bifurcations is systematically demonstrated. It can be noted that peripheral reflected waves do not have a significant effect on the aortic flows, because they get “trapped” on their way to the aorta, at the junctions of the network, which are not well matched for backward travelling waves.

This study is further extended by using a validated model of the arterial tree with 37 segments and imposing a reflection from the left anterior tibial. By monitoring the wave travelling towards the aortic root, results have shown that 75% of the initial wave magnitude is observed after the iliac bifurcation. Eventually, only 1% of the wave magnitude reaches to the aortic root. The absolute value of the wave travelling towards the aortic root decreased exponentially.

Previously, it has been demonstrated that the pulse originating from the ascending aorta diminished exponentially (Alastruey *et al.*, 2009; Davies *et al.*, 2012).

The outcomes of this research demonstrate a clear response of the arterial tree to a single reflection generated distally. However, because the sole influence of arterial tapering is still not well understood both in literature and in previous simulations of this research, a part of this thesis is dedicated to studying the impact of arterial tapering on wave propagation. The effect of increasing the arterial tapering angle is examined, which is one of the changes reported as a consequence of ageing. The outcomes demonstrated that higher tapering angle produced higher resistance and lowered arterial compliance, resulting in higher peak pressure and larger pulse pressure.

The impact of the tapering angle on wave speed is also studied, showing that higher tapering angle was associated with an increase in the mean and outlet wave speed, although the local wave speed at the inlet remained unchanged. As a result, reflected waves reached the root earlier. An explanation to this can be provided through the Moens-Korteweg’s equation (Equation 1.2), where the tapering causes a reduction in the diameter hence rises in the value of wave speed. We assume that the changes in elasticity and thickness are negligible, and the density of the blood remains constant.

Considering the equations of separation of pressure and wave intensity to their forward and backward components, as shown in Equations 2.67 and 2.68 in Chapter 2, the wave speed is a parameter influencing the amplitude of the forward and backward directions. If the vessel is

tapered, mean wave speed will increase; accordingly, an enhancement in the forward and a reduction in the backward components of the wave are expected, with similar dP and dU . Therefore, as the wave travels distally, more reflections are damped.

Pulse wave velocity (PWV), which is the clinical term used for wave speed, can be measured by calculating by the foot-to-foot method, which is $2L/\Delta t$ (Gaddum *et al.*, 2013). PWV has shown to be associated with cardiovascular risks (Blacher *et al.*, 1999; Laurent *et al.*, 2001), and due to the ease and ability to measure it non-invasively, it is considered to be the gold standard within clinical practises (Laurent *et al.*, 2001).

In (Westerhof *et al.*, 2008), the authors question that with ageing, the PWV increases while the Δt remains the same suggesting that the origin of the reflection is moving toward the periphery. In this study, it is shown that the increase of tapering angle, which is one of the changes in the ageing arterial tree can also increase the mean PWV. However, there are no changes in the length of the descending aorta (Hickson *et al.*, 2010; Charlton *et al.*, 2019). Hence, the results of this study agree with the authors of (Westerhof *et al.*, 2008), that using only the time of the return of the reflection and the distance is not sufficient for allocation of origin of the reflection wave. On the other hand, it is observed that only using the local wave speed might provide an indistinct explanation of the response of the system, since the tapering is affecting a region rather than a location.

In order to isolate the effect of tapering from the effect bifurcations, in Chapter 6 two structures are compared, one of which resembles the physiological dimensions and the other one has the same reflection coefficients at each bifurcation, but the vessels are not tapered. The difference between the wave intensity reaching the aortic arch in the two models is small, approximately 0.06%, which indicates that the major parameter that affects the pressure waveform morphology is the number and coefficient of the bifurcations along the arterial tree.

7.1. SUMMARY OF THE THESIS ACHIEVEMENT

In this thesis, the effect of bifurcations on reflections, re-reflections, and the trapping of waves between consecutive bifurcations is computationally demonstrated.

The correlation of the tapering angle and the mechanical properties of the thoracic aortic wall and its influence on pressure is examined, which explains some of the underlying changes in an ageing arterial tree. Then the findings of this study are compared with a clinical dataset of the ageing population.

To the best of author's knowledge, this is the first study to investigate the effect of tapering on wave intensity analysis.

7.2. IMPLICATIONS FOR FUTURE RESEARCH

In our studies, we have used setups that do not replicate the physiological environment of the arterial tree. However, we believe that our findings could demonstrate the response of the arterial tree by focusing on its geometrical features.

This study can undoubtedly be further improved with consideration of the cardiac response to the arterial tree. We considered the vessels with elastic behaviour, while it is reported that viscoelastic behaviour of the arterial tree can harvest better understanding of the ability of the arterial tree for damping the reflections, especially, in the studies related to tapering and the angle of tapering. The energy loss at bifurcations is neglected in our experiments. Thus, consideration of the energy loss will provide more accurate values.

Finally, the study on the impact of tapering can be validated by measuring the dimensions of the aorta in different age groups.

APPENDIX 1

CALCULATION OF ARTERIAL RESISTANCE AND COMPLIANCE

The authors of (Epstein *et al.*, 2015) developed a novel methodology to coalesce a single nonlinear 1D mode vessel with a length of l connected to a linear three-element Windkessel model, as shown in Figure A1.1, into a linear two-element Windkessel model. To replace the vessel with Windkessel elements, it was required to linearize Equations of conservation mass and momentum (Eq 2.4 and Eq 2.14) and the tube law (Eq 2.26).

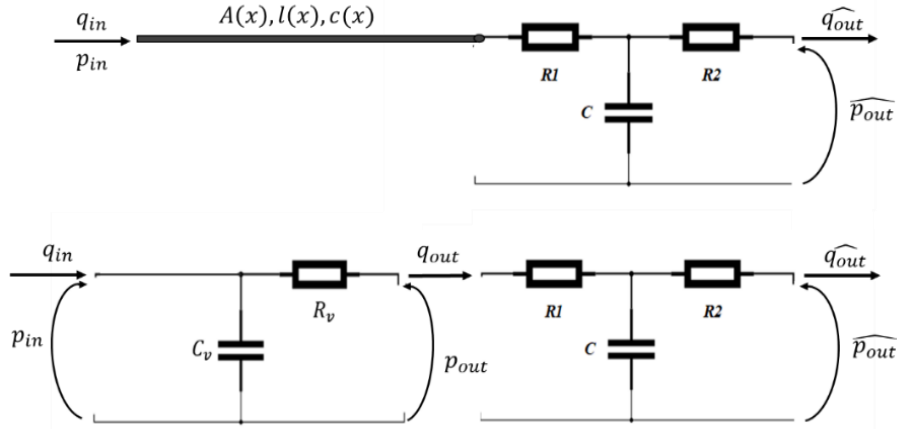


Figure A1. 1. Schematic representation of reduction of a single vessel into a two-element Wk model in 1D model

Each vessel has pressure and flow $p_{in}(t)$ and $q_{in}(t)$ at the inlet, and $p_{out}(t)$ and $q_{out}(t)$ at the outlet. The linearized 1D equations are as (Alastruey *et al.*, 2008)

$$\frac{A_0}{\rho c_d^2} \frac{\partial P}{\partial t} + \frac{\partial q}{\partial x} = 0, \quad (A.1)$$

$$\frac{\partial q}{\partial t} + \frac{A_d}{\rho} \frac{\partial P}{\partial x} = -\frac{2(\xi + 2)\pi\mu q}{\rho A_d}, \quad (A.2)$$

where instead of Q , UA is used. The diastolic condition is linearized to $(A, P, Q) = (A_d + a, P_d + p, q)$, where $a(x, t)$ and $p(x, t)$ and $q(x, t)$ are the variables cause by the perturbation in the area, pressure and flow rate.

The authors used the Mean value Theorem (MVT) stating that if $f: [b_1, b_2] \rightarrow \mathbb{R}$ is continuous and if $g \geq 0$ is bounded and continuous on $[b_1, b_2]$. Then there is $\epsilon \in [b_1, b_2]$ such that

$$\int_{b_1}^{b_2} f(x)g(x)dx = f(c) \int_{b_1}^{b_2} g(x)dx, \quad (\text{A. 3})$$

and

$$f(c) = \frac{\int_{b_1}^{b_2} f(x)g(x)dx}{\int_{b_1}^{b_2} g(x)dx}. \quad (\text{A. 4})$$

With Integration of the Equation A.1 along the x axis we have

$$\int_0^l \left(\underbrace{\frac{A_d}{\rho c_d^2} \frac{\partial P}{\partial t}}_a + \underbrace{\frac{\partial q}{\partial x}}_b \right) dx = 0. \quad (\text{A. 5})$$

For Equation A.2, $A_d(x)$ is divided from both sides and then integrated along the x axis and we get

$$\int_0^l \left(\frac{\partial q}{\partial t} \frac{1}{c} + \frac{A_d}{\rho} \frac{\partial P}{\partial x} \right) dx = - \int_0^l \frac{2(\xi + 2)\pi\mu q}{\rho A_d} dx, \quad (\text{A. 6})$$

Each element of Equation A.5 is evaluated separately as following:

$$(a) \int_0^l \frac{A_d}{\rho c_d^2} \frac{\partial P}{\partial t} dx = \frac{1}{\rho} \frac{dp(\epsilon_1, t)}{dt} \int_0^l \frac{A_d}{\rho c_d^2} dx;$$

$$(b) \int_0^l \frac{\partial q}{\partial x} dx = q_{out} - q_{in}, \text{ with } q_{out} = q(l, t) \text{ and } q_{in} = p(0, t).$$

Considering that $p(x, t)$ is continuous as well as A_d/c_d^2 , and since in physiological conditions $A_d > 0$ and $c_d > 0$, MVT theorem can be applied to (a) with $\epsilon_1 \in [0, l]$.

By evaluating Equation A.6, each term of the equation can be written as

$$(c) \int_0^l \frac{1}{A_d} \frac{\partial q}{\partial t} dx = \frac{1}{\rho} \frac{dq(\epsilon_2, t)}{dt} \int_0^l \frac{1}{A_d} dx;$$

$$(d) \int_0^l \frac{1}{\rho} \frac{\partial p}{\partial x} dx = \frac{p_{out} - p_{in}}{\rho} \int_0^l \frac{1}{A_d} dx, \text{ with } p_{out} = p(l, t) \text{ and } p_{in} = p(0, t); \text{ and}$$

$$(e) - \frac{2(\xi + 2)\pi\mu}{\rho} \int_0^l \frac{q}{A_d^2} dx = - \frac{2(\xi + 2)\pi\mu}{\rho} q(\epsilon_3, t) \int_0^l \frac{1}{A_d^2} dx.$$

Both $q(x, t)$ and $\partial q(x, t)/\partial t$ are continuous and, in a physiological environment, $1/A_d$ and $1/A_d^2$ are continuous and positive. Hence the MVT can be applied to (c) and (e), with ϵ_2 and $\epsilon_3 \in [0, l]$.

In the cardiovascular system, the arterial length varies from millimetres up to approximately 10 centimetres, while the waves propagate with a speed of 4 to 15 m/s . Hence, the transit time for a pulse wave to travel within a vessel is short in comparison with the duration of a cardiac cycle. Therefore, at any arbitrary time, space averaged values are close to piecewise ones and

$p(\epsilon_1, t) = p_{in}(t)$, $q(\epsilon_2, t) = q_{out}$ and $q(\epsilon_3, t) = q_{out}$ are reasonable (Milišić and Quarteroni, 2004). The equations A.5 and A.6 can be rewritten as

$$\underbrace{\frac{K_1}{\rho} \frac{dp_{in}}{dt}}_a + \underbrace{q_{out} - q_{in}}_b = 0, \quad (\text{A.7})$$

$$- \underbrace{\frac{2(\xi + 2)\pi\mu}{\rho} K_2 q_{out}}_e = \underbrace{K_3 \frac{dq_{out}}{dt}}_c + \underbrace{\frac{p_{out} - p_{in}}{\rho}}_d, \quad (\text{A.8})$$

with

$$K_1 = \int_0^l \frac{A_d}{c_d^2} dx, \quad K_2 = \int_0^l \frac{1}{A_d^2} dx, \quad K_3 = \int_0^l \frac{1}{A_d} dx. \quad (\text{A.9})$$

The term $C_v = K_1/\rho$ is the arterial compliance of the 1D vessel. It is assumed that the term for fluid inertia $K_3 dq_{out}/dt$ is insignificant, due to the negligible effect of peripheral inertia on flow waveforms. (Alastruey *et al.*, 2008). Hence, Equations A.7 and A.8 change to

$$C_v \frac{dp_{in}}{dt} + q_{out} - q_{in} = 0, \quad (\text{A.10})$$

$$p_{out} - p_{in} = -R_v q_{out}, \quad (\text{A.11})$$

With

$$R_v = 2(\xi + 2)\pi\mu K_2, \quad (\text{A.12})$$

where R_v is the resistance value for the 1D vessel.

REFERENCES

- Abdullateef, S. *et al.* (2019) ‘A Study on the Characteristics Influencing the Pressure at the Root of a Distributed One-Dimensional Model of Arterial Blood Flow’, in *2018 Computing in Cardiology Conference (CinC)*, pp. 4–7. doi: 10.22489/cinc.2018.223.
- Abdullateef, S. *et al.* (2020) ‘P124 Impact of Tapering on Arterial Blood Pressure Using a One-dimensional Computational Model’, *Artery Research*, 25(10), pp. S164–S164.
- Abdullateef, S., Mariscal-Harana, J. and Khir, A. W. (2020) ‘Impact of Tapering of Arterial Vessels on Blood Pressure, Pulse Wave Velocity, and Wave Intensity Analysis using 1-Dimensional Computational Model’, *International Journal for Numerical Methods in Biomedical Engineering*, 18, p. e3312. doi: 10.1002/cnm.3312.
- Alastruey, J. (2006) *Numerical Modelling of Pulse Wave Propagation in the Cardiovascular System: Development, Validation and clinical applications*, PhD Thesis, Imperial College London. Imperial College London.
- Alastruey, J. *et al.* (2007) ‘Modelling the circle of Willis to assess the effects of anatomical variations and occlusions on cerebral flows’, *Journal of Biomechanics*. Elsevier, 40(8), pp. 1794–1805. doi: 10.1016/j.jbiomech.2006.07.008.
- Alastruey, J. *et al.* (2008) ‘Lumped Parameter Outflow Models for 1-D Blood Flow Simulations : Effect on Pulse Waves and Parameter Estimation’, *Communications in Computational Physics*, 4(2), pp. 317–336.
- Alastruey, J. *et al.* (2009) ‘Analysing the pattern of pulse waves in arterial networks: A time-domain study’, *Journal of Engineering Mathematics*, 64(4), pp. 331–351. doi: 10.1007/s10665-009-9275-1.
- Alastruey, J. (2011) ‘Numerical assessment of time-domain methods for the estimation of local arterial pulse wave speed’, *Journal of Biomechanics*. Elsevier, 44(5), pp. 885–891. doi: 10.1016/j.jbiomech.2010.12.002.
- Alastruey, J. *et al.* (2011) ‘Pulse wave propagation in a model human arterial network: Assessment of 1-D visco-elastic simulations against in vitro measurements’, *Journal of Biomechanics*, 44(12), pp. 2250–2258. doi: 10.1016/j.jbiomech.2011.05.041.
- Alastruey, J. *et al.* (2012) ‘Physical determining factors of the arterial pulse waveform: Theoretical analysis and calculation using the 1-D formulation’, *Journal of Engineering Mathematics*, 77(1), pp. 19–37. doi: 10.1007/s10665-012-9555-z.
- Alastruey, J., Parker, Kim H and Sherwin, S. J. (2012) ‘Arterial pulse wave haemodynamics’,

- 11th International Conference on Pressure Surges*, (October), pp. 401–443. Available at: http://www2.imperial.ac.uk/ssherw/spectralhp/papers/PulseSurges_2012.pdf.
- Alastruey, J., Parker, Kim H. and Sherwin, S. J. (2012) ‘Arterial pulse wave haemodynamics’, in *BHR Group - 11th International Conferences on Pressure Surges*, pp. 401–442.
- Anliker, M., Rockwell, R. L. and Ogden, E. (1971) ‘Nonlinear analysis of flow pulses and shock waves in arteries - Part I: Derivation and properties of mathematical model’, *Zeitschrift für angewandte Mathematik und Physik ZAMP*. Birkhäuser-Verlag, 22(2), pp. 217–246. doi: 10.1007/BF01591407.
- Atabek, H. B. (1968) ‘WAVE PROPAGATION THROUGH A VISCOUS FLUID CONTAINED IN A TETHERED, INITIALLY STRESSED, ORTHOTROPIC ELASTIC TUBE’, *Biophysical j*, 8, pp. 626–649.
- Atabek, H. B. and Lew, H. S. (1966) ‘Wave Propagation through a Viscous Incompressible Fluid Contained in an Initially Stressed Elastic Tube’, *Biophysical Journal*. The Biophysical Society, 6(4), pp. 481–503. doi: 10.1016/S0006-3495(66)86671-7.
- Avolio, A. P. (1980) ‘Multi-branched model of the human arterial system’, *Medical & Biological Engineering & Computing*. Kluwer Academic Publishers, 18(6), pp. 709–718. doi: 10.1007/BF02441895.
- Azer, K. and Peskin, C. S. (2007) ‘A one-dimensional model of blood flow in arteries with friction and convection based on the Womersley velocity profile’, *Cardiovascular Engineering*, 7(2), pp. 51–73. doi: 10.1007/s10558-007-9031-y.
- Baker, G. F., Tortora, G. J. and Nostakos, N. P. A. (1976) ‘Principles of Anatomy and Physiology’, *The American Journal of Nursing*. HarperCollinsCollege, 76(3), p. 477. doi: 10.2307/3423898.
- Balar, S. D., Rogge, T. R. and Young, D. F. (1989) ‘Computer simulation of blood flow in the human arm’, *Journal of Biomechanics*, 22(6–7), pp. 691–697. doi: 10.1016/0021-9290(89)90019-5.
- Barnard, A. C. L. *et al.* (1966) ‘A Theory of Fluid Flow in Compliant Tubes’, *Biophysical Journal*, 6(6), pp. 717–724. doi: 10.1016/S0006-3495(66)86690-0.
- Bauer, R. ., Pasch, T. and Wetterer, E. (1972) ‘THEORETICAL STUDIES ON THE HUMAN ARTERIAL PRESSURE AND FLOW PULSE BY MEANS OF A NON-UNIFORM TUBE MODEL’, *Journal of Biomechanics*, 6, pp. 289–298. Available at: https://ac.els-cdn.com/0021929073900511/1-s2.0-0021929073900511-main.pdf?_tid=1f12fd7e-b60e-440b-956e-f252d5752abc&acdnat=1530633337_209e6d6cb091cee77c5afc3e5146dedf (Accessed: 3 July 2018).

- Bessems, D., Rutten, M. and Van De Vosse, F. (2007) 'A wave propagation model of blood flow in large vessels using an approximate velocity profile function', *Journal of Fluid Mechanics*, 580, pp. 145–168. doi: 10.1017/S0022112007005344.
- Blacher, J. *et al.* (1999) 'Aortic pulse wave velocity as a marker of cardiovascular risk in hypertensive patients', *Hypertension*. Lippincott Williams and Wilkins, 33(5), pp. 1111–1117. doi: 10.1161/01.HYP.33.5.1111.
- Blanco, P. J. *et al.* (2015) 'An anatomically detailed arterial network model for one-dimensional computational hemodynamics', *IEEE Transactions on Biomedical Engineering*. IEEE Computer Society, 62(2), pp. 736–753. doi: 10.1109/TBME.2014.2364522.
- Boileau, E. *et al.* (2015) 'A benchmark study of numerical schemes for one-dimensional arterial blood flow modelling', *International Journal for Numerical Methods in Biomedical Engineering*. Wiley-Blackwell, 31(10), pp. 1–33. doi: 10.1002/cnm.2732.
- Borlotti, A. *et al.* (2012) 'Noninvasive determination of local pulse wave velocity and wave intensity: Changes with age and gender in the carotid and femoral arteries of healthy human', *Journal of Applied Physiology*. American Physiological Society Bethesda, MD, 113(5), pp. 727–735. doi: 10.1152/jappphysiol.00164.2012.
- Bos, G. C. V. Den *et al.* (1976) 'Reflection in the systemic arterial system: Effects of aortic and carotid occlusion', *Cardiovascular Research*, 10(5), pp. 565–573. doi: 10.1093/cvr/10.5.565.
- Bramwell, J. C. and Hill, A. V. (1922) 'The velocity of pulse wave in man', *Proceedings of the Royal Society of London. Series B, Containing Papers of a Biological Character*. The Royal Society, 93(652), pp. 298–306. doi: 10.1098/rspb.1922.0022.
- Brook, B. S., Falle, S. A. E. G. and Pedley, T. J. (1999) 'Numerical solutions for unsteady gravity-driven flows in collapsible tubes: Evolution and roll-wave instability of a steady state', *Journal of Fluid Mechanics*, 396, pp. 223–256. doi: 10.1017/S0022112099006084.
- Broyd, C. J. *et al.* (2017) 'Wave intensity analysis and its application to the coronary circulation', *Global Cardiology Science and Practice*, 2017(1), p. e201705. doi: 10.21542/gcsp.2017.5.
- Burattini, R. and Campbell, K. B. (1989) 'Modified Asymmetric T-Tube Model to Infer Arterial Wave Reflection at the Aortic Root', *IEEE Transactions on Biomedical Engineering*, 36(8), pp. 805–814. doi: 10.1109/10.30806.
- Burattini, R. and Gnudi, G. (1982) 'Computer identification of models for the arterial tree input impedance: Comparison between two new simple models and first experimental results', *Medical & Biological Engineering & Computing*. Kluwer Academic Publishers, 20(2), pp. 134–144. doi: 10.1007/BF02441348.
- Burattini, R. and Di Salvia, P. O. (2007) 'Development of systemic arterial mechanical properties

- from infancy to adulthood interpreted by four-element windkessel models’, *Journal of Applied Physiology*, 103(1), pp. 66–79. doi: 10.1152/jappphysiol.00664.2006.
- Caro, C. G. *et al.* (2011) *The mechanics of the circulation, second edition, The Mechanics of the Circulation, Second Edition*. Cambridge: Cambridge University Press. doi: 10.1017/CBO9781139013406.
- Charlton, P. H. *et al.* (2019) ‘Modeling arterial pulse waves in healthy aging: a database for in silico evaluation of hemodynamics and pulse wave indexes’, *American journal of physiology. Heart and circulatory physiology*, 317(5), pp. H1062–H1085. doi: 10.1152/ajpheart.00218.2019.
- Chemla, D. *et al.* (1998) ‘Total arterial compliance estimated by stroke volume-to-aortic pulse pressure ratio in humans’, *American Journal of Physiology - Heart and Circulatory Physiology*, 274(2), pp. H500–5. doi: 10.1152/ajpheart.1998.274.2.h500.
- Chiesa, S. T. *et al.* (2019) ‘Carotid artery wave intensity in mid-to late-life predicts cognitive decline: The Whitehall II study’, *European Heart Journal*, 40(28), pp. 2300–2309. doi: 10.1093/eurheartj/ehz189.
- Collins, J. A. *et al.* (2014) ‘The anatomy of the aging aorta’, *Clinical Anatomy*. Wiley Periodicals, Inc, 27(3), pp. 463–466. doi: 10.1002/ca.22384.
- Davies, J. E. *et al.* (2006) ‘Evidence of a dominant backward-propagating “suction” wave responsible for diastolic coronary filling in humans, attenuated in left ventricular hypertrophy’, *Circulation*, 113(14), pp. 1768–78. doi: 10.1161/CIRCULATIONAHA.105.603050.
- Davies, J. E. *et al.* (2012) ‘Attenuation of Wave Reflection by Wave Entrapment Creates a “Horizon Effect” in the Human Aorta’, *Hypertension*, 60, pp. 778–785. doi: 10.1161/HYPERTENSIONAHA.
- Epstein, S. *et al.* (2015) ‘Reducing the number of parameters in 1D arterial blood flow modeling: Less is more for patient-specific simulations’, *American Journal of Physiology - Heart and Circulatory Physiology*. American Physiological Society Bethesda, MD, 309(1), pp. H222–H234. doi: 10.1152/ajpheart.00857.2014.
- Feng, J. and Khir, A. W. (2008) ‘The compression and expansion waves of the forward and backward flows: An in-vitro arterial model’, *Proceedings of the Institution of Mechanical Engineers, Part H: Journal of Engineering in Medicine*, 222(4), pp. 531–542. doi: 10.1243/09544119JEIM339.
- Feng, J. and Khir, A. W. (2010) ‘Determination of wave speed and wave separation in the arteries using diameter and velocity’, *Journal of Biomechanics*. Elsevier, 43(3), pp. 455–462. doi: 10.1016/j.jbiomech.2009.09.046.

- Feng, J., Long, Q. and Khir, A. W. (2007) ‘Wave dissipation in flexible tubes in the time domain: In vitro model of arterial waves’, *Journal of Biomechanics*. Elsevier, 40(10), pp. 2130–2138. doi: 10.1016/J.JBIOMECH.2006.10.034.
- Formaggia, L. *et al.* (2006) ‘Numerical modeling of 1D arterial networks coupled with a lumped parameters description of the heart’, *Computer Methods in Biomechanics and Biomedical Engineering*, 9(5), pp. 273–288. doi: 10.1080/10255840600857767.
- Formaggia, L., Lamponi, D. and Quarteroni, A. (2003) ‘One-dimensional models for blood flow in arteries’, *Journal of Engineering Mathematics*, 47(3–4), pp. 251–276. doi: 10.1023/B:ENGI.0000007980.01347.29.
- Fourier, J. B. J. (2009) *Théorie Analytique de la Chaleur*. 1st edn, *Théorie Analytique de la Chaleur*. 1st edn. Paris: Firmin Didot. doi: 10.1017/cbo9780511693229.
- Frank, O. (1899) ‘Die Grundform des arteriellen Pulses’, *Zeitschrift für Biologie*, 27, pp. 483–526.
- Frank, O. (1905) ‘Der Puls in den Arterien’, *Zeitschrift für Biologie*, 46, pp. 441–553.
- Franklin, S. S. *et al.* (1997) ‘Hemodynamic patterns of age-related changes in blood pressure: The Framingham heart study’, *Circulation*. Lippincott Williams and Wilkins, 96(1), pp. 308–315. doi: 10.1161/01.CIR.96.1.308.
- Fung, Y. C. (1996) *Biomechanics: Circulation*, Springer.
- Gaddum, N. R. *et al.* (2013) ‘A technical assessment of pulse wave velocity algorithms applied to non-invasive arterial waveforms’, *Annals of Biomedical Engineering*. Springer US, 41(12), pp. 2617–2629. doi: 10.1007/s10439-013-0854-y.
- Ghigo, A. R. *et al.* (2017) ‘Linear and Nonlinear Viscoelastic Arterial Wall Models: Application on Animals’, *Journal of Biomechanical Engineering*, 139(1), p. 011003. doi: 10.1115/1.4034832.
- Greenwald, S. E., Carter, A. C. and Berry, C. L. (1990) ‘Effect of age on the in vitro reflection coefficient of the aortoiliac bifurcation in humans’, *Circulation*, 82(1), pp. 114–123. doi: 10.1161/01.CIR.82.1.114.
- Hacham, W. S. and Khir, A. W. (2019) ‘The speed, reflection and intensity of waves propagating in flexible tubes with aneurysm and stenosis: Experimental investigation’, *Proceedings of the Institution of Mechanical Engineers, Part H: Journal of Engineering in Medicine*. SAGE Publications Ltd, 233(10), pp. 979–988. doi: 10.1177/0954411919859994.
- Hall, P. (1974) ‘Unsteady viscous flow in a pipe of slowly varying cross-section’, *Journal of Fluid Mechanics*. Cambridge University Press, 64(2), pp. 209–226. doi: 10.1017/S0022112074002369.

- Hardy-Stashin, J., Meyer, W. W. and Kauffman, S. L. (1980) 'Branching coefficient ("area ratio") of the human aortic bifurcation determined in distended specimens', *Atherosclerosis*. Elsevier, 37(3), pp. 399–402. doi: 10.1016/0021-9150(80)90144-6.
- Harvey, W. (1628) *Exercitatio anatomica de motu cordis et sanguinis in animalibus*. Frankfurt: William Fitzer.
- Hellevik, L. R. *et al.* (2009) 'An assessment of ductus venosus tapering and wave transmission from the fetal heart', *Biomechanics and Modeling in Mechanobiology*, 8(6), pp. 509–517. doi: 10.1007/s10237-009-0155-4.
- Hickson, S. S. *et al.* (2010) 'The relationship of age with regional aortic stiffness and diameter', *JACC: Cardiovascular Imaging*, 3(12), pp. 1247–1255. doi: 10.1016/j.jcmg.2010.09.016.
- Histand, M. B. and Anliker, M. (1973) 'Influence of flow and pressure on wave propagation in the canine aorta', *Circulation Research*, 32(4), pp. 524–529. doi: 10.1161/01.res.32.4.524.
- Holenstein, R., Niederer, P. and Anliker, M. (1980) 'A viscoelastic model for use in predicting arterial pulse waves', *Journal of Biomechanical Engineering*. American Society of Mechanical Engineers, 102(4), pp. 318–325. doi: 10.1115/1.3138229.
- Holzapfel, G. A., Gasser, T. C. and Stadler, M. (2002) 'A structural model for the viscoelastic behavior of arterial walls: Continuum formulation and finite element analysis', *European Journal of Mechanics, A/Solids*, 21(3), pp. 441–463. doi: 10.1016/S0997-7538(01)01206-2.
- Jones, C. J. H. *et al.* (2002) 'Compression and expansion wavefront travel in canine ascending aortic flow: Wave intensity analysis', *Heart and Vessels*. Springer-Verlag Tokyo, 16(3), pp. 91–98. doi: 10.1007/s003800200002.
- Karniadakis, G. and Sherwin, S. (2007) *Spectral/hp Element Methods for Computational Fluid Dynamics, Spectral/hp Element Methods for Computational Fluid Dynamics*. Oxford University Press. doi: 10.1093/acprof:oso/9780198528692.001.0001.
- Karreman, G. (1952) 'Some contributions to the mathematical biology of blood circulation. Reflections of pressure waves in the arterial system', *The Bulletin of Mathematical Biophysics*. Kluwer Academic Publishers, 14(4), pp. 327–350. doi: 10.1007/BF02477850.
- Khair, A. W. *et al.* (2001) 'Determination of wave speed and wave separation in the arteries', *Journal of Biomechanics*. Elsevier, 34(9), pp. 1145–1155. doi: 10.1016/S0021-9290(01)00076-8.
- Khair, A. W. *et al.* (2007) 'Simultaneous determination of wave speed and arrival time of reflected waves using the pressure-velocity loop', *Medical and Biological Engineering and Computing*, 45(12), pp. 1201–1210. doi: 10.1007/s11517-007-0241-7.
- Khair, A. W. and Parker, K. H. (2002) 'Measurements of wave speed and reflected waves in elastic

- tubes and bifurcations’, *Journal of Biomechanics*. Elsevier, 35(6), pp. 775–783. doi: 10.1016/S0021-9290(02)00025-8.
- Khiri, A. W. and Parker, K. H. (2005) ‘Wave intensity in the ascending aorta: Effects of arterial occlusion’, *Journal of Biomechanics*, 38(4), pp. 647–655. doi: 10.1016/j.jbiomech.2004.05.039.
- Kim, H. L. *et al.* (2017) ‘Association between arterial stiffness and left ventricular diastolic function in relation to gender and age’, *Medicine (United States)*. Wolters Kluwer Health, 96(1), p. e5783. doi: 10.1097/MD.0000000000005783.
- Koh, T. W. *et al.* (1998) ‘Analysis of wave reflections in the arterial system using wave intensity: A novel method for predicting the timing and amplitude of reflected waves’, *Heart and Vessels*, 13(3), pp. 103–113. doi: 10.1007/BF01747827.
- Kolyva, C. and Khiri, A. (2015) ‘Wave intensity analysis in the great arteries – What has been learnt during the last 25 years? Part 1’, *International Cardiovascular Forum Journal*, 1(2), p. 68. doi: 10.17987/icfj.v1i2.23.
- Korteweg, D. J. (1878) ‘Ueber die Fortpflanzungsgeschwindigkeit des Schalles in elastischen Röhren’, *Annalen der Physik*, 241(12), pp. 525–542. doi: 10.1002/andp.18782411206.
- Lau, E. M. T. *et al.* (2014) ‘Assessment of ventriculo-arterial interaction in pulmonary arterial hypertension using wave intensity analysis’, *European Respiratory Journal*. European Respiratory Society, 43(6), pp. 1804–1807. doi: 10.1183/09031936.00148313.
- Laurent, S. *et al.* (2001) ‘Aortic stiffness is an independent predictor of all-cause and cardiovascular mortality in hypertensive patients’, *Hypertension*. Lippincott Williams and Wilkins, 37(5), pp. 1236–1241. doi: 10.1161/01.HYP.37.5.1236.
- Laxminarayan, S. (1979) ‘The calculation of forward and backward waves in the arterial system’, *Medical & Biological Engineering & Computing*, 17(1), p. 130. doi: 10.1007/BF02440966.
- Learoyd, B. M. and Taylor, M. G. (1966) ‘Alterations with age in the viscoelastic properties of human arterial walls.’, *Circulation research*, 18(3), pp. 278–292. doi: 10.1161/01.RES.18.3.278.
- Li, Y. *et al.* (2019) ‘Stiffening and ventricular–arterial interaction in the ascending aorta using MRI’, *Journal of Hypertension*. Lippincott Williams and Wilkins, 37(2), pp. 347–355. doi: 10.1097/HJH.0000000000001886.
- Lighthill, M. J. (1967) ‘Waves in fluids’, *Communications on Pure and Applied Mathematics*, 20(2), pp. 267–293. doi: 10.1002/cpa.3160200204.
- López-Beltrán, E. A. *et al.* (1998) ‘Non-invasive studies of peripheral vascular compliance using a non-occluding photoplethysmographic method’, *Medical and Biological Engineering and*

- Computing*. Peter Peregrinus Ltd, 36(6), pp. 748–753. doi: 10.1007/BF02518879.
- LUCHSINGER, P. C. *et al.* (1964) ‘Instantaneous Pressure Distribution Along the Human Aorta.’, *Circulation research*, 15, pp. 503–510. doi: 10.1161/01.RES.15.6.503.
- Martin, C. *et al.* (2013) ‘Age-dependent ascending aorta mechanics assessed through multiphase CT’, *Annals of Biomedical Engineering*, 41(12), p. 256574. doi: 10.1007/s10439-013-0856-9.
- Matthys, K. S. *et al.* (2007) ‘Pulse wave propagation in a model human arterial network: Assessment of 1-D numerical simulations against in vitro measurements’, *Journal of Biomechanics*, 40(15), pp. 3476–3486. doi: 10.1016/j.jbiomech.2007.05.027.
- Milišić, V. and Quarteroni, A. (2004) ‘Analysis of lumped parameter models for blood flow simulations and their relation with 1D models’, *Mathematical Modelling and Numerical Analysis*, 38(4), pp. 613–632. doi: 10.1051/m2an:2004036.
- Mills, C. J. *et al.* (1970) ‘Pressure-flow relationships and vascular impedance in man’, *Cardiovascular Research*. Oxford University Press, 4(4), pp. 405–417. doi: 10.1093/cvr/4.4.405.
- Mitchell, G. F. *et al.* (2004) ‘Changes in arterial stiffness and wave reflection with advancing age in healthy men and women: The Framingham Heart Study’, *Hypertension*, 43(6), pp. 1239–1245. doi: 10.1161/01.HYP.0000128420.01881.aa.
- Mitchell, G. F. (2008) ‘Effects of central arterial aging on the structure and function of the peripheral vasculature: Implications for end-organ damage’, *Journal of Applied Physiology*. American Physiological Society, 105(5), pp. 1652–1660. doi: 10.1152/jappphysiol.90549.2008.
- Mitchell, G. F. (2009) ‘Clinical achievements of impedance analysis’, *Medical and Biological Engineering and Computing*. Springer-Verlag, 47(2), pp. 153–163. doi: 10.1007/s11517-008-0402-3.
- Mitchell, G. F. *et al.* (2014) ‘Arterial Stiffness and Cardiovascular Events The Framingham Heart Study’, *Circulation*, 121(4), pp. 505–511. doi: 10.1161/circulationaha.109.886655.
- Moens, A. I. (1877) *Over de voortplantingssnelheid ven den pols*. Leiden, The Netherlands.
- Montecinos, G. I., Müller, L. O. and Toro, E. F. (2014) ‘Hyperbolic reformulation of a 1D viscoelastic blood flow model and ADER finite volume schemes’, *Journal of Computational Physics*, 266, pp. 101–123. doi: 10.1016/j.jcp.2014.02.013.
- Mu, W. *et al.* (2013) ‘Effect of tapered angles in an artery on distribution of blood flow pressure with gravity considered’, *Journal of Biomedical Science and Engineering*, 06(12), pp. 14–20. doi: 10.4236/jbise.2013.612a003.
- Müller, L. O. and Toro, E. F. (2013) ‘Well-balanced high-order solver for blood flow in networks

- of vessels with variable properties', *International Journal for Numerical Methods in Biomedical Engineering*, 29(12), pp. 1388–1411. doi: 10.1002/cnm.2580.
- Murakami, T. (2017) 'Enhanced Aortic Pressure Wave Reflection in Patients with Aortic Coarctation after Aortic Arch Repair', *Pulse*, 5(1–4), pp. 82–87. doi: 10.1159/000478530.
- Murgo, J. P. *et al.* (1980) 'Aortic input impedance in normal man: Relationship to pressure wave forms', *Circulation*, 62(1), pp. 105–116. doi: 10.1161/01.CIR.62.1.105.
- Myers, L. J. and Capper, W. L. (2004) 'Exponential taper in arteries: An exact solution of its effect on blood flow velocity waveforms and impedance', *Medical Engineering and Physics*, 26(2), pp. 147–155. doi: 10.1016/S1350-4533(03)00117-6.
- Mynard, J. P. *et al.* (2012) 'Non-linear separation of pressure, velocity and wave intensity into forward and backward components', *Medical and Biological Engineering and Computing*. Springer-Verlag, 50(6), pp. 641–648. doi: 10.1007/s11517-012-0897-5.
- Mynard, J. P. and Smolich, J. J. (2014) 'Wave potential and the one-dimensional windkessel as a wave-based paradigm of diastolic arterial hemodynamics', *American Journal of Physiology - Heart and Circulatory Physiology*. American Physiological Society Bethesda, MD, 307(3), pp. H307–H318. doi: 10.1152/ajpheart.00293.2014.
- Mynard, J. P. and Valen-Sendstad, K. (2015) 'A unified method for estimating pressure losses at vascular junctions', *International Journal for Numerical Methods in Biomedical Engineering*. John Wiley & Sons, Ltd, 31(7), pp. 1–23. doi: 10.1002/cnm.2717.
- Mynard, J., Penny, D. J. and Smolich, J. J. (2008) 'Wave intensity amplification and attenuation in non-linear flow: Implications for the calculation of local reflection coefficients', *Journal of Biomechanics*. Elsevier, 41(16), pp. 3314–3321. doi: 10.1016/j.jbiomech.2008.10.002.
- Noordergraaf, A., Verdouw, P. D. and Boom, H. B. K. (1963) 'The use of an analog computer in a circulation model', *Progress in Cardiovascular Diseases*. W.B. Saunders, 5(5), pp. 419–439. doi: 10.1016/S0033-0620(63)80009-2.
- Nyhan, D. *et al.* (2011) 'Vascular stiffness and increased pulse pressure in the aging cardiovascular system', *Cardiology Research and Practice*, 1(1), p. 263585 (8 pages). doi: 10.4061/2011/263585.
- O'Rourke, M. F. *et al.* (1968) 'Pressure wave transmission along the human aorta. Changes with age and in arterial degenerative disease.', *Circulation research*, 23(4), pp. 567–579. doi: 10.1161/01.RES.23.4.567.
- O'Rourke, M. F. and Hashimoto, J. (2007) 'Mechanical Factors in Arterial Aging. A Clinical Perspective', *Journal of the American College of Cardiology*. Elsevier, 50(1), pp. 1–13. doi: 10.1016/j.jacc.2006.12.050.

- O'Rourke, M. F. and Nichols, W. W. (2005) 'Aortic diameter, aortic stiffness, and wave reflection increase with age and isolated systolic hypertension', *Hypertension*. Lippincott Williams & Wilkins, 45(4), pp. 652–658. doi: 10.1161/01.HYP.0000153793.84859.b8.
- O'Rourke, M., Farnsworth, A. and O'Rourke, J. (2008) 'Aortic Dimensions and Stiffness in Normal Adults', *JACC: Cardiovascular Imaging*. Elsevier, 1(6), pp. 749–751. doi: 10.1016/j.jcmg.2008.08.002.
- Olufsen, M. S. (1999) 'Structured tree outflow condition for blood flow in larger systemic arteries', *American Journal of Physiology - Heart and Circulatory Physiology*. American Physiological Society Bethesda, MD, 276(1), pp. H257–H268. doi: 10.1152/ajpheart.1999.276.1.h257.
- Olufsen, M. S. *et al.* (2000) 'Numerical simulation and experimental validation of blood flow in arteries with structured-tree outflow conditions', *Annals of Biomedical Engineering*. Kluwer Academic Publishers-Plenum Publishers, 28(11), pp. 1281–1299. doi: 10.1114/1.1326031.
- Papageorgiou, G. L. *et al.* (1990) 'The area ratio of normal arterial junctions and its implications in pulse wave reflections', *Cardiovascular Research*, pp. 478–484. doi: 10.1093/cvr/24.6.478.
- Parker, K. H. *et al.* (1988) 'What stops the flow of blood from the heart?', *Heart and Vessels*. Springer-Verlag, 4(4), pp. 241–245. doi: 10.1007/BF02058593.
- Parker, K. H. (2009) 'An introduction to wave intensity analysis', *Medical and Biological Engineering and Computing*, 47(2), pp. 175–188. doi: 10.1007/s11517-009-0439-y.
- Parker, K. H. and Jones, C. J. H. (1990) 'Forward and backward running waves in the arteries: Analysis using the method of characteristics', *Journal of Biomechanical Engineering*. American Society of Mechanical Engineers, 112(3), pp. 322–326. doi: 10.1115/1.2891191.
- PATEL, D. J. *et al.* (1963) 'RELATIONSHIP OF RADIUS TO PRESSURE ALONG THE AORTA IN LIVING DOGS.', *Journal of applied physiology*, 18, pp. 1111–1117. doi: 10.1152/jappl.1963.18.6.1111.
- Pedley, T. J. (1980) 'The Fluid Mechanics of Large Blood Vessels', *Journal of Biomechanical Engineering*. Cambridge University Press, 102(4), pp. 345–346. doi: 10.1017/cbo9780511896996.
- Pedley, T. J. (2003) 'Mathematical modelling of arterial fluid dynamics', *Journal of Engineering Mathematics*, 47(3–4), pp. 419–444.
- Peiro, J., Sherwin, S. and Parker, K. (2003) 'Numerical simulation of arterial pulse propagation using one-dimensional models', *Wall-Fluid Interactions in Physiological Flows*. Available at: <http://www2.imperial.ac.uk/ssherw/spectralhp/papers/1DChapter.pdf>.
- Peiró, J. and Veneziani, A. (2009) 'Reduced models of the cardiovascular system', in *Modeling*,

-
- Simulation and Applications*. Milano: Springer Milan, pp. 347–394. doi: 10.1007/978-88-470-1152-6_10.
- Peskin, C. S. (1982) ‘The Fluid Mechanics of Large Blood Vessels’, by T. J. Pedley’, *Medical Physics*. Cambridge University Press, 9(1), pp. 132–132. doi: 10.1118/1.595220.
- Peterson, L. . and Gerst, P. . (1956) ‘Significance of reflected waves within the arterial system’, *Fed Proc*, 15(496), p. 145.
- Poiseuille, J. L. M. (1846) ‘Recherches experimentales sur le mouvement des liquides dans les tubes de tres-petits diametres’, *Acad Sci de l’Institut de France*, 9, pp. 433–544.
- Pythoud, F., Stergiopoulos, N. and Meister, J. J. (1996) ‘Separation of arterial pressure waves into their forward and backward running components’, *Journal of Biomechanical Engineering*, 118(3), pp. 295–301. doi: 10.1115/1.2796010.
- Quail, M. A. *et al.* (2017) ‘Abnormal wave reflections and left ventricular hypertrophy late after coarctation of the aorta repair’, *Hypertension*, 69(3), pp. 501–509. doi: 10.1161/HYPERTENSIONAHA.116.08763.
- Rabben, S. I. *et al.* (2004) ‘An ultrasound-based method for determining pulse wave velocity in superficial arteries’, *Journal of Biomechanics*. Elsevier, 37(10), pp. 1615–1622. doi: 10.1016/j.jbiomech.2003.12.031.
- Raines, J. K., Jaffrin, M. Y. and Shapiro, A. H. (1974) ‘A computer simulation of arterial dynamics in the human leg’, *Journal of Biomechanics*, 7(1), pp. 77–91. doi: 10.1016/0021-9290(74)90072-4.
- Redheuil, A. *et al.* (2011) ‘Age-related changes in aortic arch geometry: Relationship with proximal aortic function and left ventricular mass and remodeling’, *Journal of the American College of Cardiology*, 58(12), pp. 1262–1270. doi: 10.1016/j.jacc.2011.06.012.
- Resnick, L. M. *et al.* (2000) ‘Pulse waveform analysis of arterial compliance: Relation to other techniques, age, and metabolic variables’, *American Journal of Hypertension*, 13(12), pp. 1243–1249. doi: 10.1016/S0895-7061(00)01219-X.
- Reuderink, P. J. *et al.* (1989) ‘Linear and nonlinear one-dimensional models of pulse wave transmission at high Womersley numbers’, *Journal of Biomechanics*, 22(8–9), pp. 819–827. doi: 10.1016/0021-9290(89)90065-1.
- Reuderink, P., Sipkema, P. and Westerhof, N. (1988) ‘Influence of geometric taper on the derivation of the true propagation coefficient using a three point method’, *Journal of Biomechanics*. Elsevier, 21(2), pp. 141–153. doi: 10.1016/0021-9290(88)90007-3.
- Reymond, P. *et al.* (2009) ‘Validation of a one-dimensional model of the systemic arterial tree’, *American Journal of Physiology - Heart and Circulatory Physiology*. American Physiological

- Society, 297(1), pp. H208–H222. doi: 10.1152/ajpheart.00037.2009.
- Reymond, P. *et al.* (2011) ‘Validation of a patient-specific one-dimensional model of the systemic arterial tree’, *American Journal of Physiology - Heart and Circulatory Physiology*, 301(3), pp. 208–222. doi: 10.1152/ajpheart.00821.2010.
- Reynolds, O. (1883) ‘An experimental investigation of the circumstances which determine whether the motion of water in parallel channels shall be direct or sinuous and of the Society, The Royal Transactions, Philosophical Society, Royalaw of resistance in parallel channels’, *Society, The Royal Transactions, Philosophical Society, Royal*, 174(1883), pp. 935–982.
- Riemann, B. (1876) ‘Gesammelte Mathematische Werke und Wissenschaftlicher Nachlass’, pp. 23–590. doi: 10.1007/978-3-663-10149-9_1.
- Saito, M. *et al.* (2011) ‘One-dimensional model for propagation of a pressure wave in a model of the human arterial network: Comparison of theoretical and experimental results’, *Journal of Biomechanical Engineering*, 133(12), p. 121005. doi: 10.1115/1.4005472.
- Schaaf, B. W. and Abbrecht, P. H. (1972) ‘Digital computer simulation of human systemic arterial pulse wave transmission: A nonlinear model’, *Journal of Biomechanics*, 5(4), pp. 345–364. doi: 10.1016/0021-9290(72)90064-4.
- Segers, P. *et al.* (2005) ‘Conductance catheter-based assessment of arterial input impedance, arterial function, and ventricular-vascular interaction in mice’, *American Journal of Physiology - Heart and Circulatory Physiology*, 288(3), pp. H1157–H1164. doi: 10.1152/ajpheart.00414.2004.
- Segers, P., Rietzschel, Ernst R, *et al.* (2007) ‘Assessment of pressure wave reflection: Getting the timing right!’, *Physiological Measurement*. IOP Publishing, 28(9), pp. 1045–1056. doi: 10.1088/0967-3334/28/9/006.
- Segers, P., Rietzschel, Ernst R., *et al.* (2007) ‘Noninvasive (input) impedance, pulse wave velocity, and wave reflection in healthy middle-aged men and women’, *Hypertension*, 49(6), pp. 1248–1255. doi: 10.1161/HYPERTENSIONAHA.106.085480.
- Segers, P. *et al.* (2017) ‘Towards a consensus on the understanding and analysis of the pulse waveform: Results from the 2016 Workshop on Arterial Hemodynamics: Past, present and future’, *Artery Research*. Elsevier, 18, pp. 75–80. doi: 10.1016/j.artres.2017.03.004.
- Segers, P. and Verdonck, P. (2000) ‘Role of tapering in aortic wave reflection: hydraulic and mathematical model study’, *Journal of Biomechanics*, 33(3), pp. 299–306.
- Sherwin, S. J. *et al.* (2003) ‘One-dimensional modelling of a vascular network in space-time variables’, *Journal of Engineering Mathematics*, 47(3–4), pp. 217–250. doi: 10.1023/B:ENGI.0000007979.32871.e2.

-
- Shi, Y., Lawford, P. and Hose, R. (2011) 'Review of Zero-D and 1-D Models of Blood Flow in the Cardiovascular System', *BioMedical Engineering Online*, 10, p. 33. doi: 10.1186/1475-925X-10-33.
- Smith, N. P., Pullan, A. J. and Hunter, P. J. (2002) 'An Anatomically Based Model of Transient Coronary Blood Flow in the Heart', *SIAM Journal on Applied Mathematics*, 62(3), pp. 990–1018. doi: 10.1137/S0036139999355199.
- Steele, B. N. *et al.* (2003) 'In vivo validation of a one-dimensional finite-element method for predicting blood flow in cardiovascular bypass grafts', *IEEE Transactions on Biomedical Engineering*, 50(6), pp. 649–656. doi: 10.1109/TBME.2003.812201.
- Stergiopoulos, N. *et al.* (1996) 'On the wave transmission and reflection properties of stenoses', *Journal of Biomechanics*, 29(1), pp. 31–38. doi: 10.1016/0021-9290(95)00023-2.
- Stergiopoulos, N., Tardy, Y. and Meister, J. J. (1993) 'Nonlinear separation of forward and backward running waves in elastic conduits', *Journal of Biomechanics*. Elsevier, 26(2), pp. 201–209. doi: 10.1016/0021-9290(93)90049-K.
- Stergiopoulos, N., Young, D. F. and Rogge, T. R. (1992) 'Computer simulation of arterial flow with applications to arterial and aortic stenoses', *Journal of Biomechanics*. Elsevier, 25(12), pp. 1477–1488. doi: 10.1016/0021-9290(92)90060-E.
- Stettler, J. C., Niederer, P. and Anliker, M. (1981) 'Theoretical analysis of arterial hemodynamics including the influence of bifurcations - Part I: Mathematical model and prediction of normal pulse patterns', *Annals of Biomedical Engineering*. Kluwer Academic Publishers, 9(2), pp. 145–164. doi: 10.1007/BF02363533.
- STREETER, V. L., KEITZER, W. F. and BOHR, D. F. (1963) 'Pulsatile Pressure and Flow Through Distensible Vessels.', *Circulation research*, 13, pp. 3–20. doi: 10.1161/01.RES.13.1.3.
- Su, J. *et al.* (2017) 'Wave intensity analysis provides novel insights into pulmonary arterial hypertension and chronic thromboembolic pulmonary hypertension', *Journal of the American Heart Association*. John Wiley and Sons Inc., 6(11), p. e006679.
- Sugawara, J. *et al.* (2008) 'Age-Associated Elongation of the Ascending Aorta in Adults', *JACC: Cardiovascular Imaging*. Elsevier, 1(6), pp. 739–748. doi: 10.1016/j.jcmg.2008.06.010.
- Sun, Y. H. *et al.* (2004) 'Effects of left ventricular contractility and coronary vascular resistance on coronary dynamics', *American Journal of Physiology - Heart and Circulatory Physiology*. American Physiological Society, 286(4), pp. H1590–H1595.
- Swillens, A. *et al.* (2008) 'Effect of an abdominal aortic aneurysm on wave reflection in the aorta', *IEEE Transactions on Biomedical Engineering*, 55(5), pp. 1602–1611. doi:

10.1109/TBME.2007.913994.

- Taylor, M. G. (1959) 'An experimental determination of the propagation of fluid oscillations in a tube with a visco-elastic wall; Together with an analysis of the characteristics required in an electrical analogue', *Physics in Medicine and Biology*, 4(1), pp. 63–82. doi: 10.1088/0031-9155/4/1/308.
- Van de Vosse, F. N. and Stergiopoulos, N. (2011) 'Pulse Wave Propagation in the Arterial Tree', *Annual Review of Fluid Mechanics*, 43(1), pp. 467–499. doi: 10.1146/annurev-fluid-122109-160730.
- Wang, J. *et al.* (2006) 'Systemic venous circulation. Waves propagating on a windkessel: Relation of arterial and venous windkessels to systemic vascular resistance', *American Journal of Physiology - Heart and Circulatory Physiology*, 290(1), pp. H154-62.
- Wang, J. J. and Parker, K. H. (2004) 'Wave propagation in a model of the arterial circulation', *Journal of Biomechanics*, 37(4), pp. 457–470. doi: 10.1016/j.jbiomech.2003.09.007.
- Wang, Z., Golob, M. J. and Chesler, N. C. (2016) 'Viscoelastic Properties of Cardiovascular Tissues', in *Viscoelastic and Viscoplastic Materials*. InTech. doi: 10.5772/64169.
- Weber, E. H. and Weber, W. (1825) *Wellenlehre auf Experimente gegründet, oder über die Wellen tropfbarer Flüssigkeiten mit Anwendung auf die Schall- und Lichtwellen*. Leipzig.
- Weizsacker, H. W. and Pinto, J. G. (1988) 'Isotropy and anisotropy of the arterial wall', *Journal of Biomechanics*, 21(6), pp. 477–487. doi: 10.1016/0021-9290(88)90240-0.
- Wemple, R. R. and Mockros, L. F. (1972) 'Pressure and flow in the systemic arterial system', *Journal of Biomechanics*, 5(6), pp. 629–641. doi: 10.1016/0021-9290(72)90035-8.
- Westerhof, B. E. *et al.* (2008) 'Location of a reflection site is elusive: Consequences for the calculation of aortic pulse wave velocity', *Hypertension*, 52(3), pp. 478–483. doi: 10.1161/HYPERTENSIONAHA.108.116525.
- Westerhof, N. *et al.* (1969) 'Analog studies of the human systemic arterial tree', *Journal of Biomechanics*, 2(2), pp. 121–43. doi: 10.1016/0021-9290(69)90024-4.
- Westerhof, N. *et al.* (1972) 'Forward and backward waves in the arterial system', *Cardiovascular Research*, 6(6), pp. 648–656. doi: 10.1093/cvr/6.6.648.
- Westerhof, N., Elzinga, G. and Sipkema, P. (1971) 'An artificial arterial system for pumping hearts.', *Journal of applied physiology*, 31(5), pp. 776–781. doi: 10.1152/jappl.1971.31.5.776.
- Westerhof, N., Lankhaar, J. W. and Westerhof, B. E. (2009) 'The arterial windkessel', *Medical and Biological Engineering and Computing*. Springer-Verlag, 47(2), pp. 131–141. doi: 10.1007/s11517-008-0359-2.
- Willemet, M. and Alastruey, J. (2014) 'Arterial Pressure and Flow Wave Analysis Using Time-

-
- Domain 1-D Hemodynamics’, *Annals of Biomedical Engineering*. Springer, 43(1), pp. 190–206. doi: 10.1007/s10439-014-1087-4.
- Willemet, M., Lacroix, V. and Marchandise, E. (2011) ‘Inlet boundary conditions for blood flow simulations in truncated arterial networks’, *Journal of Biomechanics*. Elsevier, 44(5), pp. 897–903. doi: 10.1016/j.jbiomech.2010.11.036.
- Willemet, M., Lacroix, V. and Marchandise, E. (2013) ‘Validation of a 1D patient-specific model of the arterial hemodynamics in bypassed lower-limbs: Simulations against in vivo measurements’, *Medical Engineering and Physics*, 35(11), pp. 1573–1583.
- Willemet, M., Vennin, S. and Alastruey, J. (2016) ‘Computational assessment of hemodynamics-based diagnostic tools using a database of virtual subjects: Application to three case studies’, *Journal of Biomechanics*, 49(16), pp. 3908–3914. doi: 10.1016/j.jbiomech.2016.11.001.
- Xiao, N., Alastruey, J. and Figueroa, C. A. (2014) ‘A systematic comparison between 1-D and 3-D hemodynamics in compliant arterial models’, *International Journal for Numerical Methods in Biomedical Engineering*. NIH Public Access, 30(2), pp. 204–231. doi: 10.1002/cnm.2598.
- Zambanini, A. *et al.* (2005) ‘Wave-energy patterns in carotid, brachial, and radial arteries: A noninvasive approach using wave-intensity analysis’, *American Journal of Physiology - Heart and Circulatory Physiology*, 289(1), pp. 270–276. doi: 10.1152/ajpheart.00636.2003.
- Zamir, M. (2000) *The Physics of Pulsatile Flow*. New York: Springer-Verlag.